Doctoral Dissertation (Censored)

博士論文 (要約)

Modulation of physical properties
of 4*d*-5*d* transition metal oxide thin films
by anion doping
(アニオンドープによる
4*d*-5*d* 遷移金属酸化物薄膜の物性変調)

A Dissertation Submitted for the Degree of Doctor of Science

December 2020

令和 2 年 12 月博士(理学)申請

Department of Chemistry, Graduate School of Science,

The University of Tokyo

東京大学大学院理学系研究科化学専攻

Takahiro Maruyama

丸山　敬裕

Modulation of physical properties
of $4d$-$5d$ transition metal oxide thin films
by anion doping

by

Takahiro Maruyama

Department of Chemistry

Graduate School of Science

The University of Tokyo

December 2020

Abstract

1. Introduction

4d-5d based transition metal oxides (TMOs) show distinctive electronic properties due to large overlap of electron orbitals and large spin-orbit interaction (SOI). Some 4d-5d based TMOs, such as $SrMoO_3$ and ReO_3, are good conductors, of which resistivity is comparable to those of conventional metals, due to the spatially spread d orbitals, and Sr_2RuO_4 is known to be an unconventional spin-triplet superconductor. Iridium oxides exhibit unique physical properties, including Weyl semimetal phases, owing to the large SOI of Ir ions.

Recently, doping of anion, such as H^-, N^{3-} and F^-, into 4d-5d TMOs has attracted much attention as a powerful method to modulate their physical properties through carrier doping, control of local anion arrangement, and so on. A typical example is $RbLaNb_2O_6F$, which possesses high electronic conductivity with ion exchange ability. $SrNbO_2N$ shows large positive magnetoresistance, which originates from the random distribution of oxygen and nitrogen in the crystal.

In this thesis study, I have focused on two 4d-5d TMOs, $EuNbO_3$ and Sr_2IrO_4, and attempted to modify their electronic properties by nitrogen and fluorine doping, respectively. Nb in $EuNbO_3$ has electrons in 4d orbitals, which interact with large spins at Eu, resulting in rich physical properties. For modulation of the interaction, I introduced anion randomness by nitrogen doping. Ir in Sr_2IrO_4 is a typical element with large SOI. I examined how the electronic properties are affected by anion randomness and change in dimensionality associated with fluorine doping. For these purposes, I synthesized

Abstract

nitrogen doped $EuNbO_3$ and fluorine doped Sr_2IrO_4 thin films and discussed the modulation of physical properties.

2. Magnetotransport properties of perovskite $EuNbO_3$ thin films

Before studying nitrogen-doped $EuNbO_3$, I investigated the magnetic and transport properties of perovskite $EuNbO_3$ single-crystalline thin films deposited by pulsed laser deposition. The obtained $EuNbO_3$ thin films showed metallic transport properties and ferromagnetism with a Curie temperature (T_C) of ~6 K. The carrier concentration and mobility of the $EuNbO_3$ thin films were nearly independent of temperature, suggesting that the excess oxygen in the films behaves as a scattering center. The sign of magnetoresistance changed around T_C, possibly due to competition between the weak anti-localization effect and magnetic coupling between Eu^{2+} $4f$ localized spins and Nb^{4+} $4d$ itinerant electrons.

3. Nitrogen content dependence of negative magnetoresistance in $EuNbO_{3-x}N_x$ thin films

Perovskite-type europium niobium oxynitride $EuNbO_2N$ is known to exhibit colossal negative magnetoresistance (MR > −99%) at low temperature. In order to investigate the role of nitrogen in the negative MR, I fabricated $EuNbO_{3-x}N_x$ single-crystalline thin films with different nitrogen contents (N/Eu = 0.6, 0.7, 1.0) and measured their magnetotransport properties. All the oxynitride thin films showed saturation magnetization of ~3.0 μ_B/f.u., indicating that nearly half of the Eu ions exist in trivalent oxidation states independent of the nitrogen content. The transport properties of the $EuNbO_{3-x}N_x$ thin films gradually changed from metallic behavior to semiconducting behavior as the nitrogen content x increased. The semiconducting conduction was described by three-dimensional variable-range hopping, suggesting that carrier

Abstract

localization occurs due to the random distribution of nitrogen in the anion sites. With increasing x, the negative MR ratio at 2 K increased from 20 % to 98 %, accompanied by an increase of Nb^{5+} amount in the films. Based on results of magneto-transport measurements, I proposed that the exchange interaction between Eu^{2+} and $Nb\ 4d^1$ localized spins and $Nb\ 4d^1$ spins in the random potential was a key to the colossal negative MR of ENON.

4. Influence of fluorination on electronic states and electron transport properties of Sr_2IrO_4 thin films

I fabricated layered-perovskite $Sr_2IrO_{4−x}F_{2x}$ thin films by combining pulsed-laser deposition with topotactic fluorination and investigated their structures, electronic states, and electron transport properties. In the fluorination process, the insertion of fluorine into SrO rocksalt layers and the partial removal of oxygen occurred simultaneously while keeping Ir^{4+}. The fluorine amount was evaluated to be $2x \approx 3$, which was much larger than the bulk value. Optical and photoemission measurements revealed that the effective total angular momentum $J_{\mathrm{eff}} = 3/2$ is stabilized upon fluorination owing to the large electronegativity of fluorine. The conduction mechanism was observed in both Sr_2IrO_4 and $Sr_2IrO_{4-x}F_{2x}$ thin films, where $\rho(T)$s of Sr_2IrO_4 and $Sr_2IrO_{4-x}F_{2x}$ were proportional to $T^{-1/4}$ and $T^{-1/2}$, respectively. The change of the temperature dependence upon fluorine doping indicates that the conduction mechanism was modulated from the Mott variable-range hopping mechanism to the Efros–Shklovskii variable-range hopping mechanism. The change of conduction mechanism could result from the increase of Coulomb interaction among electrons, which may be induced by confinement of electrons in the $Ir(O, F)_6$ layer and by suppression of electron screening effect

Abstract

due to the random potential in Ir(O, F)$_6$. Our research provides valuable insight into how electronic states can be modified by anion doping to explore unprecedented physical properties in RP-type iridates.

5. Conclusion

I successfully modulated the physical properties of $4d$-$5d$ TMO thin films by anion doping and provided valuable insights into the intrinsic role of the anion. In the study of EuNbO$_{3-x}$N$_x$, it was revealed that randomly distributed nitrogen ions locally modulate the exchange interaction between Eu^{2+} localized spins and Nb $4d^1$ spin. In the study of Sr$_2$IrO$_{4-x}$F$_{2x}$, it was proposed that fluorine doping could increase the Coulomb interaction among electrons by strengthening two-dimensionality and by introducing random distribution of oxygen and nitrogen. Deep understanding of the role of the anions would lead to the finding of unprecedented physical properties of in $4d$-$5d$ transition metal-based mixed anion compounds.

Acknowledgment

First and foremost, I would like to thank my supervisor, Prof. Tetsuya Hasegawa, for giving me the precious opportunity to research in this laboratory. He has created an excellent environment in which I can conduct cutting-edge research activities without any worries. Thanks to a variety of equipment, I was able to measure samples of interest immediately and satisfy my intellectual curiosity to my heart's content. I very much appreciate you for all the ways you have made my daily research life more comfortable. Since my professor values the phrase "Are you happy?" I could proceed with my research in a relaxed manner without feeling extreme pressure and anxiety, making me happy. He always gave me insightful and accurate advice based on the insights he had gained over the years during research discussions, presentation practice for conferences, and paper corrections. Besides, I cannot thank him enough for his calmness in handling the serious trouble in one day. I am genuinely convinced that this thesis would never have been completed without his tremendous support.

As a member of the Chikamatsu Group, I am indebted to Assistant Prof. Akira Chikamatsu for providing me with this challenging and intriguing projects. I had the pleasure of discussing research and chatting about our daily chores with him. He corrected many texts, such as research papers and applications for me. His comments were always precise, concise, and straightforward. My writing skills as a researcher have been nurtured through the process of steadily responding to his suggestions. I truly appreciated that. Whenever I was stuck in my work, he was always warm and kind enough to encourage me. Also, I learned a lot from our honest discussions about all-night measurements at

Contents

Chapter 1 General introduction

1.1 Physical properties of 3*d* transition metal oxides

Transition metal oxides (TMOs) have occupied an important position in materials science because they have a variety of physical properties such as complex magnetism, metal-insulator transition, magnetoresistance, and superconductivity. The *d* electrons in TMOs play a crucial role in determining the electronic ground state. Usually, the *d* electrons tend to localize around atomic nuclei compared with *s* or *p* electrons. Since the *d* electrons are confined in the narrow space, they are significantly influenced by strong Coulomb interaction among themselves. In this situation, multiple degrees of freedom, charge, spins, orbital, and lattice are closely interacted, of which situation is illustrated in Figure 1.1.1. Under this circumstance, a slight stimulus can cause dramatic changes in the electronic ground state and lead to a wide variety of physical properties. Since 3*d* TMOs have been more intensively studied than 4*d*-5*d* TMOs, I firstly introduce some representative examples of physical properties in 3*d* TMOs.
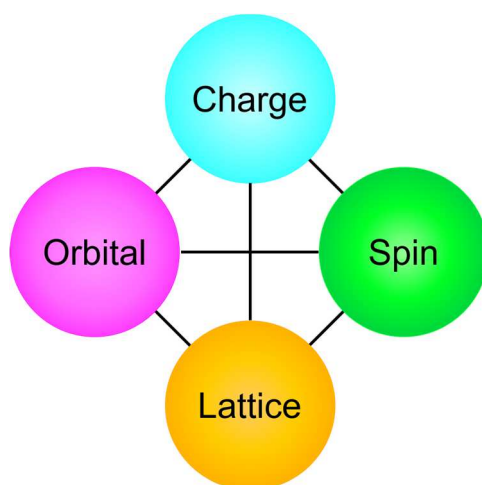
Figure 1.1.1 Multiple degree of freedom in TMOs.

1.1 Physical properties of 3d transition metal oxides

Mott insulating state and metal-insulator-transition (MIT) in $3d$ TMOs have been intensively studied for decades [1]. Figure 1.1.2(a) shows a schematic illustration of the Mott insulating state. When d orbitals of an oxide compound are partially filled with some electrons, the oxide is supposed to be a metal according to the band theory. However, it becomes an insulator when the electrons cannot hop to adjacent sites due to the Coulomb interaction between electrons. There are three key parameters to understand the electronic ground state: U, W, and n. U is the Coulomb repulsion between two electrons at the same site, W is the bandwidth, and n is the electron number. The competition among those parameters determines the electronic ground state whose phase diagram is shown in Figure 1.1.2(b). The vertical axis of the diagram is electron correlation evaluated by the ratio of U/W, and the horizontal axis is the deviation of electron number n from a particular integer. As electric correlation becomes large and the electron number approaches one specific integer, the system is likely to be Mott insulating state. When the system locates at the boundary region between metal and Mott insulating area, it is basically metal, but carriers are easily localized by extrinsic effects such as randomness in a crystal and electron-lattice coupling.

MIT is induced by two different ways: Chang of electric correlation U/W and change of electron number n. The former is called Bandwidth control MIT (BC-MIT), and the latter is called Filling control MIT (FC-MIT), which are shown as the arrows in Figure 1.1.2(b). BC-MIT can be seen in perovskite oxides ABO_3 with transition metal at B-site. For example, $LaNiO_3$ transforms from a metal to an insulator by substituting smaller rare earth cations [2–4]. Substitution of smaller cations for A-site causes bending of B–O–B bond angles from 180°, which induces suppression of d-p orbital overlap and reduces bandwidth W, resulting in the increase of U/W. On the other hand, FC-MIT can

2

be observed in the carrier doped Mott insulator. For example, a Mott insulator $LaVO_3$ becomes a metal by hole doping via substitution of La^{3+} by Sr^{2+} [5] or Ca^{2+} [6].
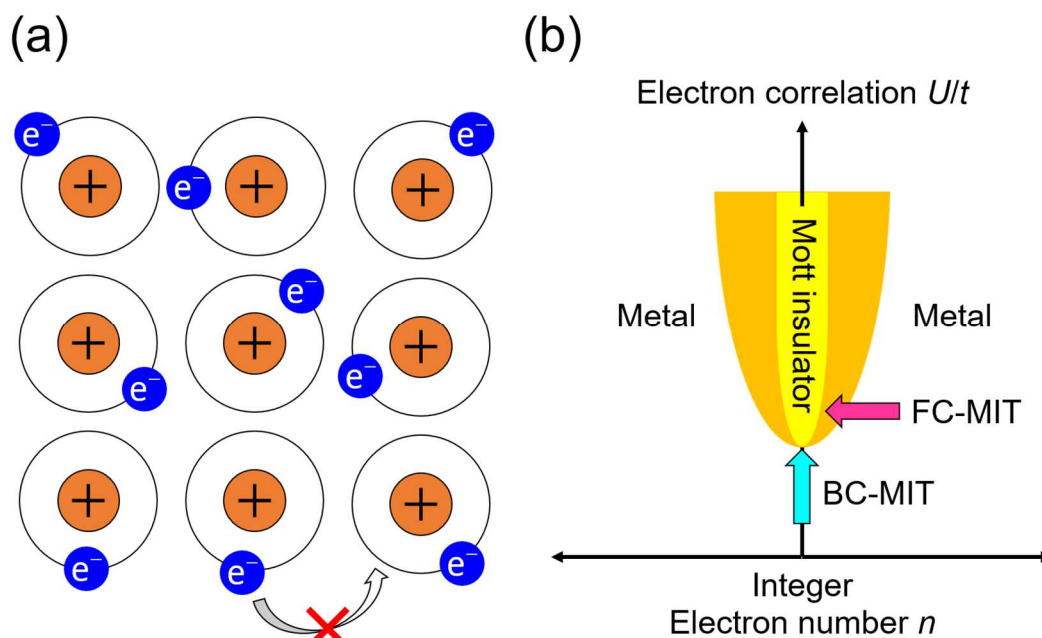
Figure 1.1.2 (a) A schematic illustration of a Mott insulator. (b) Phase diagram around Mott insulating state. Two allows denote two mechanisms of MIT.

Magnetism in $3d$ TMOs has also been vigorously studied for many years. A famous fundamental rule for TMOs is the Kanamori-Goodenough rule, which mainly focuses on superexchange interaction between transition metal ions through oxygen ions. Two examples are shown in Figure 1.1.3. When two transition metal ions and an oxygen ion are aligned in line as shown in Figure 1.1.3(a), spins at the two metal ions are aligned antiferromagnetically because a hopping process of an electron from the oxygen ion to transition metal ions are allowed. On the other hand, when the M-O-M angle is 90°; as shown in Figure 1.1.3(b), the spins of the two metal ions are aligned ferromagnetically. In real materials, structural distortion makes the M-O-M angle different from either 90° or 180°, which causes competition between the two mechanisms.
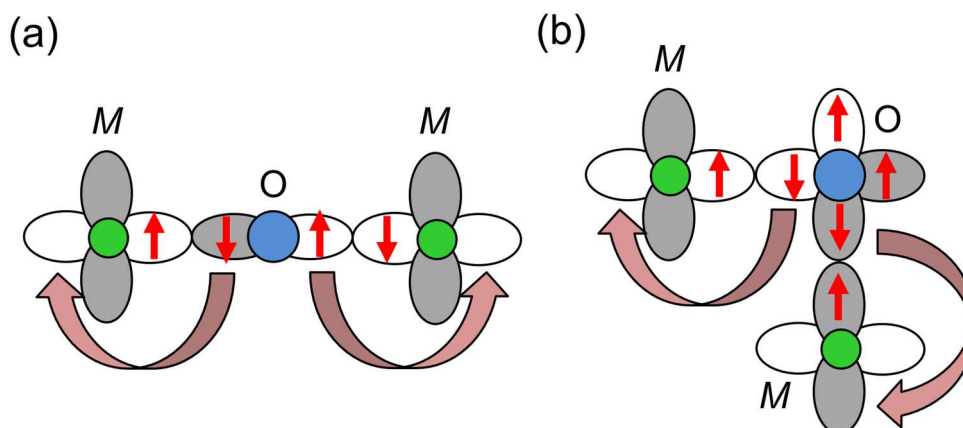
Figure 1.1.3 Schematic illustration of superexchange interaction.
(a) antiferromagnetic interaction in M-O-M with a bond angle of 180°.
(b) ferromagnetic interaction in M-O-M with a bond angle of 90°.

More complex magnetism has also been observed in $3d$ TMOs. An example is LaCoO$_3$, which basically exhibits paramagnetism. However, the magnetic susceptibility increases as the temperature increases and shows a maximum around 100 K, as shown in Figure 1.1.4(a) [7]. This behavior is far different from normal paramagnetic behavior of other RCoO$_3$ (R = Sm, Eu), where the magnetic susceptibility decreases as the temperature increases (Figure 1.1.4(b),(c)). Moreover, there is an anomaly of magnetic susceptibility around 500 K accompanied with drastic reduction of electrical resistivity [7–11]. Such complex behavior originates from three different spin states of Co^{3+} with d^6 electronic configuration, as summarized in Figure 1.1.4(d): the low spin state (LS) with $S = 0$, the intermediate state (IS) with $S = 1$, and the high spin state (HS) with $S = 2$. The energies of these three states depend on the close interplay among the Hund's coupling J_{Hund}, crystallographic splitting Δ, electron-transfer integral t, and electron repulsion U. As a result, the energy levels of the three spin configurations are sensitive to many factors such as temperature, physical pressure, and a magnetic field, resulting in the unusual magnetic behaviors.
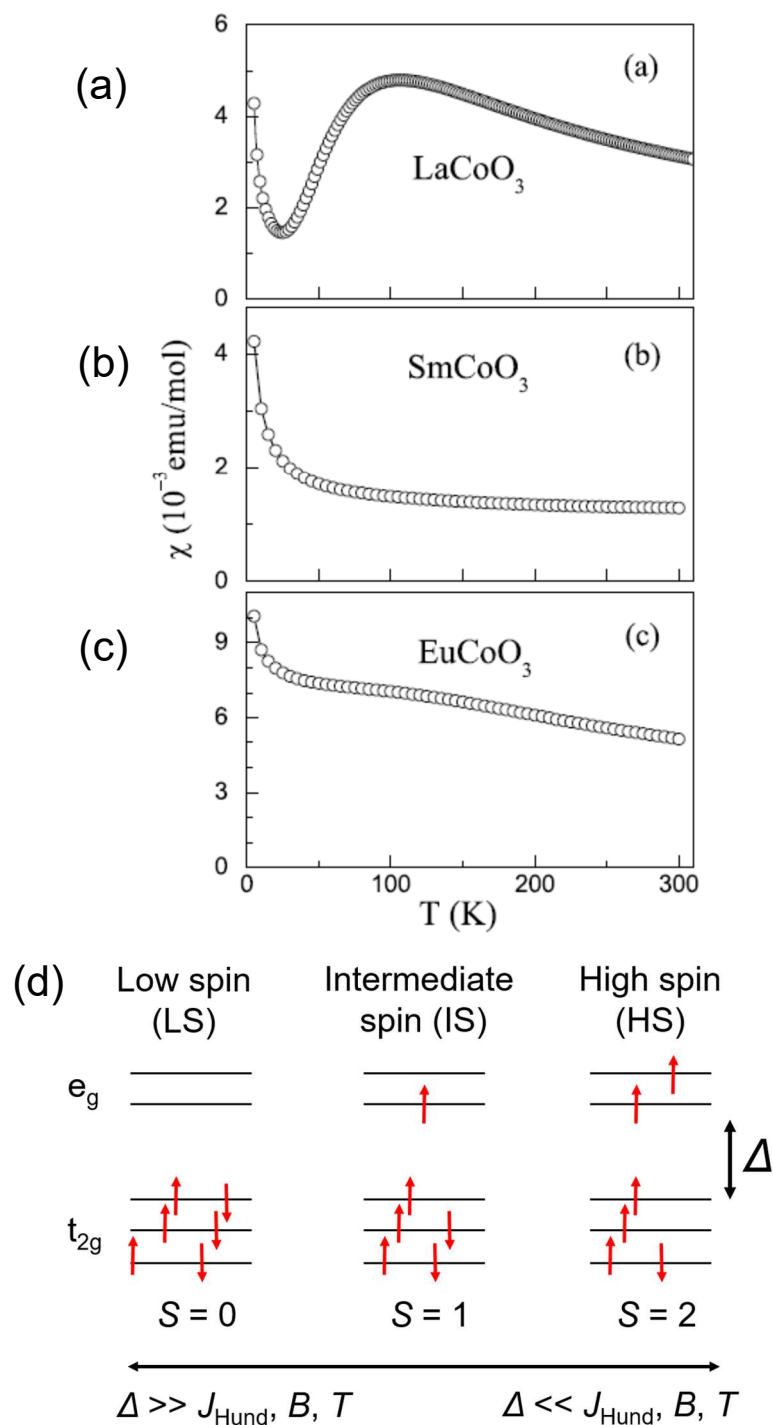
Figure 1.1.4 (a)-(c) Temperature dependences of the susceptibility of $R\text{CoO}_3$ compounds (R = La, Sm, Eu) (d) three different spin states of Co^{3+} with d^6 electronic configuration. the low spin state (LS) with $S = 0$, the intermediate state (IS) with $S = 1$, and the high spin state (HS) with $S = 2$. (a), (b), and (c) are reprinted with permission from [7]. Copyright 2019 by Elsevier.

The interaction between electric conduction and magnetism can be seen in a magnetoresistance (MR) effect, which represents modulation of electric conductivity by an external magnetic field. A representative MR compound is hole-doped $LaMnO_3$, which shows a considerably large MR effect [12–16]. The crystal structure of $LaMnO_3$ is shown in Figure 1.1.5(a) (This and the following figures of crystal structures are drawn with VESTA [17]). The undoped material $LaMnO_3$ is insulating and antiferromagnetic. Once a hole is doped to $LaMnO_3$, it becomes metallic and ferromagnetic at low temperatures, as shown in Figures 1.1.5(b). Besides, electric resistivity is significantly reduced around the Curie temperature by applying a magnetic field, which is called colossal negative MR effect (Figures 1.1.5(c)).
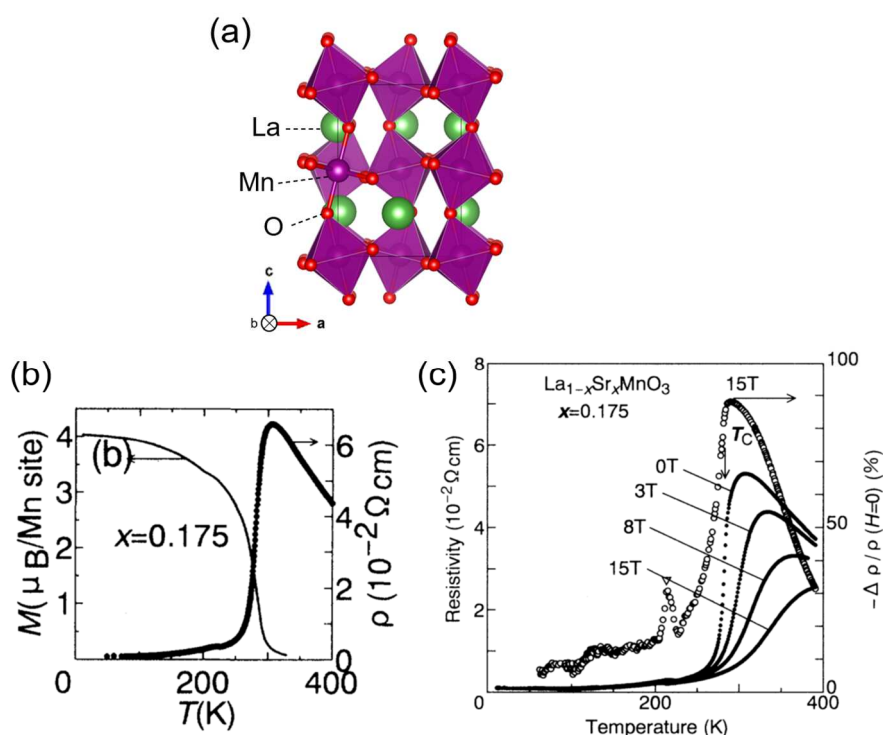
Figure 1.1.5 (a) Crystal structure of $LaMnO_3$. (b) Correlation between the temperature dependence of resistivity and magnetic moment for $La_{1-x}Sr_xMnO_3$ ($x = 0.175$). (c) Temperature dependence of resistivity $La_{1-x}Sr_xMnO_3$ ($x = 0.175$) for under various magnetic fields; Open circles represent the magnitude of negative magnetoresistance $-[\rho(H)-\rho(0)]/\rho(0)$ with a magnetic field of 15 T. (b) and (c) are reprinted with the permission from [16]. Copyrights 1995 by the American Physical Society.

Here, I explain the colossal MR effect using a schematic illustration for the electronic configuration of Mn^{3+} (Figure 1.1.6). Five $3d$ orbitals are split by crystal field and Jahn Teller distortion, resulting in the configuration with one electron in one e_g ($3d_{z2}$) orbital and three electrons in three t_{2g} orbitals, as drawn in Figure 1.1.6(a). Figure 1.1.6(b) compares the undoped and doped states. In undoped $LaMnO_3$, the one free electron in the $3d_{z2}$ orbital cannot hop from one site to another due to strong on-site Coulomb interaction, which is referred to as Mott insulating state. The antiferromagnetism originates from the superexchange interaction between Mn^{3+} ions via O^{2-} ions. When a hole is doped to $LaMnO_3$, the $3d_{z2}$ orbital at Mn^{4+} becomes empty. Another important feature of Mn^{3+} is strong Hund's coupling between the conduction (e_g) spin and localized (t_{2g}) spins. If the spins of Mn^{3+} and Mn^{4+} are aligned in the same direction, the electron in $3d_{z2}$ orbital at Mn^{3+} becomes mobile by hopping, resulting in a metallic state. Thus, the doping of holes into $LaMnO_3$ causes a transition from antiferromagnetic insulating state to ferromagnetic metallic states. This mechanism is called double exchange interaction mechanism.

The mechanism can qualitatively describe the colossal negative MR at Curie temperature, as shown in Figure 1.1.6(c). The electron hopping probability from one site to next is proportional to cos (θ/2), where θ is the relative angle of two spins in t_{2g} orbitals at adjacent two sites. At Curie temperature without a magnetic field, spins at t_{2g} orbitals orientate randomly, resulting in low hopping probability of electrons. Once a magnetic field is applied, the spins begin to be aligned in parallel, resulting in high hopping probability of electrons. The difference in hopping probability leads to the colossal negative MR effects.
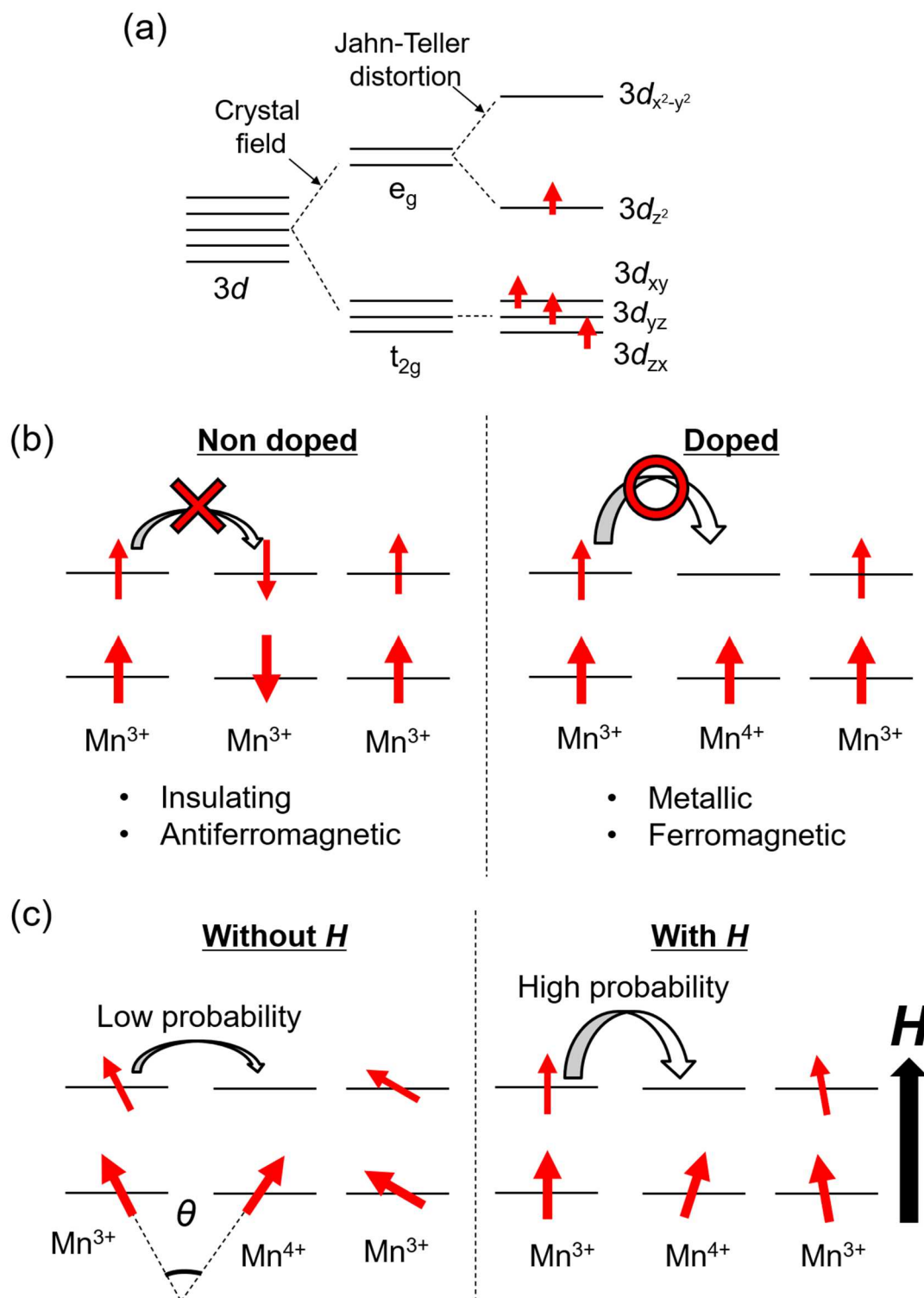
Figure 1.1.6 (a) Electric configuration of Mn^{3+}.

(b) Explanation of double exchange coupling in hole-doped $LaMnO_3$.

(c) Mechanism of colossal negative magnetoresistance.

High-temperature superconductivity is the most famous physical properties of $3d$ TMOs. The study began from Ba doped La_2CuO_4 with a critical temperature (T_c) of 30 K [18,19], whose crystal structure is shown in Figure 1.1.6(a). Since this discovery, superconductivity has been discovered in various copper oxides, such as $La_{2-x}Sr_xCuO_4$ [20], $Nd_{2-x}Ce_xCuO_4$ [21], and $YBa_2Cu_3O_{6+\delta}$ [22]. As materials exploration proceeds, the maximum T_c elevated and reached 130 K in $HgBa_2Ca_2Cu_3O_x$ at ambient pressure [23]. One of the significant features of copper oxide superconductors is that the superconductivity emerges when a moderate amount of carriers are doped into a pristine oxide. Figure 1.1.6(b) shows the typical electronic phase diagram of superconducting copper oxides. The electronic ground state drastically changes from antiferromagnetic Mott insulating state to metallic states and superconducting state is induced by doping an appropriate amount of electron or hole.

In undoped copper oxides, the Cu ion is in the divalent state with $3d^9$ electric configuration, as illustrated in Figure 1.1.6(c). Five $3d$ orbitals split into three groups due to the crystal field effect and the Jahn Teller effect, resulting in the situation that only one electron occupies the $3d_{x2-y2}$ orbital. The $3d_{x2-y2}$ orbitals are hybridized with O $2p$ orbitals, forming CuO_2 planes, as shown in Figure 1.1.6(d). The pristine oxide with half occupied $3d_{x2-y2}$ is a Mott insulator due to the on-site Coulomb repulsion. As mentioned above, the high T_c superconductivity is attributable to the close interplay between itinerant electrons and spin. However, a unified perspective for the mechanism of high T_c superconductivity has not been established yet, and many kinds of research are still ongoing even now.
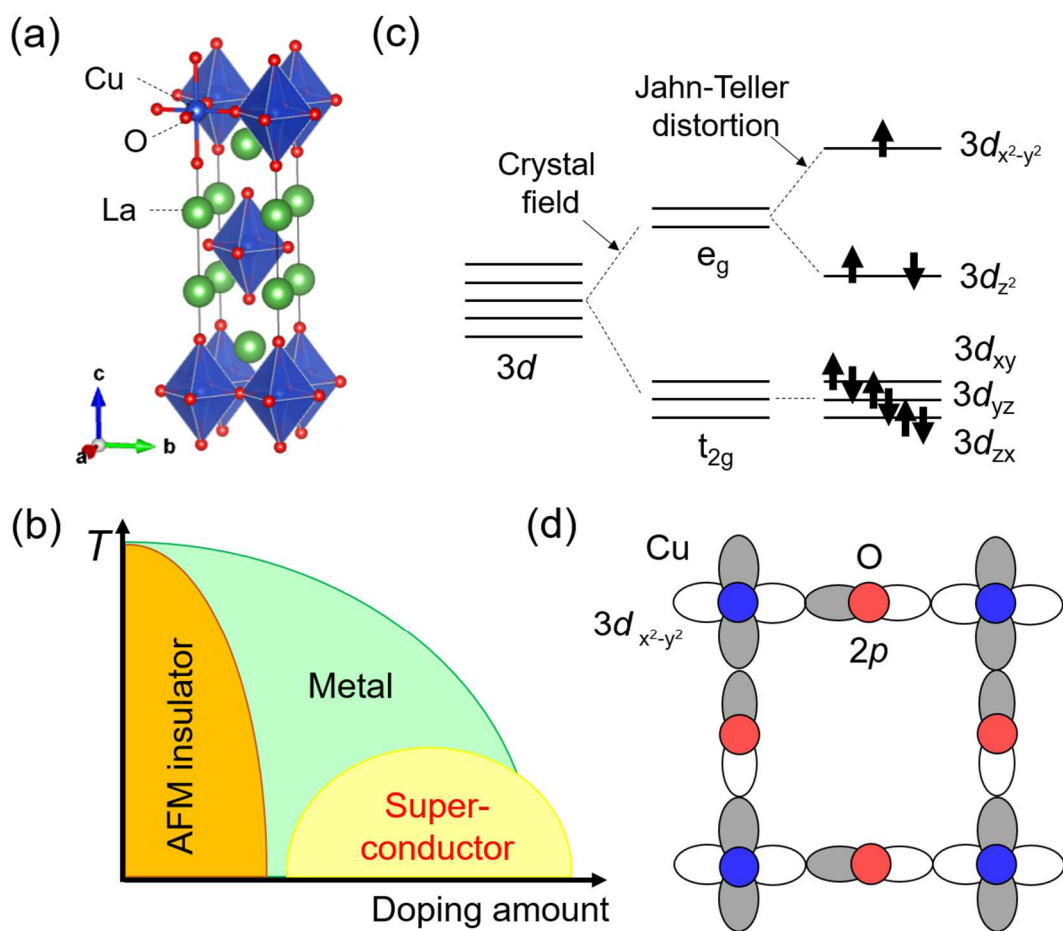
Figure 1.1.7 (a) Crystal structure of La_2CuO_4. (b) Typical phase diagram of cupper oxide superconductor (c) Electric configuration of Cu^{2+} (d) Schematic illustration of CuO_2 planes

1.2 Physical properties of 4*d*-5*d* transition metal oxides

The physical properties of 4*d*-5*d* TMOs are incredibly unique compared to those of 3*d* TMOs. The reason is attributable to its spatially distributed *d* orbitals. Figure 1.2.1 plots radical distribution functions of 3*d*, 4*d,* and 5*d* orbitals [24], which manifests how 4*d* and 5*d* orbitals spatially spread more than 3*d* one. This spread distribution of 4*d* and 5*d* orbitals leads to large overlaps between each other and large spin-orbit interaction (SOI). Owing to these features, 4*d*-5*d* TMOs show distinctive properties different from those of 3*d* TMOs. In this section, I introduce attractive physical properties of 4*d*-5*d* TMOs.
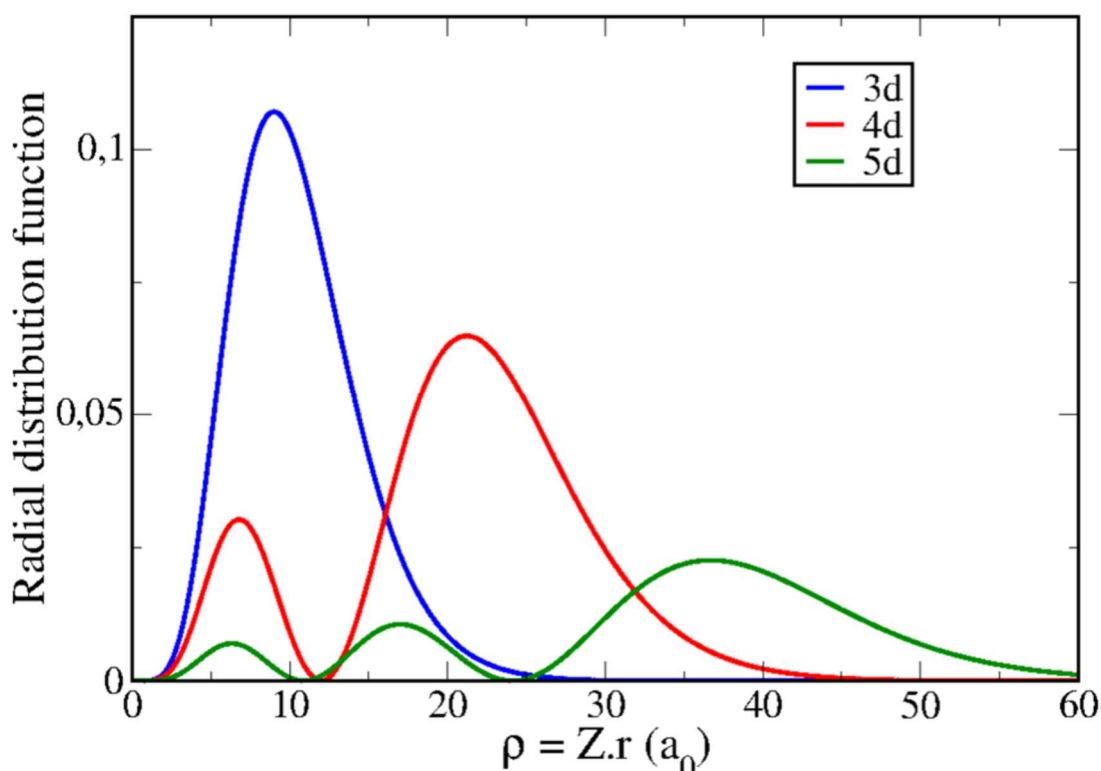
Figure 1.2.1 The radical distribution function of 3*d*, 4*d* and 5*d* orbitals. Reprinted with permission from [24]. Copyright 2017 by IOP Publishing. (Licensed under CC BY 4.0)

1.2 Physical properties of 4d-5d transition metal oxides

One prominent feature is high conductivity. Table 2.1 gathers resistivity values of some 4*d*-5*d* TMOs Some oxides like $SrMoO_3$ and ReO_3 are good conductors, of which conductivities are comparable to those of conventional metals such as Cu and Ag.

Table 2.1. List of resistivity values at 300 K of 4*d*-5*d* TMOs.

Product	Resistivity [Ω cm] @ 300 K	Ref.
$SrNbO_3$	$2.8×10^{-5}$	[25]
$SrMoO_3$	$5.1×10^{-6}$	[26]
RuO_2	$\sim 3×10^{-5}$	[27,28]
$SrRuO_3$	$2.0×10^{-4}$	[29]
Sr_2RuO_4	$1.0×10^{-4}$	[30]
ReO_3	$9.0×10^{-6}$	[31]
IrO_2	$1.2×10^{-4}$	[32]
Cu metal	$1\sim2×10^{-6}$	[33]
Ag metal	$1\sim2×10^{-6}$	[31]

Particularly, the physical properties of ruthenium oxides are remarkably different from those of 3*d* TMOs, as follows. $SrRuO_3$ is metallic and ferromagnetic with a Curie temperature of 160 K [29,34], which is exceptionally high as 4*d* TMOs. Assuming that the four *d* electrons of Ru^{4+} are all localized with low spin configuration, the magnetic moment per Ru atom should be 2 μ_B. Contrary to this prediction, the experimental magnetic moment per Ru atom is 1.0-1.5 μ_B [35–38]. According to the Kanamori-Goodenough rule, $SrRuO_3$ should be antiferromagnetic since it has Ru-O-Ru bonding with a bond angle of nearly 180°. The isostructural $CaRuO_3$ is also metallic [39,40]. Ca

has a smaller ionic radius than Sr, so that the substitution of Sr for Ca causes bending of the Ru-O-Ru bond from 180°. The distorted structure of $CaRuO_3$ could reduce antiferromagnetic interaction between Ru^{4+}, which could relatively stabilize the ferromagnetic state. Experimentally, however, no apparent magnetic ordering is reported in $CaRuO_3$ [35,40,41]. Previous research points out the relationship between magnetism and extended $4d$ orbitals in $SrRuO_3$ and $CaRuO_3$. Band theory studies suggest that its relatively extended $4d$ orbitals make $SrRuO_3$ a Stoner ferromagnet due to the strong hybridization between Ru $4d$ and O $2p$ orbitals [42–44]. It is also suggested that the distorted structure of $CaRuO_3$ reduces the hybridization between Ru and O and thus weakens the ferromagnetic interaction [44].

Another unique phenomenon of ruthenium oxides is MIT in layered perovskite ruthenium oxides A_2RuO_4 (A = Ca, Sr). The mechanism of MIT cannot be explained by modulation of electron correlation or band filling in $3d$ TMOs. While pristine Ca_2RuO_4 is an insulator below ~350 K, it becomes a metal above that temperature [45,46]. Partial substitution of Ca by Sr also makes the ground state metallic in the whole temperature region [47,48]. It was proposed that the MIT in A_2RuO_4 originates from the change of crystal field splitting with rearrangement of electric configuration [49]. Here I compare the electronic configurations of insulating Ca_2RuO_4 and metallic Sr_2RuO_4 to understand the mechanism of MIT. (Figure 1.2.2). A RuO_6 octahedra in Ca_2RuO_4 is remarkably flattened due to a small ionic radius of Ca^{2+}. The length of Ru-O1 is longer than that of Ru-O2. In this environment, the three t_{2g} orbitals split into lower xy orbital and higher xz, yz orbitals, resulting in the situation that the xz, yz orbitals eacn have one electron. This integer occupation makes Ca_2RuO_4 a Mott insulator due to the Coulomb repulsion between electrons. On the contrary, a RuO_6 octahedra in Sr_2RuO_4 is not significantly

distorted and the Ru-O1 bond is almost as long as the Ru-O2. In this surroundings, the t_{2g}

orbitals are still triply degenerated, resulting in metallic conductivity.
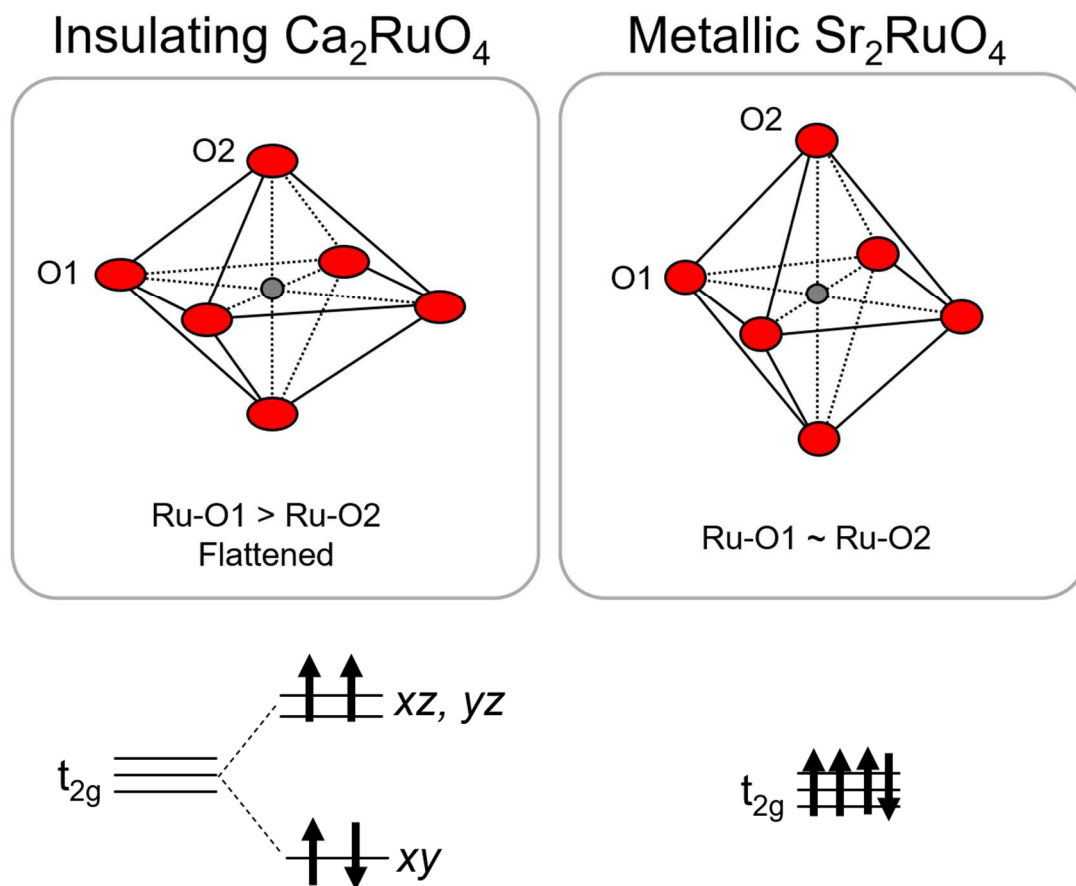
Figure 1.2.2 Schematic illustration of RuO_6 octahedra and schematic diagrams of d^4 configurations in insulating Ca_2RuO_4 and metallic Sr_2RuO_4.

Moreover, Sr_2RuO_4 is famous for its superconductivity below 1.5 K with anomalous pairing symmetry [50–52]. Although it is isostructural to copper oxide superconductors like $La_{2-x}Ba_xCu_2O_4$, there are many differences between them. First, carrier doping is not necessary for the emergence of superconductivity in Sr_2RuO_4, whereas it is critical for cuprates. The σ* antibonding state between Cu $3d$ and O $2p$ is responsible for the superconductivity in cuprates, while the π* antibonding state between Ru $4d$ and O $2p$ plays a role in ruthenate. Besides, the former σ* bonding is non-degenerated, whereas the latter π* bonding is composed of three $4d$ orbitals degenerates. A unique feature of the superconductivity in Sr_2RuO_4 is the spin-triplet superconductivity [51,52], where the spin degree of freedom does not disappear. In the conventional Bardeen-Cooper-Schrieffer (BCS) theory, superconductivity is caused by the condensation of two electrons forming a pair called a Cooper pair. The spins of the two electrons are antiparallel to each other, and so the Cooper pairs have zero net spin. Therefore, there is no need to consider the spin degrees of freedom. Meanwhile, the two-electron forming Cooper pair have parallel spin in Sr_2RuO_4. The origin of the spin-triplet superconductivity has been intensively studied since its discovery, offering many insights into the superconductivity in TMOs.

Large spin-orbit interaction (SOI) largely influences the physical properties of $4d$-$5d$ TMOs. One typical example is Sr_2IrO_4, whose crystal structure is shown in Figure 1.2.3(a). Usually, since electrons in $5d$ orbitals are more spatially extended than that in $3d$ orbitals and largely overlap with each other, they suffer from less Coulomb interaction (U) and have a larger bandwidth (W), resulting in metallic state in $5d$ TMOs. However, large SOI of Ir makes Sr_2IrO_4 an insulator [53,54]. Figure 1.2.3(b) shows the electric

15

configuration of Ir^{4+} in Sr_2IrO_4. The five $5d$ orbitals firstly spit into e_g and t_{2g} states by the crystal field, and then further split into $J_{eff} = 1/2$ and $J_{eff} = 3/2$ by the large SOI. The higher energetic $J_{eff} = 1/2$ state is occupied with only one electron, and this integer occupation makes Sr_2IrO_4 a Mott insulator due to the Coulomb repulsion between electrons. Besides, theoretical calculations predict that superconductivity is induced by carrier doping. [55,56].
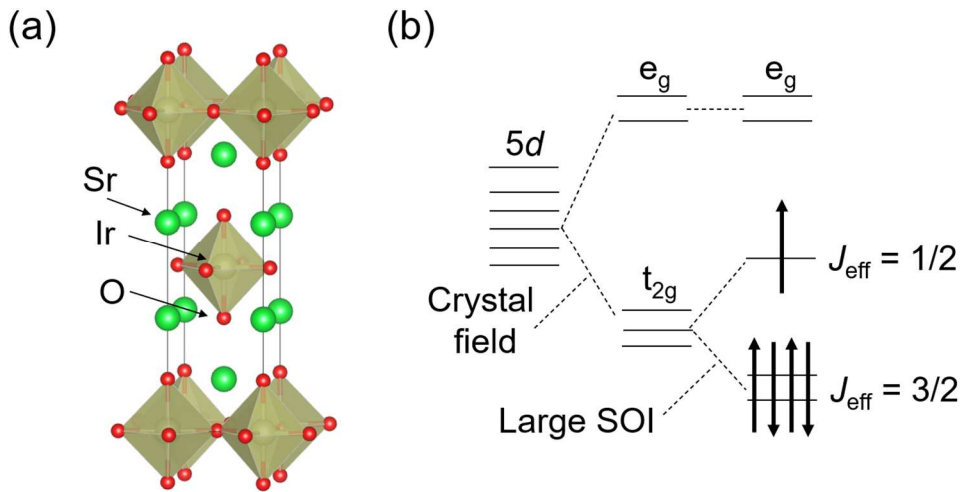
Figure 1.2.3 (a) Crystal structure of Sr_2IrO_4.
(b) Schematic diagram of electronic configuration of Ir^{4+}.

Iridium oxides are also closely related to a hot topic, topological physics, due to their large SOI. For example, pyrochlore $Pr_2Ir_2O_7$, whose crystal structure is shown in Figure 1.2.4 (a), has been intensively studied because theoretical investigation has demonstrated the possibility that many unique topological phases and phenomena such as a topological insulator or quantum spin hall effect could emerge [57]. These features are based on its unique band structure, as schematically shown in Figure 1.2.4(b). The valence band and the conduction band of $Pr_2Ir_2O_7$ touch at one point with quadratic energy dispersion as a result of the combination between Coulomb repulsion and spin-orbit

interaction of Ir. Recently, the Weyl semimetal phase was realized by introducing epitaxial strain and a magnetic field [58]. Figure 1.2.4(c) is the typical band structure of the Weyl semimetal. In the Weyl semimetal, the degenerate valence and conduction bands contact at one point in the Brillouin zone, called the Weyl point. The key feature is a linear dispersion at the Weyl points. Since the linear energy dispersion has never been observed in conventional TMOs with quadratic energy dispersion, unprecedented physical properties are expected. For example, this liner dispersion might lead to mass-less electrons with extremely high mobility.
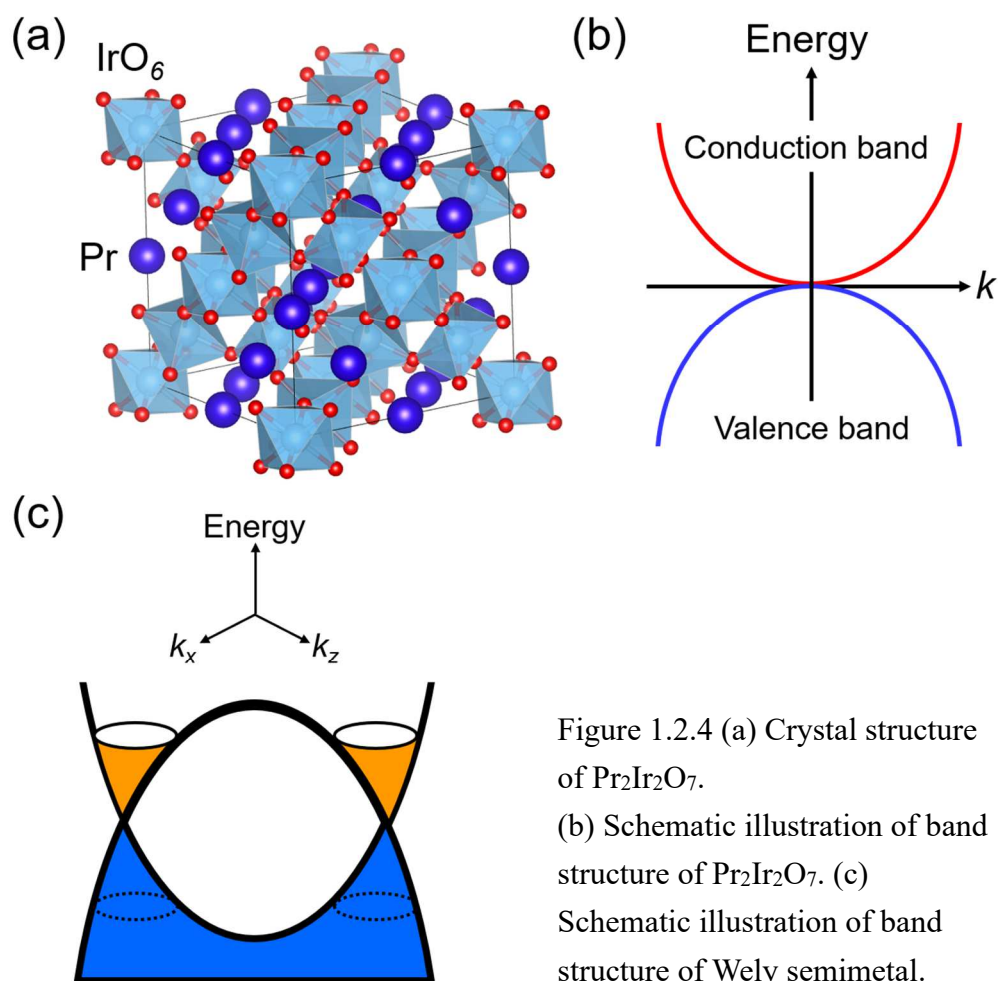
Figure 1.2.4 (a) Crystal structure of $Pr_2Ir_2O_7$.
(b) Schematic illustration of band structure of $Pr_2Ir_2O_7$. (c) Schematic illustration of band structure of Wely semimetal.

1.3 Anion doping into 3*d* transition metal oxides

1.3.1 Brief introduction of anion doping into 3*d* TMOs

As I describe in the previous sections, TMOs have a rich variety of physical properties. Modulation of these properties has vastly been conducted for many purposes such as the deep understanding of underlying physics and functional improvement. There are many techniques for modulation, such as carrier doping, application of external field or high pressure, etc. Recently, anion doping has been proposed as a new method to modulate physical properties [59–62]. The concept of anion doping is illustrated in Fig.1.3.1. In this case, an oxide ion bonded to a central cation is substituted for a different anion, such as hydride ion, fluoride ion, and nitride ion.
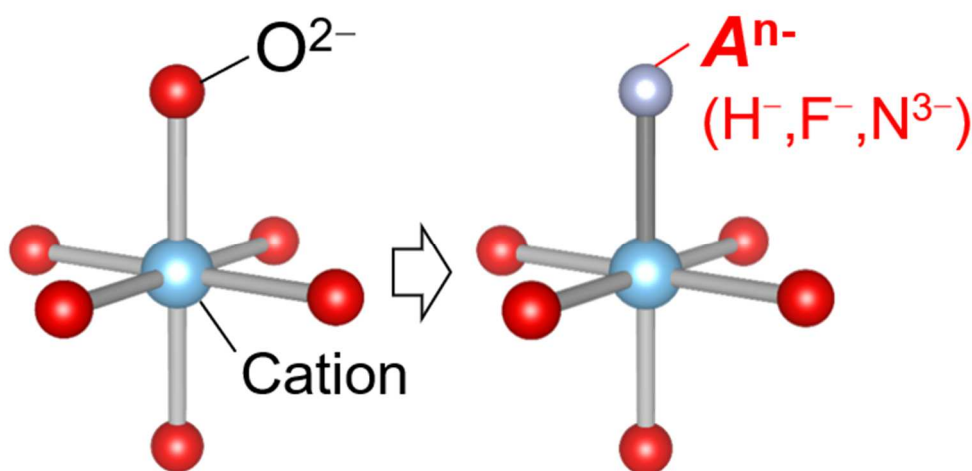
Figure 1.3.1 Concept of anion doping.

The anion doping can tune carrier concentration, bond length, bond angles, as conventional cation doping can do, but it can also modulate many parameters that cation doping cannot modulate. Figure 1.3.2 summarizes parameters that can be modulated by anion doping [59]. For example, anion doping can modulate crystal field splitting even when the octahedron stays rigid (Figure 1.3.2. (a)). Anion doping can increase or decrease the bandgap energy through an upward or downward shift of the valence band maximum (Figure 1.3.2. (b)). Especially, nitrogen doping is widely conducted for visible light photocatalyst because nitrogen doping can decrease the band gap energy due to its higher covalence nature than oxygen. It also gives rise to a cis/trans degree of freedom in MO_4X_2 octahedra (Figure 1.3.2 (c)). For example, trans-type TaO_4N_2 octahedra in $SrTaO_2N$ results in ferroelectricity, whereas cis-type TaO_4N_2 octahedra does not show any ferroelectric order. If anions do not order, it can introduce randomness in the crystal. Local coordination asymmetry is also brought about by anion-doping (Figure 1.3.2 (d)). The O_h symmetry of the rigid octahedron is reduced to lower symmetry, such as C_4 and C_3 symmetry. This symmetry reduction has been applied to the development of phosphor, of which characteristics largely depend on its local structure around the luminescent center. Alternate stacking of layers of different anions has the potential to enhance two-dimensionality (Figure 1.3.2 (g)). For example, $Sr_2CuO_2F_{2+\delta}$ with two-dimensional CuO_2 planes shows superconductivity, and $Sr_2CuO_2Cl_2$ is known as an ideal two-dimensional square lattice quantum magnetic material.

In the following sections, I focus on the modulation of physical properties by fluorine doping and nitrogen doping.
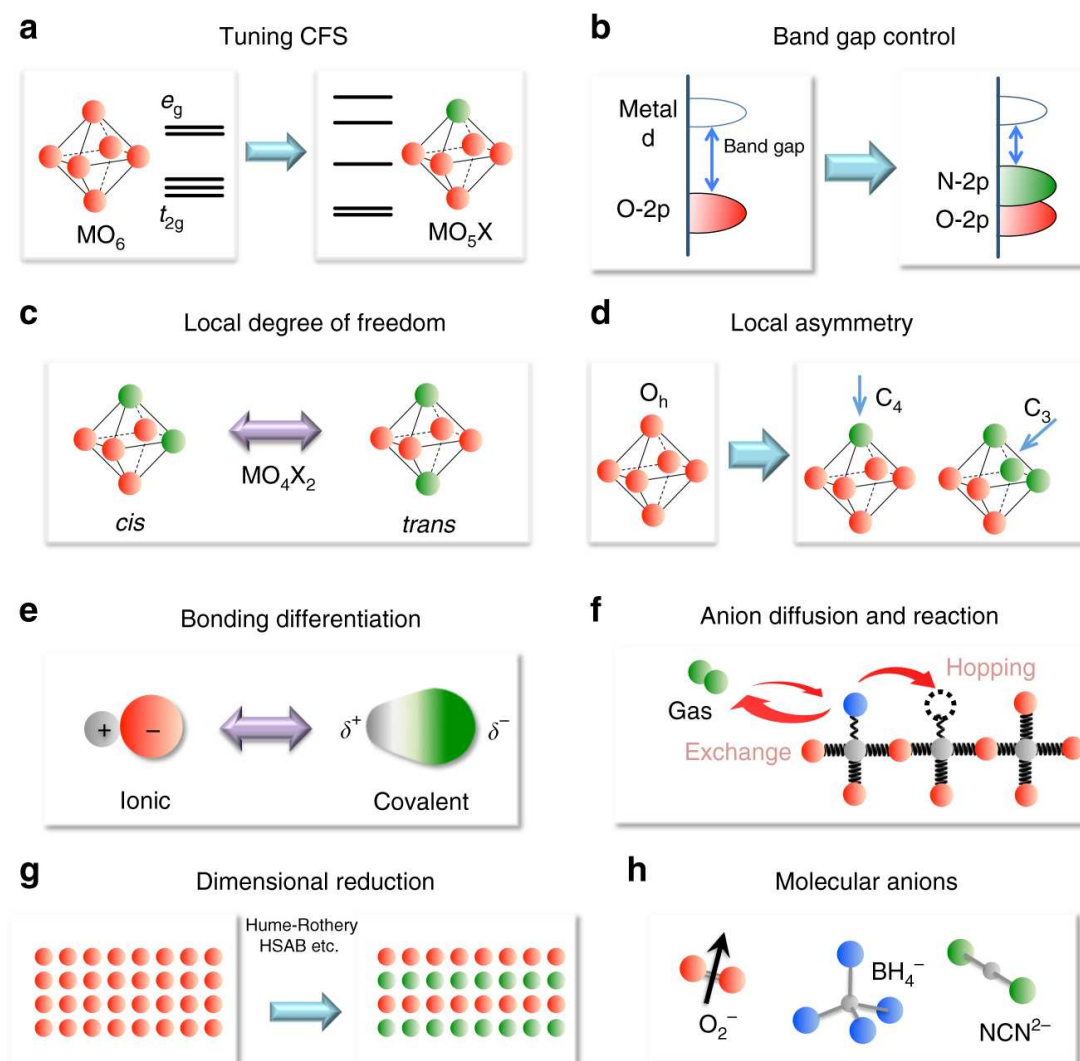
Figure 1.3.2 Parameters which anion doping can tune (a) Crystal field splitting, (b) Band gap, (c) Local degree of freedom, (d) Local asymmetry, (e) Bonding differentiation, (f) Diffusion and reaction (g) Dimensional reduction, (h) Formation of molecular anions fluorine doping. This figure is reproduced with permission from Ref [59]. Copyright 2018 by Springer Nature. (Licensed under CC BY 4.0)

1.3.2 Modulation of physical properties of 3*d* TMOs by fluorine doping

Before introducing physical properties induced by fluorine doping, I briefly explain the coordination chemistry of fluorine doping, as summarized in Figure 1.3.3. There are two types of fluorine doping: substitution of oxygen by fluorine and fluorine insertion into a vacant space. The substitution of oxygen by fluorine is widely observed among fluorine-doped TMOs. The substituted fluorine atoms sometimes order but sometimes do not, depending on compounds. Fluorine insertion into a vacant space is mainly seen in layered perovskite oxyfluorides. Fluorine is inserted into rock salt layers accompanied with the expansion of *c*-axis length.
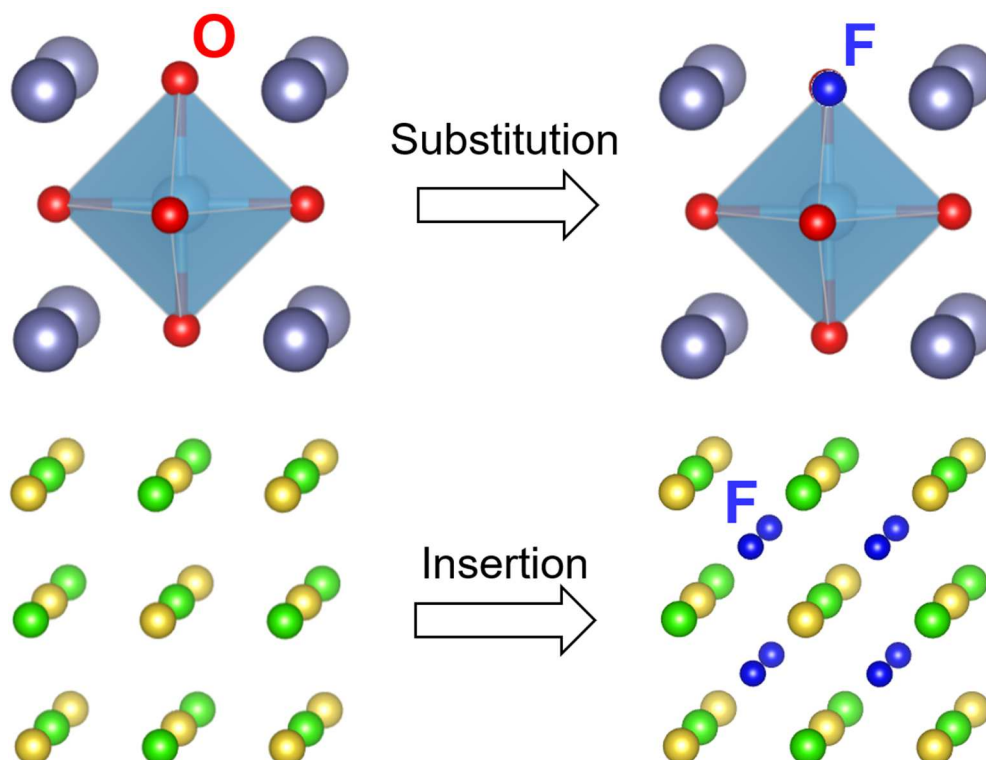
Figure 1.3.3 Two types of fluorine doping. The upper figures illustrate the substitution of oxygen for fluorine. The bottom figures illustrate the insertion of for fluorine into vacant space in a crystal structure.

Modulation of magnetic properties of $3d$ TMOs by fluorine doping has been widely reported so far. A K_2NiF_4-type oxyfluoride Sr_2CoO_3F is a good example. Pristine Sr_2CoO_4, whose crystal structure is shown in Figure 1.3.4 (a), is a metallic ferromagnet with a relatively high Curie temperature of 255 K [63,64]. This ferromagnetism is attributable to Co^{4+} in the CoO_6 octahedra with the intermediate-spin state ($t_{2g}^4 e_g^1$, $S = 3/2$). On the other hand, Sr_2CoO_3F is an insulating antiferromagnet with a reasonably high Neer temperature of 323 K [65–67].

Figure 1.3.4(b) manifests the preferential occupation of fluorine atom in the apical anion site of the CoX_6 octahedra in Sr_2CoO_3F. The random distribution of O and F in the apical site results in the Co-site off-centering, as shown in Figure 1.3.4(c). The strong covalency of oxygen in comparison with F yields a distorted square pyramid of CoO_5, which is loosely bound to one F anion. In this anion coordination, the Co^{3+} cation took the high spin state with the electronic configuration of $(d_{xy})^2(d_{xz}, d_{yz})^2(d_{x2-y2})^1(d_{z2})^1$ [67,68].

Moreover, physical pressure of ~10 GPa induces spin-crossover from high spin state ($S = 2$) to low spin state ($S = 0$) with the change of coordination environment. As the physical pressure is induced, the Co–F bond gradually shrinks, resulting in the transformation from pyramidal CoO_5 to octahedral CoO_5F, as shown in Figure 1.3.4(c). It is very rare that the coordination environment around Co changes in such a rigid crystalline phase by applying physical pressure.
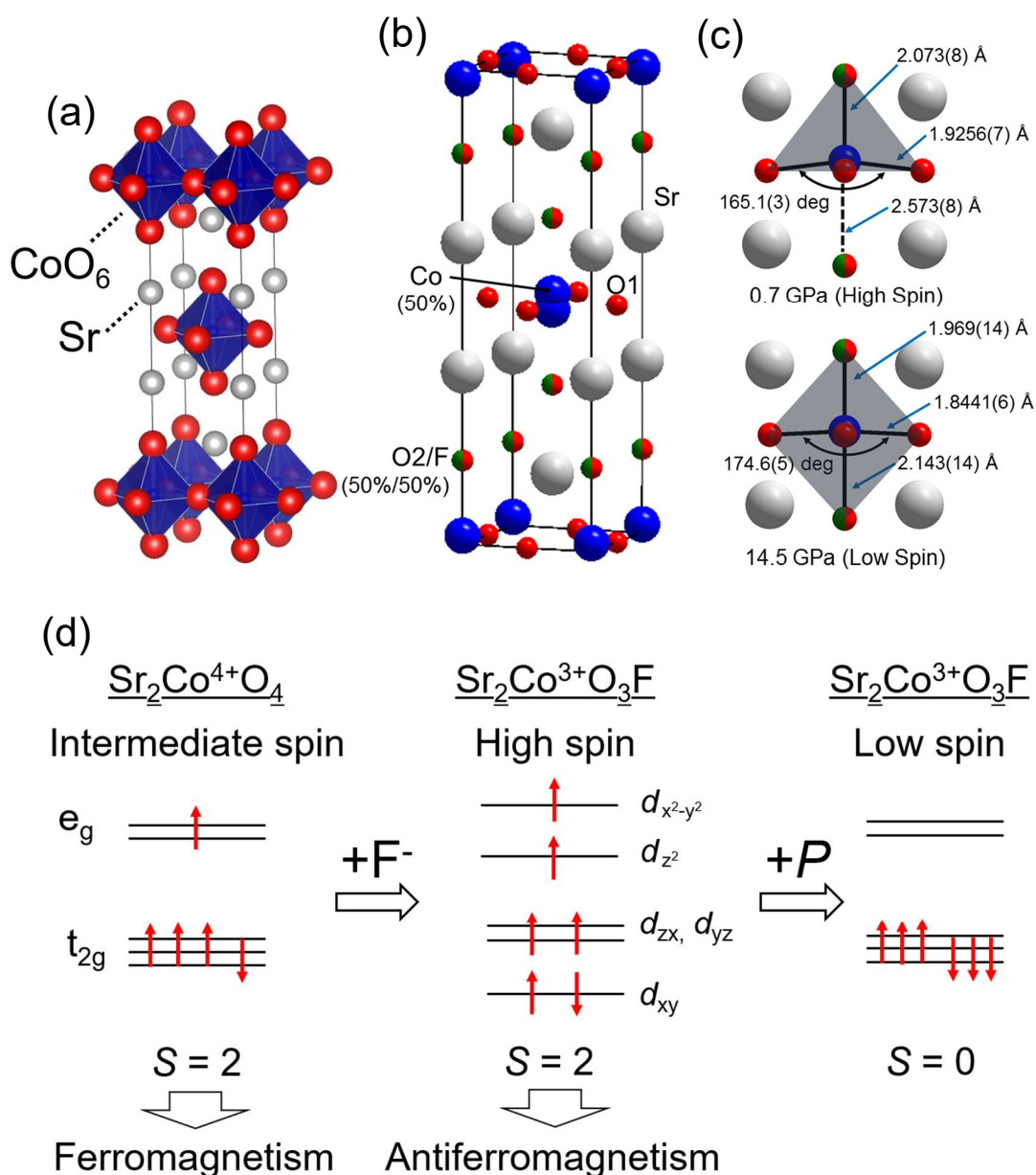
Figure 1.3.4 (a) Crystal structure of Sr_2CoO_4 (b) Crystal structure of Sr_2CoO_3F at ambient pressure Blue, red, green, and grey spheres represent Co, O, F, and Sr atoms, respectively. (c) Local coordination environment around Co center at 0.7 and 14.5 GPa. The gray shade represents the coordination polyhedron. (d) Electric configurations of Sr_2CoO_4, Sr_2CoO_3F at ambient pressure and Sr_2CoO_3F under high pressure, respectively. (b) and (c) are reprinted with permission from [67]. Copyright 2016 by Springer Nature. (Licensed under CC BY 4.0)

Modulation of the local coordination environment in transition metal oxides has also been observed in fluorine-doped iron oxides. Partial substitution of fluorine for oxygen in Fe-based hexagonal perovskite (FHP) oxides lead to robust antiferromagnetic ordering with a high Neer temperature (T_N) of ~ 700 K [69]. Pristine Fe-based hexagonal perovskite oxides such as 6H-BaFeO$_{3-\delta}$ [70], 12H-BaFeO$_{3-\delta}$ [71], and BaFeO$_{2.95}$ [72] are antiferromagnetic with Neer temperature of 130 K, 270 K, and 180 K, respectively, which are much lower than that of fluorine-doped one. Therefore, it is natural to infer that fluorine plays an important role in the robust antiferromagnetic ordering.

Here, I pick up one example of fluorine-doped FEP oxides, (Ba, Sr)FeO$_{2.4}$F$_{0.2}$, which exhibits antiferromagnetic ordering with T_N of 680 K. A small amount of Sr with a smaller ionic radius than Ba is added in order to maintain the hexagonal structure. The crystal structure of 6H-BaFeO$_3$ is shown in Figure 1.3.5(a), which helps understand the basic structure of hexagonal perovskite. The fundamental components of the structure are single FeO$_6$ octahedra and plane-shared octahedral dimers, which are alternately stacked in the vertical direction. The crystal structure and spin structure of (Ba, Sr)FeO$_{2.4}$F$_{0.2}$ are shown in Figure 1.3.5(c). Fluorine doping causes a drastic change in the plane-shared octahedral dimers, as shown in Figure 1.3.5(c). That is, the plane-shared octahedral dimers change into the combination of edge-sharing pyramids and corner-sharing tetrahedras.

Two concomitant effects of fluorine incorporation can explain the origin of the robust antiferromagnetism. One effect is the enhancement of superexchange interaction between Fe and O ions due to the reduction of Fe^{4+} into Fe^{3+}. The antiferromagnetic coupling would be enhanced by an increase of spin momentum from S = 4 of Fe^{4+} to S = 5/2 of Fe^{3+}. The other effect is the modification of the Fe-O-Fe connectivity. When

fluorine is introduced, the octahedron transforms into tetrahedral pairs via pyramidal dimers. At the same time, the bond angel of Fe-O-Fe approaches 180° by fluorine doping. This structural modulation results in the enhancement of antiferromagnetic superexchange interaction, as the Kanamori-Goodenough rule predicts.

The two examples mentioned above demonstrate that the magnetism could be significantly manipulated by fluorine doping into 3d TMOs through the reduction of the valence state and modulation of the coordination chemistry. Especially, the modulation of the coordination environment around transition metal ions cannot be realized by cation doping. Therefore, fluorine doping is a promising technique to module the physical properties of 3d TMOs.
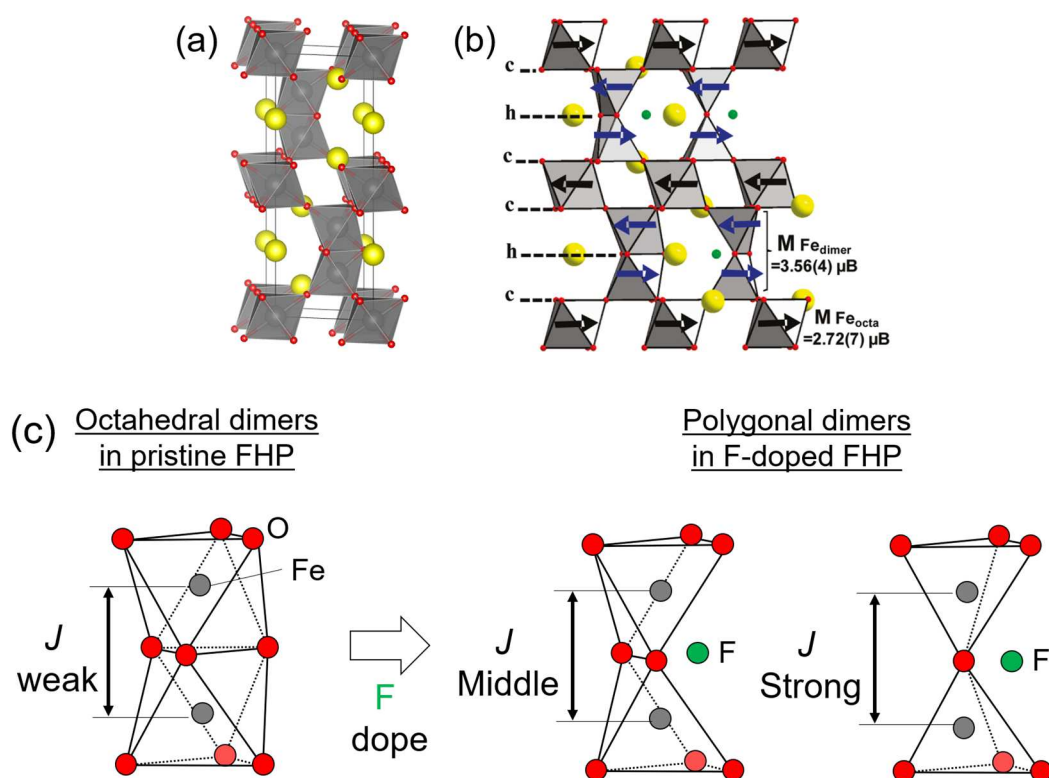
Figure 1.3.5 (a) Crystal structure of 6H-BaFeO$_3$ (b) Crystal structure and magnetic structure of the partially fluorinated 6H-polytype with mixture of several Fe configurations. (c) Schematic image of dimers in F-doped FEP. (b) is reprinted with permission from [67]. Copyright 2011 by the American Chemical Society.

1.3 Anion doping into 3d transition metal oxides

Fluorine doping can tune electric transport properties of $3d$ TMOs. Since the negative charge of fluoride ion, -1, is smaller than that of oxide ion, -2, the substitution of oxygen by fluorine causes electron doping. For example, fluorine doping into $SrCrO_{3-\delta}$ and $SrFeO_{3-\delta}$ lead to $SrCrO_{2.4}F_{0.6}$ and $SrFeO_{3-\alpha}F_{\gamma}$ of which resistivity values are decreased [73,74]. Fluorine doping into $NdNiO_3$ yields to $NdNiO_2F$, accompanied with metal to insulator transition [75]. Furthermore, fluorine doping can also induce superconductivity in oxides with layered structures. Excess fluorine atoms residing at the interstitial site in layered perovskite $Sr_2CuO_2F_{2+\delta}$ generate hole carriers, and the system undergoes a phase transition from Mott insulator to superconductor under 41 K [76]. $LaFeAsO_{1-x}F_x$ is the first example of iron oxide superconductor.
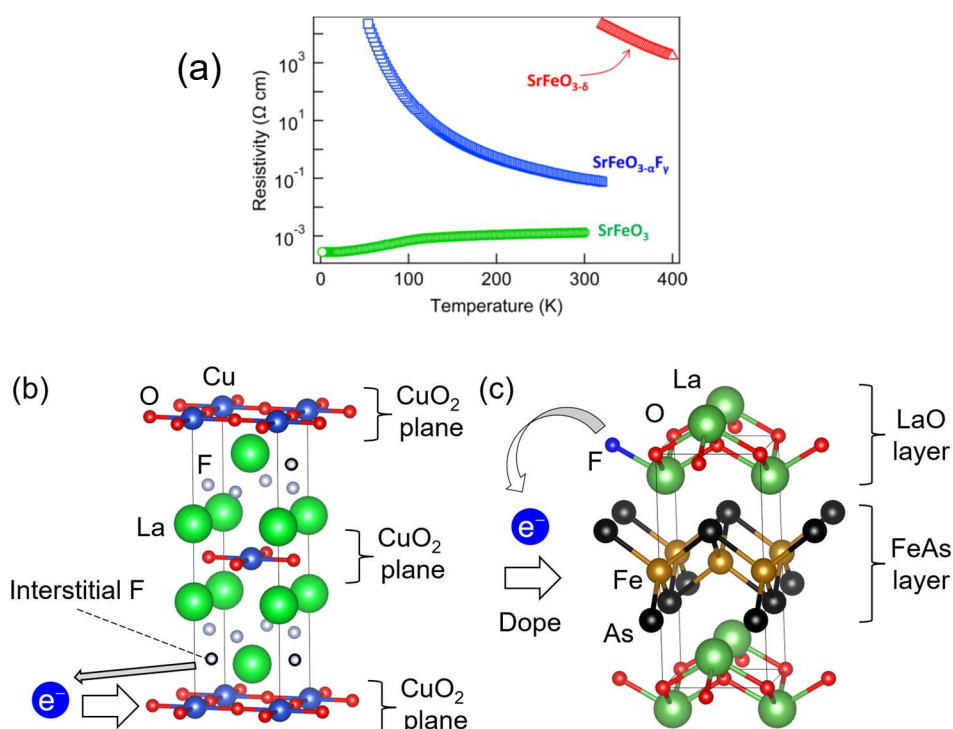
Figure 1.3.6 (a) Resistivity as a function of temperature of $SrFeO_3$ (green), $SrFeO_{3-\alpha}F_{\gamma}$ (blue), and $SrFeO_{3-x}$ (red) thin films (b) Crystal structure of $Sr_2CuO_2F_{2+\delta}$. (c) Crystal structure of $LaFeAsO_{1-x}F_x$. (a) is reprinted with permission from [72], Copyright 2014 by the American Chemical Society.

1.3.3 Modulation of physical properties of 3*d* TMOs by nitrogen doping

Nitrogen doping is possible only when oxygen is replaced by nitrogen. In usual cases, the doped nitrogen atoms are random distribution in the crystal, as shown in Figure 1.3.7. The randomness associated with nitrogen doping often governs the physical properties of nitrogen-doped 3*d* TMOs.
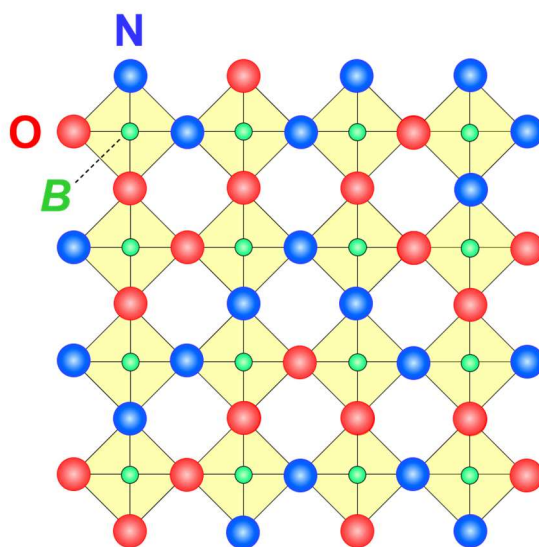
Figure 1.3.7 Schematic image of nitrogen random distribution in a crystal structure.

The effect of random nitrogen distribution on electron transport properties is seen in nitrogen-doped perovskite $LaVO_3$. Figure 1.3.8(a) compares the crystal structures of cation-doped and anion-doped $LaVO_3$. The mother compound $LaVO_3$ is a typical Mott insulator. It transforms into a metal by hole doping through substitution of an alkali earth element for La ($La_{1-x}Sr_xVO_3$ or $La_{1-x}Ca_xVO_3$). On the contrary, when nitrogen is doped into $LaVO_3$ ($LaVO_{3-x}N_x$; LVON), no insulator to metal transition occurs, and LVON still remains semiconducting [77]. This situation is more clearly seen from the temperature dependence of resistivity, as shown in Figure 1.3.8(b). In cation doping, an insulator to metal transition occurs at a relatively lower substitution level, $x = 0.2$ for $La_{1-x}Sr_xVO_3$.

On the other hand, LVON shows insulating behavior in the whole temperature region even at a high doping level. The carrier conduction in LVON can be described by the variable range hopping mechanism. This implies that the doped carriers are essentially localized in narrow special regions and that they move by hopping from a localized site to another. It is suggested that the substitution of nitrogen for oxygen induces a strong random potential in the VX_6 conduction path through the difference in charge and covalency between oxygen and nitrogen, and that the random potential localizes the carriers. As seen from the case of LVON, nitrogen doping could modulate the transport properties of $3d$ TMOs through carrier localization.
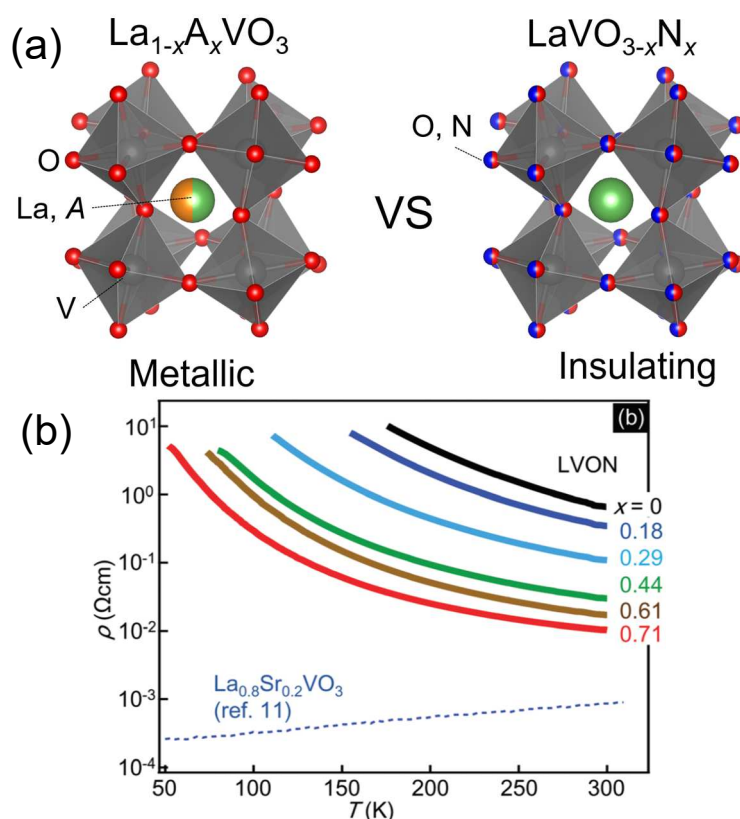
Figure 1.3.8 (a) Comparison between the conventional research of $La_{1-x}A_xVO_3$ and $LaVO_{3-x}N_x$ (b) ρ- T curves for the $LaVO_{3-x}N_x$ thin films grown on an LSAT (001) substrate (solid lines) and single-crystalline $La_{0.8}Sr_{0.2}VO_3$ (dashed line). (b) is reprinted with permission from [75]. Copyright 2017 by Royal Society of Chemistry.

Random distribution of nitrogen is also closely related to magnetism. It is known that $MnTaO_2N$ exhibits a unique magnetic structure, which cannot be seen in oxides with similar structures [78]. Figure 1.3.9(a) shows the crystal structure of $MnTaO_2N$, which takes the $LiNbO_3$-type structure with a random distribution of oxygen and nitrogen anions. Mn in $MnTaO_2N$ is divalent with d^5 configuration and $S = 5/2$. The Mn^{2+} ions exhibit a nontrivial helical spin order, as shown in Figure 1.3.9(b). The Mn^{2+} moments lie in the ab plane, which are parallel to each other. These ferromagnetic layers are stacked along the c axis with a rotation of 160° at 6 K, which is different from the conventional G-type order observed in other perovskite oxides and $LiNbO_3$-type oxides, where all spins are antiparallel to each other.

It has been pointed out that the mixed anion nature plays an important role in the helical spin structure. One distinctive feature of $MnTaO_2N$ is that it has many different magnetic couplings. In $MnTaO_2N$, Mn and anions form a ring, as shown in Figure 1.3.9(c). Since oxygen and nitrogen are randomly distributed, the ring structure varies depending on the number of anions and/or the positions of anions. This random distribution of oxygen and nitrogen may affect the local structure, such as bond length, octahedral tilting, and so on, which vary the magnitude of magnetic interaction. Besides, theoretical calculation suggested that the magnitude of the magnetic interaction in Mn–N–Mn bonds is four times larger than that of the Mn–O–Mn bonds, mainly due to the covalent nature of Mn–N bonds [79]. These multiple magnetic interactions with different strengths may enhance spin frustration and give the nontrivial spin ordering in $MnTaO_2N$. This example demonstrates that nitrogen doping is a promising strategy to realize unconventional magnetic structures in $3d$ TMOs.
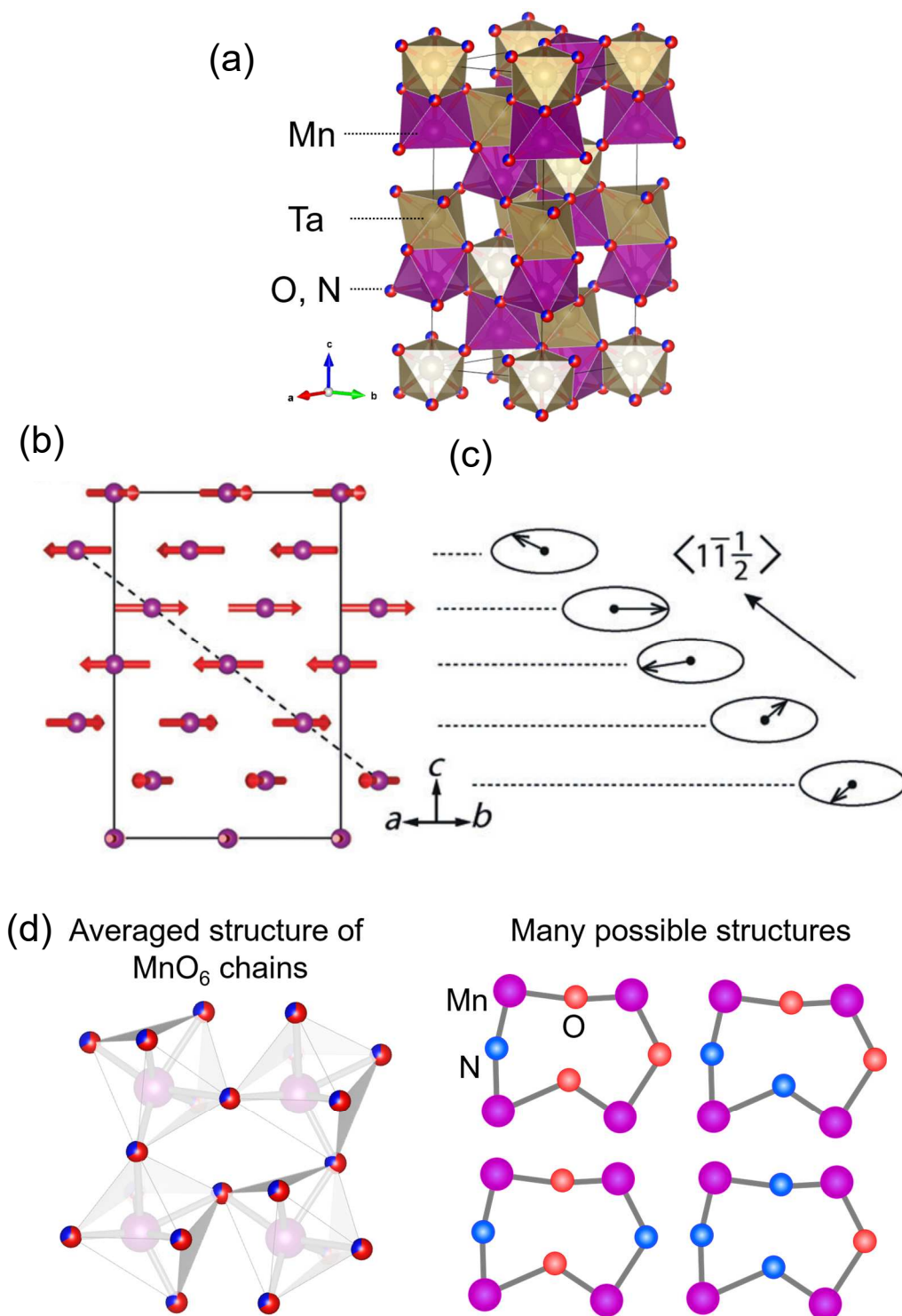
Figure 1.3.9 (a) Crystal structure of $MnTaO_2N$. (b) Helical spin structure of $MnTaO_2N$ with a propagation vector of [0,0,0.356] at 6 K. (c) The spin rotation along <1, -1 1/2>. (d) Mn chain in $MaTnO_2N$. (b) and (c) are reprinted with permission from [76]. Copyright 2014 by Weily Online Library.

1.4 Anion doping into **4*d*-5*d*** transition metal oxides

Anion doping into 4*d*-5*d* TMOs has rarely been reported compared with anion doping into 3*d* TMOs. Here, I introduce some unique physical properties of anion doped 4*d*-5*d* TMOs.

Fluorine doping into $RbLaNbO_7$ ($RbLaNbO_6F$) drastically decreases the resistivity [80], where oxygen is suggested to be randomly substituted by fluorine. Despite the reduction of Nb from 5+ to 4+ and the abrupt reduction of electric resistivity, it shows semiconducting behavior based on variable range hopping mechanism, suggesting strong carrier localization in the Nb-(O, F) network.

More interesting changes in the physical properties can be seen in fluorine doping into layered perovskite ruthenium oxides, $Sr_3Ru_2O_7$ and Sr_2RuO_4 [81,82]. Figure 1.3.10(a) shows how the crystal structure of $Sr_3Ru_2O_7$ is modified by fluorine doping. The doped fluorine atoms are inserted into the SrO rocksalt layer together with the oxidation of Ru from 4+ to 5+. This fluorine doping causes a ferromagnetic to antiferromagnetic transition. Figure 1.3.10(b) shows the magnetic susceptibilities of $Sr_3Ru_2O_7F_2$, $Sr_3Ru_2O_7$, and $SrRuO_3$-CuF_2. A peak is recognizable around 90 K in the ZFC magnetization curve of $Sr_3Ru_2O_7$, which is assignable to the ferromagnetic transition. (A peak around 170 K is due to ferromagnetic impurity of $SrRuO_3$.) Meanwhile, fluorinated $Sr_3Ru_2O_7F_2$ shows a distinct rise in the susceptibility at 185 K, indicating that ferromagnetic behavior appears below the temperature.

The ferromagnetic behavior seen in $Sr_3Ru_2O_7F_2$ can be rationalized by Dzyaloshinsky–Moriya spins canting mechanism, which is related to the antiferromagnetic coupling between Ru spins [81]. The origin of the magnetic transition can be attributed to two effects: structural modulation and reduction of Ru ion. The rotation angle of RuO_6 octahedra in the $Sr_3Ru_2O_7F_2$ is 11~13°, which is much larger than that in $Sr_3Ru_2O_7$, 7°. This larger rotation could weaken the Ru $4d$ - O $2p$ hybridization, resulting in a decrease of ferromagnetic couplings. Additionally, the oxidation of Ru valence from 4+ to 5+ could realize the situation of exactly half filled t_{2g} orbitals in Ru^{5+} with $4d^3$ electronic configuration. This configuration favors the antiferromagnetic ordering between Ru ions through superexchange interactions Ru $4d$–O $2p$–Ru $4d$. Therefore, structural modification and filling control by fluorine doping is a useful way to manipulate the magnetic ground states in $4d$-$5d$ TMOs.
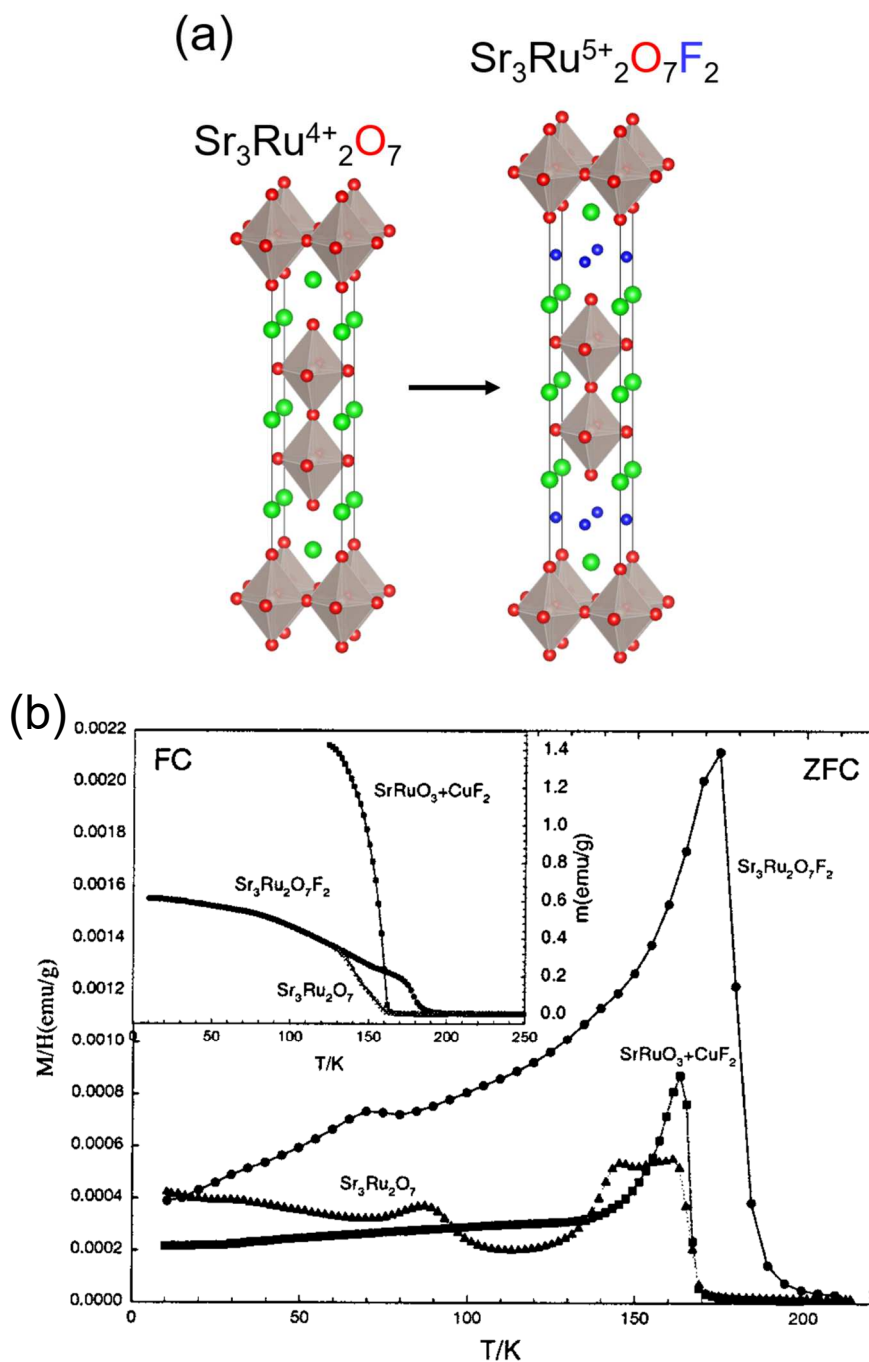
Figure 1.3.10 (a) Crystal structure modulation of $Sr_3Ru_2O_7$ by fluorine doping
(b) Magnetic susceptibilities (ZFC) of $Sr_3Ru_2O_7F_2$, $Sr_3Ru_2O_7$, and $SrRuO_3+CuF_2$.The inset shows the field cooled magnetizations of the samples. the scale of the ZFC curve of $SrRuO_3$ has been reduced to 1/20 and all the measurements were performed with an applied field of 200 G except for $SrRuO_3$, where the applied field is 10 G. (b) is reprinted with permission from [79]. Copyright 2000 by the American Physical Society.

33

Fluorine doping into Sr_2RuO_4 modulates the physical properties differently. Figure 1.3.11(a) shows the crystal modulation of Sr_2RuO_4 by fluorine doping. Doped fluorine is not only inserted into the SrO layer but also substituted for oxygen, and, as a consequence, the Ru valence state is maintained at 4+. Figure 1.3.11(b) compares the temperature dependence of resistivity before and after doping. Despite the maintenance of the Ru valence, the ground state changed from a metallic state to a highly insulating state, where the resistivity increases by 10,000 times [82].

According to theoretical calculations, the MIT can be understood by the change of coordination environment around Ru^{4+} [83]. Figure 1.3.11(c) schematically summarizes RuX_6 octahedra with electric configuration before and after fluorination. Detailed analyses of partial density of states reveal that the four $4d$ electrons of Ru^{4+} occupy the three t_{2g} bands in Sr_2RuO_4, while they occupy the four bands of $(d_{xy})^1(d_{yz}, d_{zx})^2(d_{z2})^1$ in $Sr_2RuO_3F_2$. In the latter configuration, only one electron occupies the d_{z2} orbital, and the system turns into a Mott insulating state. This anomalous occupation of the d_{z2} orbital can be explained by modulation of the crystal field around Ru ions. The RuO_6 octahedra in Sr_2RuO_4 are not subjected to large distortion, and the five $4d$ orbitals split into t_{2g} and e_g orbitals. All the four d electrons occupy the t_{2g} bands, resulting in a metallic state. After fluorination, the Ru−F bonds in the RuO_5F octahedra are elongated, which stabilizes the d_{z2} orbital. As mentioned in this section, structural modulation by fluorine doping can tune the transport properties of $4d$ TMOs.
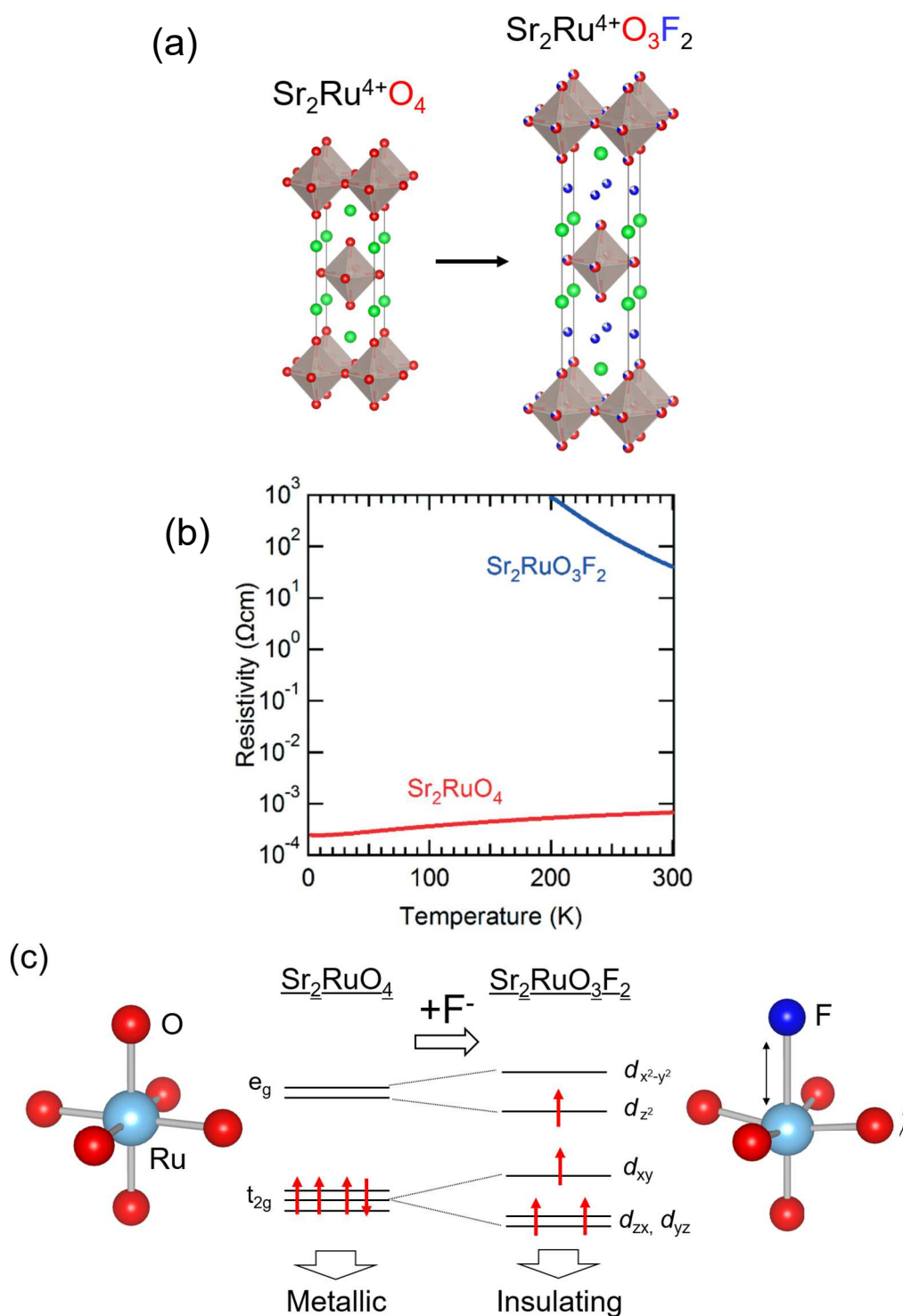
Figure 1.3.11 (a) Crystal structure modulation of Sr_2RuO_4 by fluorine doping (b) Temperature dependence of the resistivity for the Sr_2RuO_4 (red line) and $Sr_2RuO_3F_2$ (blue line). (c) Possible electric configuration of Sr_2RuO_4 and $Sr_2RuO_3F_2$. (b) is reprinted with permission from [80]. Copyright 2018 by Rolyal Society of Chemistry.

Interestingly, $SrNbO_2N$ (the crystal structure is shown in Figure 1.3.12) shows a large positive magnetoresistance at 2 K with a MR ratio of 50 % [84]. Although a positive MR effect is also seen in $SrNbO_3$, the MR ratio is as low as 3 %. The mechanism of MR in $SrNbO_3$ can be explained by the classical theory based on the Lorentz force applied to electrons, where the MR ratio is proportional to $(\mu B)^2$. However, this classical theory cannot explain the large positive MR in $SrNbO_2N$; According to the classical theory, the MR ratio of $SrNbO_2N$ should be smaller than that of $SrNbO_3$ because its carrier mobility is lower than that of $SrNbO_3$. Randomly distributed nitrogen in the crystal would induce many scattering centers in the conduction pathway, resulting in lower carrier mobility in $SrNbO_2N$. However, the MR ratio is enhanced by nitrogen doping. As a possible origin of this positive MR, the wave-function shrinking model has been proposed. In this model, the applied magnetic field causes shrinkage of localized orbitals and reduces the probability of electron hopping, which increases resistance. Therefore, nitrogen doping has the potential to induce unconventional physical properties in $4d$-$5d$ TMOs related to carrier localization.
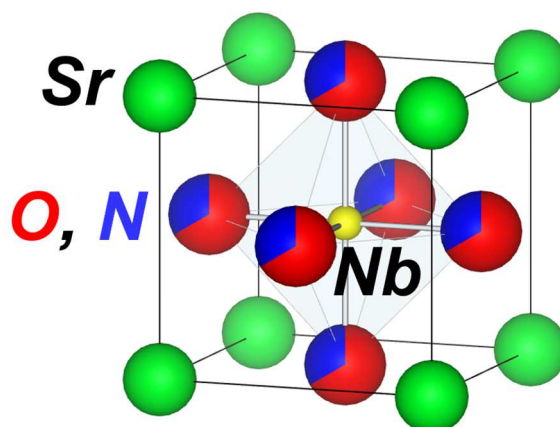
Figure 1.3.12 Crystal structure of $SrNbO_2N$,
where oxygen and nitrogen are supposed to randomly distribute.

Perovskite oxynitride exhibits not only positive magnetoresistance but also negative magnetoresistance. $EuNbO_2N$ and $EuWO_{1+x}N_{2-x}$ (the crystal structure is shown in Figure 1.3.13) are famous for their colossal negative magnetoresistance up to -99 % at low temperatures [85–87], as shown in Figure 1.3.14. A key to the negative MR is Eu^{2+}, which has large localized spins due to its $4f^7$ electron configuration. Both oxynitrides show ferromagnetic transition around 5-10 K, originating from the large localized spin of Eu^{2+}, and semiconducting transport properties. Interestingly, the negative MR does not depend on the carrier type; it is observed in both electron-doped $EuNbO_2N$ and hole-doped $EuWON_2$ ($EuWO_{1.04}N_{1.96}$), where the electron carriers in the former may be produced by slight nitrogen deficiency, and the hole carriers in the latter is by excess nitrogen. The interplay between localized spins at Eu^{2+} and itinerant carriers is thought to be a key to the colossal magnetoresistance.
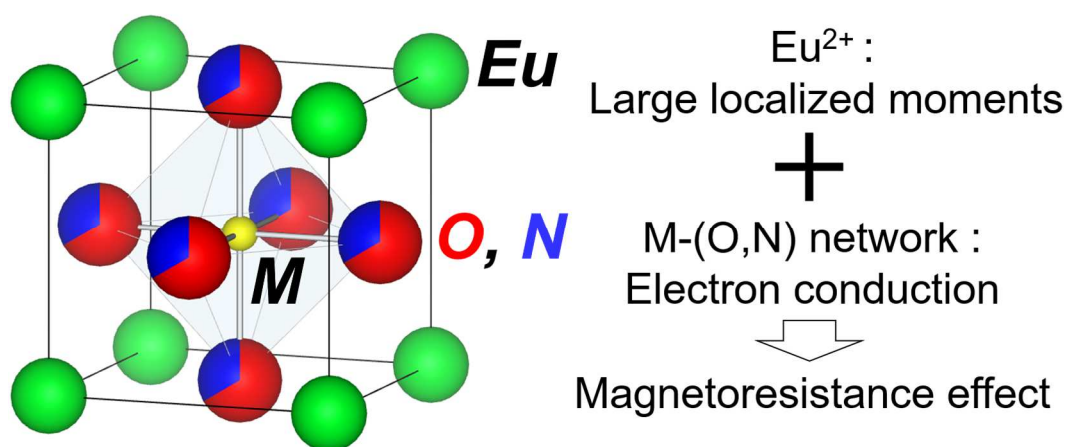
Figure 1.3.13 Crystal structure of Eu*M*(O,N)$_3$,
where oxygen and nitrogen are supposed to randomly distribute, and two key parameters in the oxynitride, large magnetic moments and electron conduction.
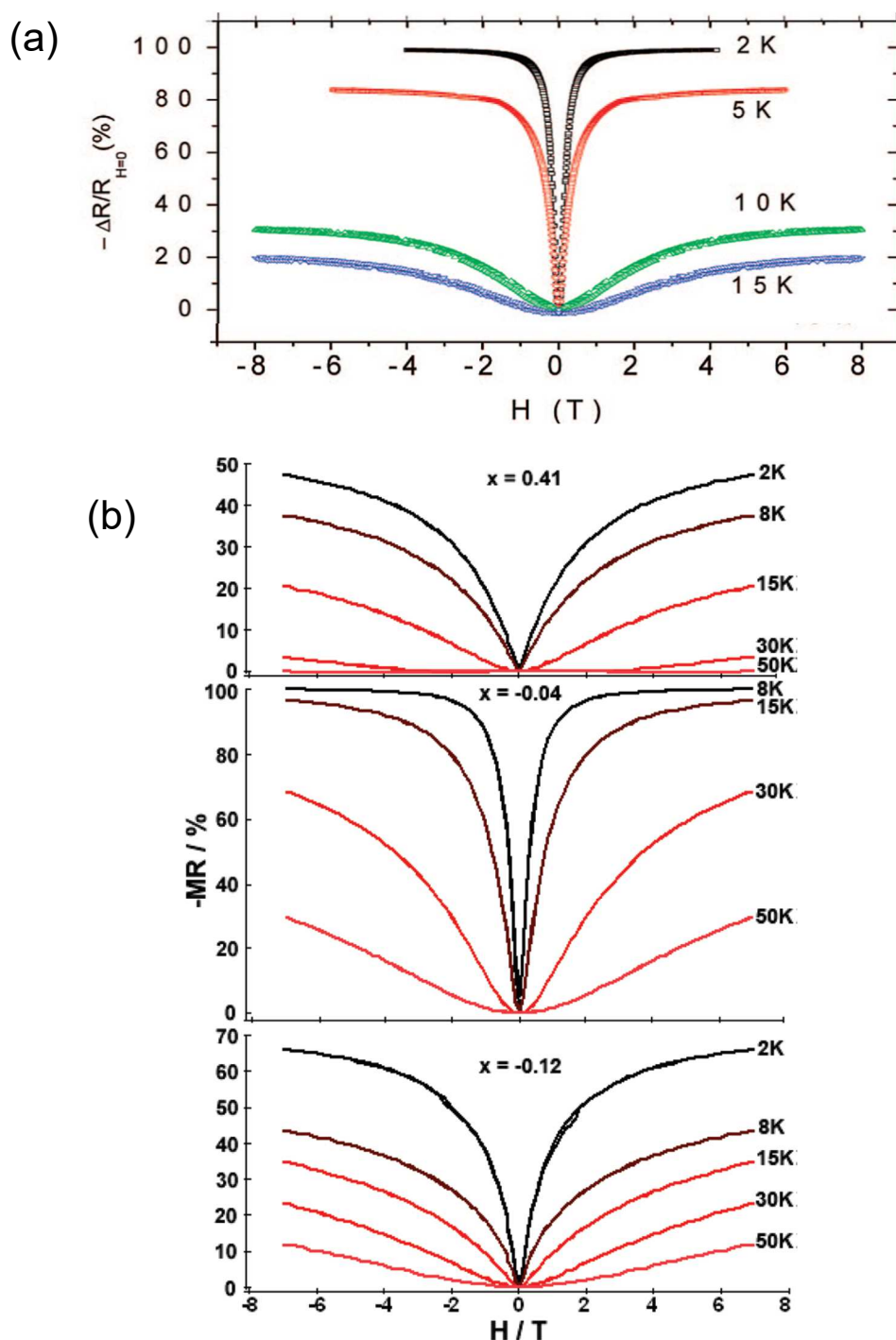
Figure 1.3.14 (a) Magnetic field dependence of the magnetoresistance of $EuNbO_2N$. (b) Magnetic-field variations of negative magnetoresistances for $EuWO_{1+x}N_{2-x}$ (x = 0.41, -0.04, and -0.12). (a) and (b) are reprinted with permission from [83] and [85], respectively. Copyright 2008 and Copyright 2010 by the American Chemical Society.

38

1.5 Merits of thin films

Usually, polycrystalline powders and small pieces of single crystals are used in materials science research. However, in this study, I adopted thin films because it has superiorities in both the synthesis of sample and the measurement of physical properties.

In the viewpoint of sample preparation of anion-doped oxide compounds, thin film form has two notable merits. Firstly, it can more easily prepare a single-phase sample than polycrystalline powder form. In anion doping, the anions are often derived from compounds such as metal fluorides and carbon nitride. These compounds are mixed with oxides and heated to synthesize a target compound. In this case, especially in the case of polycrystalline powdered materials, the resulting sample contains reaction byproducts. Those can interfere with the measurement of intrinsic physical properties. The thin-film synthesis method, however, has the advantage that only the activated anions react with the oxides, and thus the byproducts are less likely to be present in the sample.

The second merit of thin film technique is thin film's high reactivity with anion sources, enabling to obtain mixed anion compounds under mild conditions. A soft chemical process is widely used to dope anion into precursor oxides with maintaining the crystal structure. This technique requires an oxide precursor to be highly reactive with an anion source so that the doping reaction proceeds. Here, I explain the comparison of chemical reactivity between bulk from and thin film form with Figure 1.3.16. When the precursor oxide is prepared in bulk form such as polycrystalline powders or single-crystal pieces, long reaction time and high temperature is needed to diffuse the anion dopant uniformly in the whole sample. In contrast, when the precursor is prepared in thin film form, the anion can rapidly diffuse in the sample owing to the larger surface area/volume

ratio. This high reactivity of thin films makes it possible to lower the reaction temperature and shorten the reaction time than bulk samples, which is preferable to synthesize metastable compounds.
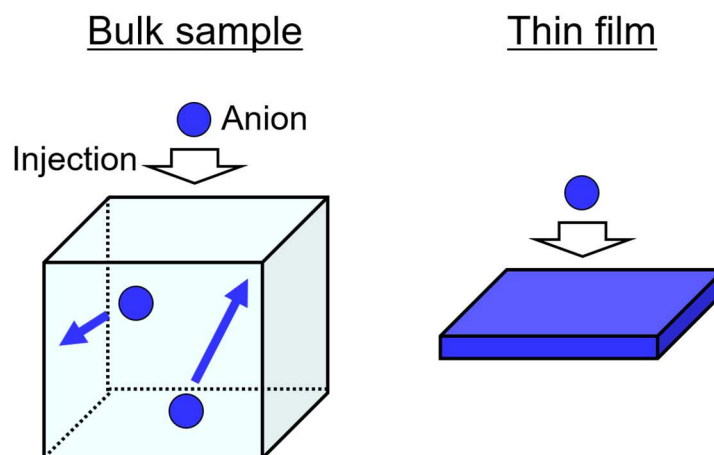
Figure 1.3.15 Comparison of of anion diffusion speeds between
bulk sample and thin film.

In the viewpoint of measurements of physical properties, thin film technique is also advantageous for the following three reasons. Firstly, thin film technique can obtain a single crystal sample that cannot be synthesized through thermal equilibrium processes. In this technique, activated atoms are deposited on a single crystalline substrate, and a crystal is epitaxially grown on it, as shown in Figure 1.3.16(a). Since this is a nonequilibrium process, meta-stable compounds can be stabilized in single crystalline form. A single crystal is suitable to investigate intrinsic transport properties because extrinsic effects such as carrier scattering and charge accumulation at grain boundaries (Figure 1.3.16(b)) can be drastically suppressed. Secondly, a sample with a large area can be gained thanks to a large substrate. Large area samples allow one to conduct various physical measurements, such as electrical measurements, optical measurements, and photoemission spectroscopy. Thirdly, using single crystalline samples can offer

40

information about anisotropic properties, in which the directions of external stimuli such as electric field and magnetic field are well defined. Such information often makes it possible to discuss the detailed mechanism of unusual electronic properties.
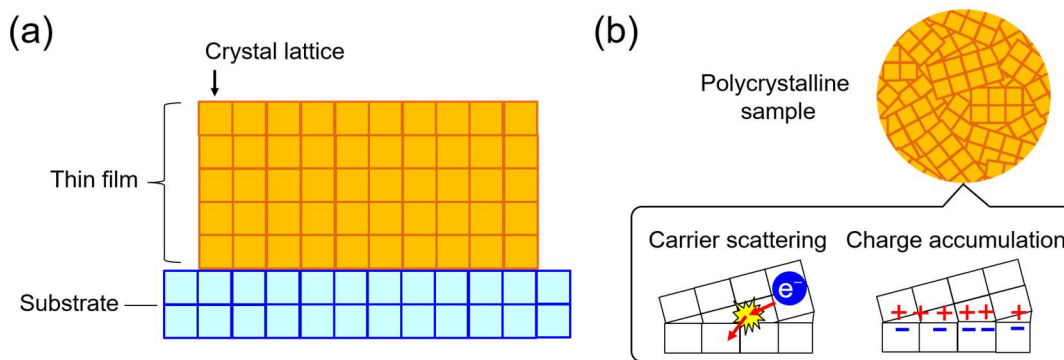
Figure 1.3.16 Schematic illustration of (a) a thin film sample and
(b) two disadvantages of a polycrystalline sample

1.6 Purpose of this study

Figure 1.3.17 is the concept of researches in my doctor course. I have chosen two precursor compounds, $EuNbO_3$ and Sr_2IrO_4, in single-crystalline thin film form and attempted to modify their physical properties. Nb in $EuNbO_3$ has electrons in $4d$ orbitals, exhibiting high electric conductivity, which is unlikely attainable in localized $3d$ orbitals. The $4d$ electrons interact with large spins at Eu, which has the largest spin moment in rare earth elements, resulting in rich physical properties like magnetotransport properties. In order to modulate the interaction, I introduced randomness associated with nitrogen doping. Ir in Sr_2IrO_4 is a typical element with large SOI. Aiming at modulating the physical properties, I also introduced anion randomness by fluorine doping. Therefore, I synthesized nitrogen-doped $EuNbO_3$, and fluorine doped Sr_2IrO_4 thin films and discussed how the physical properties are modulated.
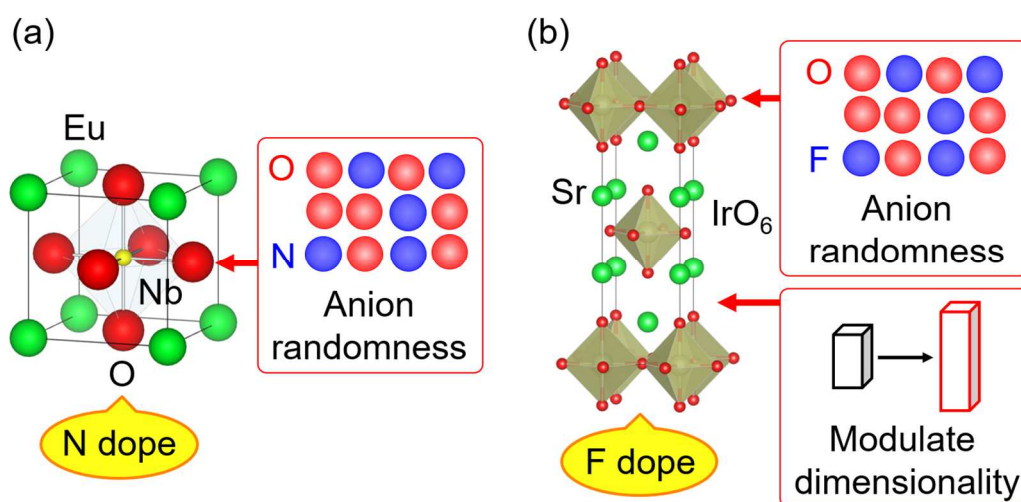
Figure 1.3.17 Concept of my doctoral research.
(a) nitrogen doping into $EuNbO_3$ and (b) fluorine doping into Sr_2IrO_4.

Chapter 2 Experimental techniques

2.1 Thin film fabrication

2.1.1 Pulsed laser deposition (PLD) method

Pulsed laser deposition (PLD) is a physical vapor deposition techniques to fabricate thin films of solid-state materials [88–90]. It is widely used for both fundamental scientific researches and industrial applications. Chemical composition, crystal structure and film quality are governed by various growth parameters conditions such as fabrication temperature, chemical composition of target, laser energy, substrate and so on.

PLD system is schematically illustrated in Figure 2.1.1. Inside an ultra-high vacuum chamber with a base pressure of $<\sim 10^{-9}$ Torr, a pulsed laser beam is irradiated onto a target, which a sintered ceramic pellet or a small piece of metal. Ultraviolet lasers such as KrF laser (248 nm) or Nd: YAG laser (266 nm) are commonly used to achieve efficient absorption of the beam energy by the target. The ablated target is instantly sublimated and becomes a plasmatic state, which is called a plume. The plume vertically heads to a substrate heated at 400 - 1200 °C, and the species forming plume were finally deposited on the substrate.

During the film deposition, a gas such as nitrogen, oxygen, and argon is introduced into the vacuum chamber to tune the deposition rate. As the substrate for fabrication of oxide thin film, a single crystal of oxide compound such as $SrTiO_3$ and $LaAlO_3$ is commonly used. A major advantage of PLD is that the cation ratio of the deposited film is usually the same as that of the target.

Figure 2.1.1 A schematic image of PLD equipment.

2.1.2 Nitrogen-plasma-assisted pulsed laser deposition (NPA-PLD) method

I adopted the nitrogen-plasma-assisted pulsed laser deposition (NPA-PLD) method to dope nitrogen into oxide compounds [91,92]. In this case, a radiofrequency (RF) plasma source is added to the PLD system, as shown in Figure 2.1.2(a). Nitrogen gas is supplied in the form of activated plasma. The activated nitrogen is injected to the plume and reacts with element species, resulting in incorporation with oxide compounds. The nitrogen amount of deposited film is tuned by adjusting the input power of the plasma source and laser frequency. Two graphs in Figure 2.1.2(b) represent the relations between nitrogen amount and the two parameters. When the input power increases, the ejected nitrogen also increases, resulting in high nitrogen concentration in film. Nitrogen amount in a sample also depends critically on the frequency of an excimer laser. When the frequency gets higher, the time for the nitrogen to react with energetically ablated atoms in the plume becomes shorter, resulting in the less amount of nitrogen in film. On the contrary, low frequency makes the reaction time longer and much nitrogen in a sample.

44

The usual method of nitrogen doping is ammonolysis at high temperature. Oxide samples are heated in a tuber furnace under NH_3 flow. NH_3 molecules collides with the sample and is replaced with oxide of a compound at high temperature, resulting in nitrogen-doped products. In this method, the sample tends to have arial inconsistency in nitrogen amount due to non-uniform flow of NH_3 gas. However, because nitrogen is constantly supplied into the plume during film fabrication in NPA-PLD system, nitrogen content tends to be uniform throughout thin film.
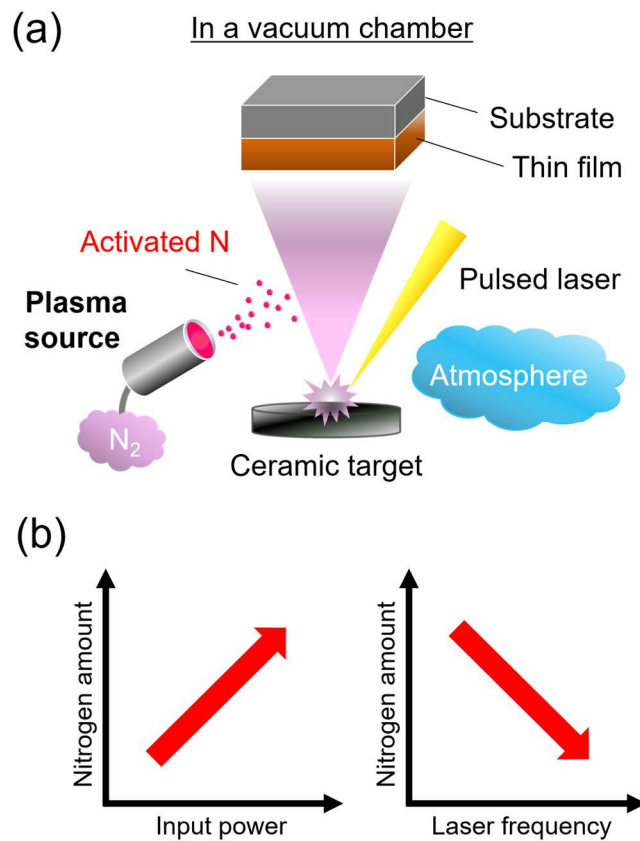
Figure 2.1.2 (a) A schematic image of NPA-PLD equipment. (b) Relations between nitrogen amount in film and two main parameters, the input power and laser frequency.

2.1.3 Topotactic fluorination

Topotactic fluorination is a method to dope fluorine into an oxide precursor compound with maintaining its crystal structure. A frequently used fluorine source is polyvinylidene fluoride (PVDF, monomer unit CH_2CF_2), which is stable in air at room temperature and decomposes above 170°C. An example of a chemical reaction between perovskite ABO$_3$ and PVDF is as follows:

$$ABO_3 + \frac{y}{2}CH_2CF_2 \rightarrow ABO_{3-x}F_y + \left(\frac{3y}{2} - x\right)C + \frac{y}{2}H_2O + \left(x - \frac{y}{2}\right)CO$$
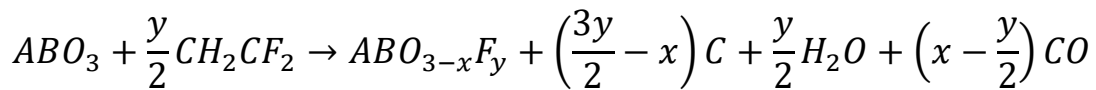
Thus, C, H_2O, and CO are generated as byproducts. The residual on the thin film can be removed by ultrasonic cleaning.

The experimental setup of topotactic fluorination for thin film samples are shown in Figure 2.1.3. A thin film is placed with small pellets of PVDF in a tubular furnace. It is rapped with Al foil to avoid adhesion of PVDF and the reaction residuals, and then heated at 200 - 350 °C with Ar flow for promoting the fluorination reaction.
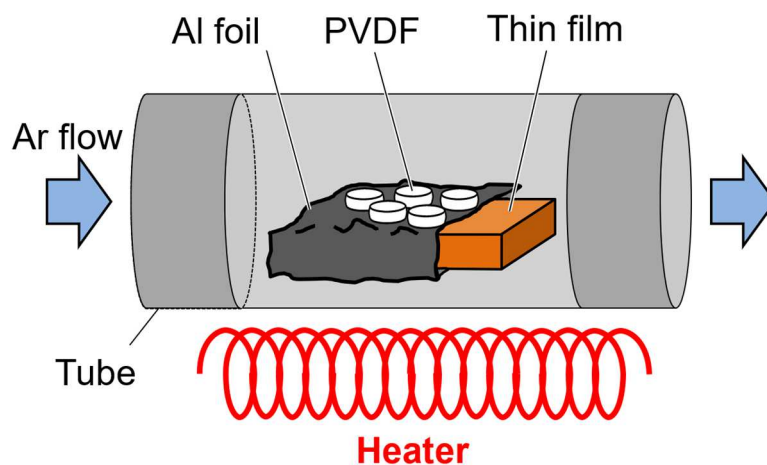
Figure 2.1.3 A schematic image of topotactic fluorination setup.

2.2 Thin film characterization

2.2.1 X-ray diffraction technique

X-ray diffraction technique is a simple and powerful method to analyze the crystal structures of chemical compounds. The principle of the technique is based on the Bragg's law, as is illustrated in Figure 2.2.1. In the figure, X-rays with a wavelength of λ are irradiated to lattice planes at an incident angle of θ. The X-rays reflected by adjacent two planes interference with each other. They are enhanced when the optical path difference is an integral multiple of λ. The condition can be mathematically written as follows:

$$2d \sin\theta = n\lambda$$

where d is the lattice spacing and n is an integer. This equation is called Bragg's law, and diffracted peaks are observed when the geometrical relation satisfies this condition. Therefore, when the values of θ and λ are known, the lattice spacing d can be calculated using this formula.
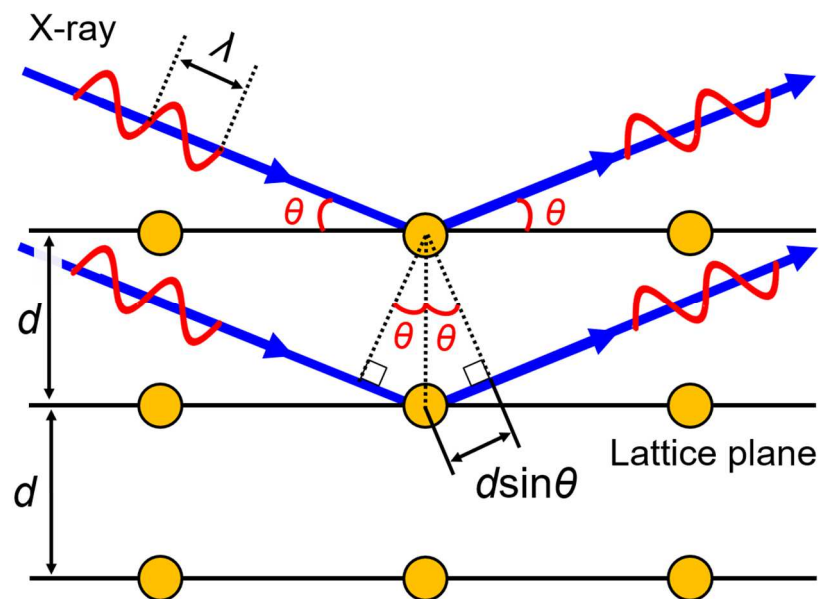
Figure 2.2.1 A schematic image of Bragg's law.

Crystallinity and crystal orientation are evaluated by a four-axis diffractometer, as shown in Figure 2.2.2. The four axis angles 2θ, ω, ϕ, and χ are adjusted to observe diffracted peaks, where 2θ is the angle between the incident and diffracted X-ray beams, ω is the angle between the incident X-ray beam and the sample, and χ and ϕ are the out-of-plane and in-plane tilting angles of the sample, respectively.
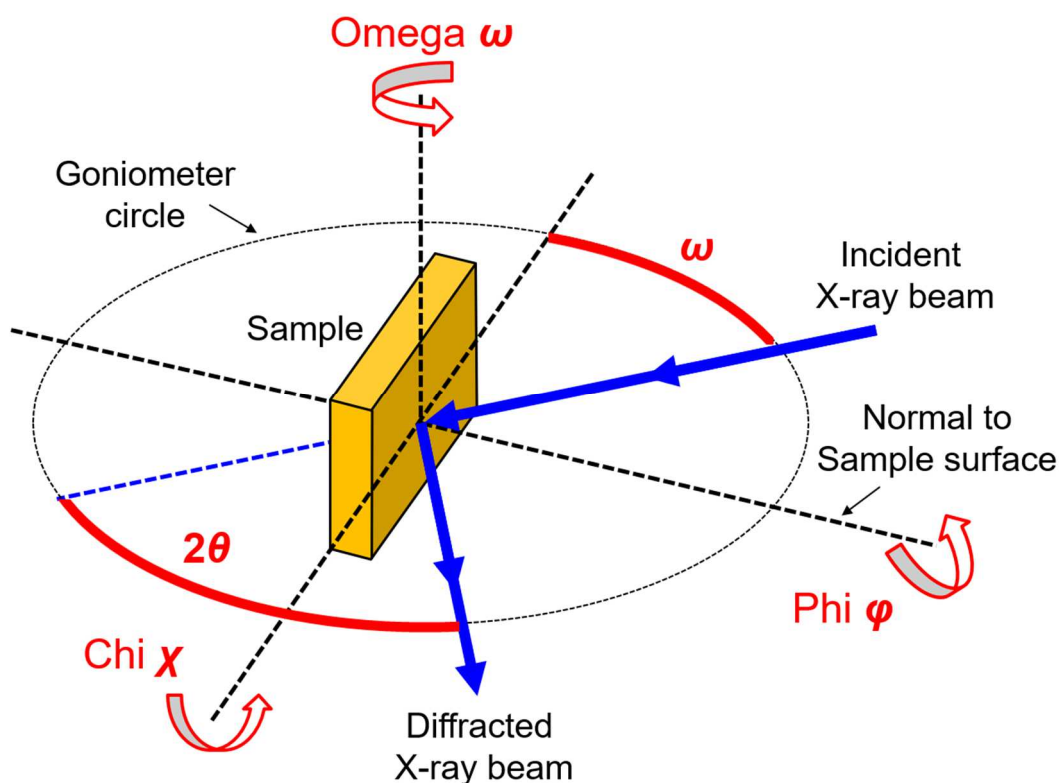
Figure 2.2.2 A schematic image of 4-axis X-ray diffractometer (2θ, ω, ϕ, χ).

I adopted three measurement modes for XRD yielding $2\theta\text{-}\theta$ XRD pattern, $2\theta\text{-}\chi$ XRD image detected by a 2D detector, and reciprocal space mapping (RSM):

$2\theta\text{-}\theta$ XRD pattern is the most common method to determine the lattice constants, as shown in Figure 2.2.3(a). The intensity of the diffraction peak is measured as a function of 2θ angle, where ω is set to be θ, and χ is fixed during measurements. The lattice spacing in the out-of-plane direction is calculated using the Bragg's formula.

The 2θ-χ measurement mode is used to determine the crystalline orientation and the crystallinity of thin films. In this mode, the diffraction intensity from the sample was imaged on a 2D detector by changing 2θ, ω, and χ. If an observed peak spreads along the χ angel, the sample can be regarded as a a polycrystal. On the other hand, if a peak appears in a spot pattern, the diffraction is coherent, guaranteeing the single crystallinity of the sample, as shown in Figure 2.2.3(b).

Reciprocal space mapping (RSM) is a powerful method to visualize the epitaxial relation between thin film and substrate. It detects the diffraction from the sample by changing 2θ and ω. The 2θ-ω patterns are measured at various ω, and all obtained data are converted into a reciprocal space map, which shows the diffraction intensity as a
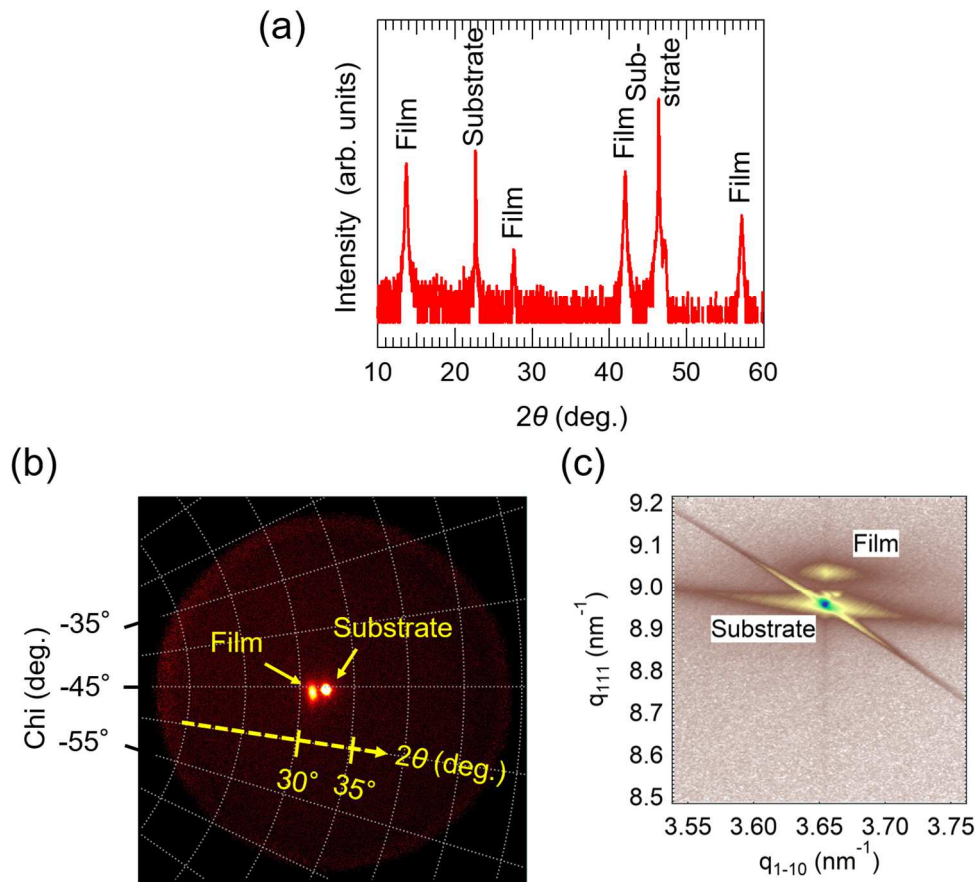
Figure 2.2.3 (a) 2θ-θ XRD pattern. (b) 2θ-χ images detected by 2D detector. (c) RSM image.

function of the reciprocal lattices q_x and q_z. By comparing the q_x values between the film and the substrate, the epitaxial relation between film and substrate can be obtained. Figure 2.2.3(c) shows the situation that the substrate and film have the same q_x values. This indicates that the thin film is grown coherently, and the in-plane lattice of the film is completely locked to that of the substrate.

2.2.2 Atomic force microscopy

Atomic force microscopy (AFM) is a technique for measuring surface roughness in nanoscale by scanning a tiny probe over the sample surface [93]. Simplified setup is shown in Figure 2.2.4. A very sharp tip (AFM scanning tip) is installed on a cantilever. The cantilever works as a very soft spring which can respond to the atomic force between atoms on the sample surface and the tip and bend upward or downward. The subtle motion of cantilever is detected by an optical lever system, where a laser beam reflected at the back of the cantilever is monitored by a photodetector.
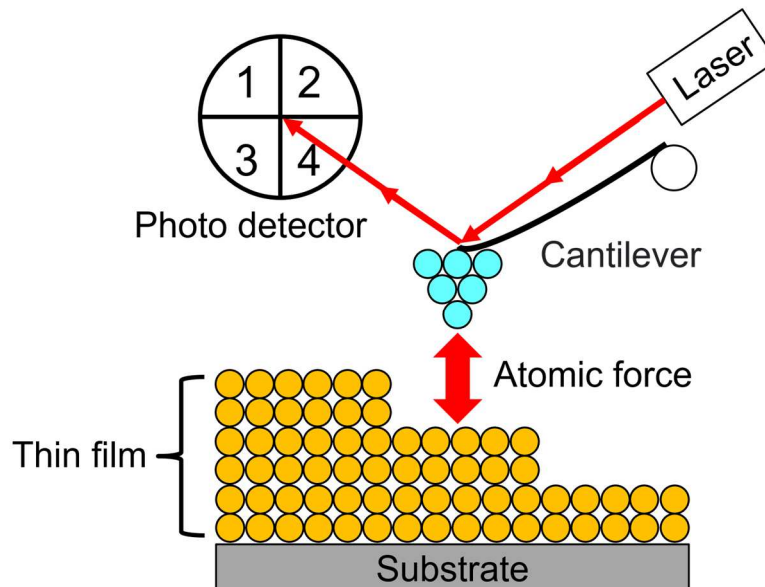
Figure 2.2.4 A schematic image of AFM measurement.

2.2.3 Stylus surface profiler

A stylus surface profiler determines the thicknesses of thin film samples. In the measurements, a tip in contact with a sample surface is moved in lateral directions. By detecting the vertical movement of the tip, the difference in height between the regions with and without the film is evaluated.

2.2.4 Energy-dispersive X-ray spectroscopy

Energy-dispersive X-ray spectroscopy (EDS) is a measurement technique for chemical composition. Figure 2.2.4 is the principle of EDS. When an accelerated electron is injected into an atom, an electron of an inner shell is ejected and a hole is generated at the inner orbital (Figure 2.2.4(a)). Then, an outer shell electron is transferred to the inner shell to occupy the hole with the emission of characteristic X-ray. Detection of the energy and intensity of the characteristic X ray allows elemental identification and semiquantitative analysis.
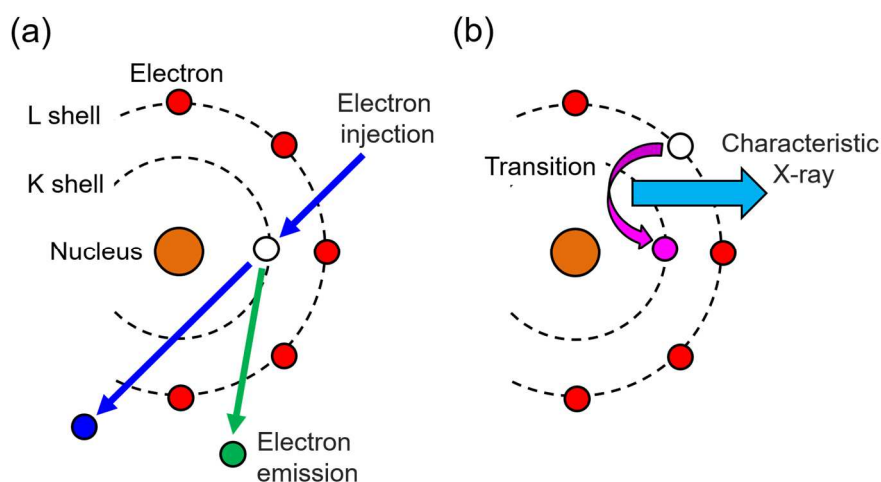
Figure 2.2.5 A schematic mechanism of EDS measurement.
(a) Electron injection and emission. (b) Generation of characteristic X-ray.

2.2.5 Rutherford backscattering spectrometry

Rutherford backscattering spectrometry (RBS) is used to determine chemical composition in samples. Accelerated He^{++} ion is irradiated to a sample, collided with an atomic nucleus in a sample, and is finally backscattered, whose process is schematically illustrated in Figure 2.2.6. The energy of backscattered ion (E_1) is given as follows:

$$E_1 = \left(\frac{M_1 cos\theta + \sqrt{M_0^2 - M_1^2 sin^2\theta}}{M_1 + M_0} \right)^2 E_0$$

where E_0 is the energy of the incident ion, M_0 and M_1 are the masses of the incident ion and collided nucleus, respectively, and θ is the scattering angle. E_0 depends on depth because some He^{++} ions are backscattered at the surface, and other He^{++} ions inside the sample. M_1 is specific to element. Therefore, by detecting the energy and number of the backscattered ions, one can determine constituent elements, their amounts and depth profiles in the sample, as shown in the inset.
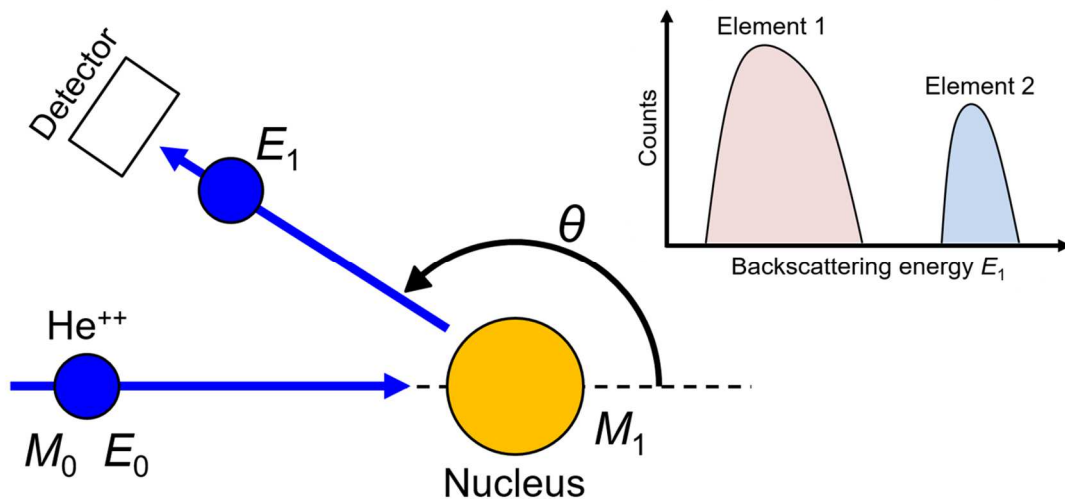
Figure 2.2.6 A schematic image of backscattering of He^{++} in RBS measurement. The inset shows an example of RBS spectra of a sample composed of two elements.

2.2.6 Elastic recoil detection analysis

Elastic recoil detection analysis (ERDA) is used to determine the contents of light elements such as hydrogen, fluorine, and nitrogen. When a Cl^+ ion is accelerated and injected to a sample, it collided with an atom on the sample surface, and the atom is finally emitted from the surface, as shown in Figure 2.2.7. The energy of the emitted atom (recoil atom) E_1 is given as follows:

$$E_1 = \frac{4m_0m_1}{(m_0 + m_1)^2}E_0cos^2\phi$$

where E_1 is the energy of the incident ion, m_0 and m_1 are the masses of the incident ion and recoil atom, respectively, and ϕ is the recoil angle. E_0 depends on the depth at which the collision occurs, and m_1 depends on elements. Therefore, detection of the energy and number of the recoil ions provide information about constituent elements, their amounts and depth profiles in the sample, similar to the case of RBS measurement.
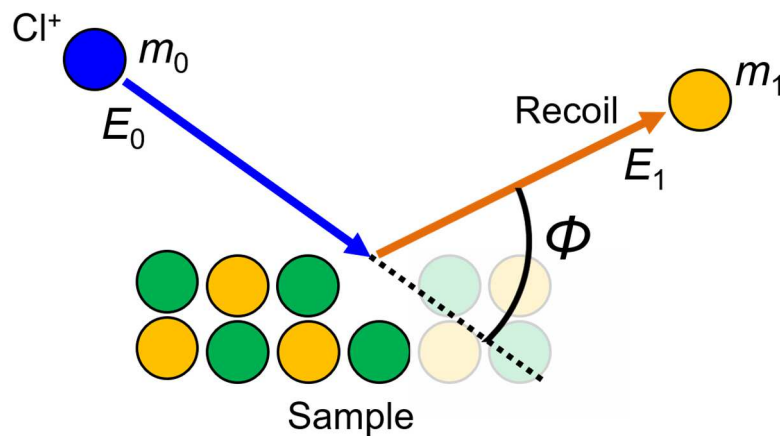
Figure 2.2.7 A illustration of elastic recoil of an atom by Cl^+ injection.

2.2.7 X-ray photoelectron spectroscopy

X-ray photoelectron spectroscopy (XPS) [94] is used to investigate the electronic structure and oxidation state of elements in a sample. When an X-ray beam is irradiated to a sample, an electron is emitted due to the photoelectric effect. After detecting the number and the kinetic energy of the emitted electrons, the XPS spectrum as a function of binding energy is obtained by the following formula:

$$E_B = h\nu - E_K - \phi$$

where E_B is the binding energy of electrons in the sample relative to E_F, $h\nu$ is the irradiated photon energy, E_k is the kinetic energy of photoelectron, and ϕ is the work function. Oxidation states and binding states of each element are determined based on the shape and the peak position of core level XPS spectra.
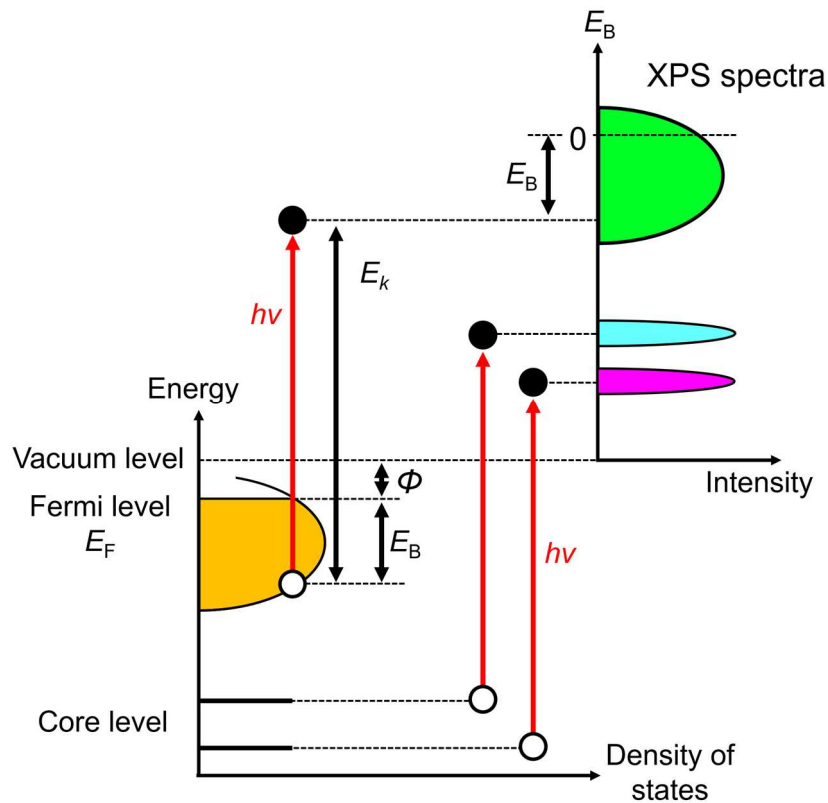
Figure 2.2.8 A schematic image of XPS measurement.

54

2.3 Physical properties measurements

2.3.1 Fourier Transform Infrared Spectroscopy and ultraviolet-visible-near-infrared spectroscopy

Fourier Transform Infrared Spectroscopy (FTIR) and Ultraviolet-visible-near-infrared spectroscopy (UV-VIS) are used to investigate optical properties. The absorption coefficient α of a sample is defined by the transmittance T and the thickness t of the sample , as shown in Figure 2.3.1.

$$I = I_0 \exp(-\alpha t)$$

$$T = \frac{I}{I_0}$$

$$\alpha = -\frac{1}{t} InT$$
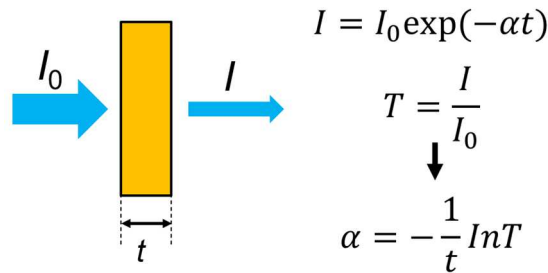
Figure 2.3.1 Definition of Absorption coefficient.

When multiple reflections between the film surface and the film/substrate interface are ignored, the relation among the transmittance of film (T_{film}), transmittance of substrate ($T_{substrate}$) and transmittance of film and substrate ($T_{film+substrate}$) can be calculated from the following equation, as shown in Figure 2.3.2:

$$T_{film+substrate} = \frac{I_{film+substrate}}{I_0} = \frac{I'}{I_0} \frac{I_{film+substrate}}{I'} = T_{film} T_{substrate}$$

$$T_{film+substrate} = \frac{I_{film+substrate}}{I_0}$$

$$T_{film} = \frac{I'}{I_0} \quad T_{substrate} = \frac{I_{film+substrate}}{I'}$$
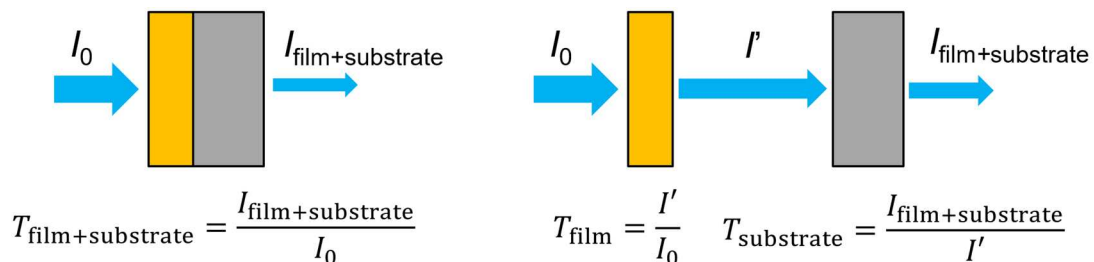
Figure 2.3.2 A schematic image of AFM measurement.

Therefore, the absorption coefficient of thin film on a substrate can be written as follows:

$$\alpha_{\text{film}} = -\frac{1}{t} In(T_{\text{film}}) = -\frac{1}{t} In(\frac{T_{\text{film+substrate}}}{T_{\text{substrate}}})$$

2.3.2 Superconducting quantum interference device

I used a superconducting quantum interference device (SQUID) magnetometer (magnetic properties measurement system (MPMS), Quantum Design Co.) for magnetic characterization. SQUID is a ring of a superconductor such as Nb containing weak links called Josephson junctions. Figure 2.2.11(a) is a schematic image of the SQUID measurement system. When a sample is moved around the edge of a pick-up-coil, an electrical current occurs to cancel the penetrating magnetic field. The current signal is transmitted to the other edge of the pick-up coil, and the magnetic field is amplified there. The change of magnetic field penetrating SQUID is recorded as the change of electric voltage.

The detailed setup of SQUID is illustrated in Figure 2.2.11(b). It is composed of a superconducting ring with two insulating gaps of Josephson junctions. When the magnitude of the magnetic flux penetrating the ring changes, electric current flows through the ring due to the Josephson effect. Detecting the voltage variation enables magnetization measurement with very high sensitivity.
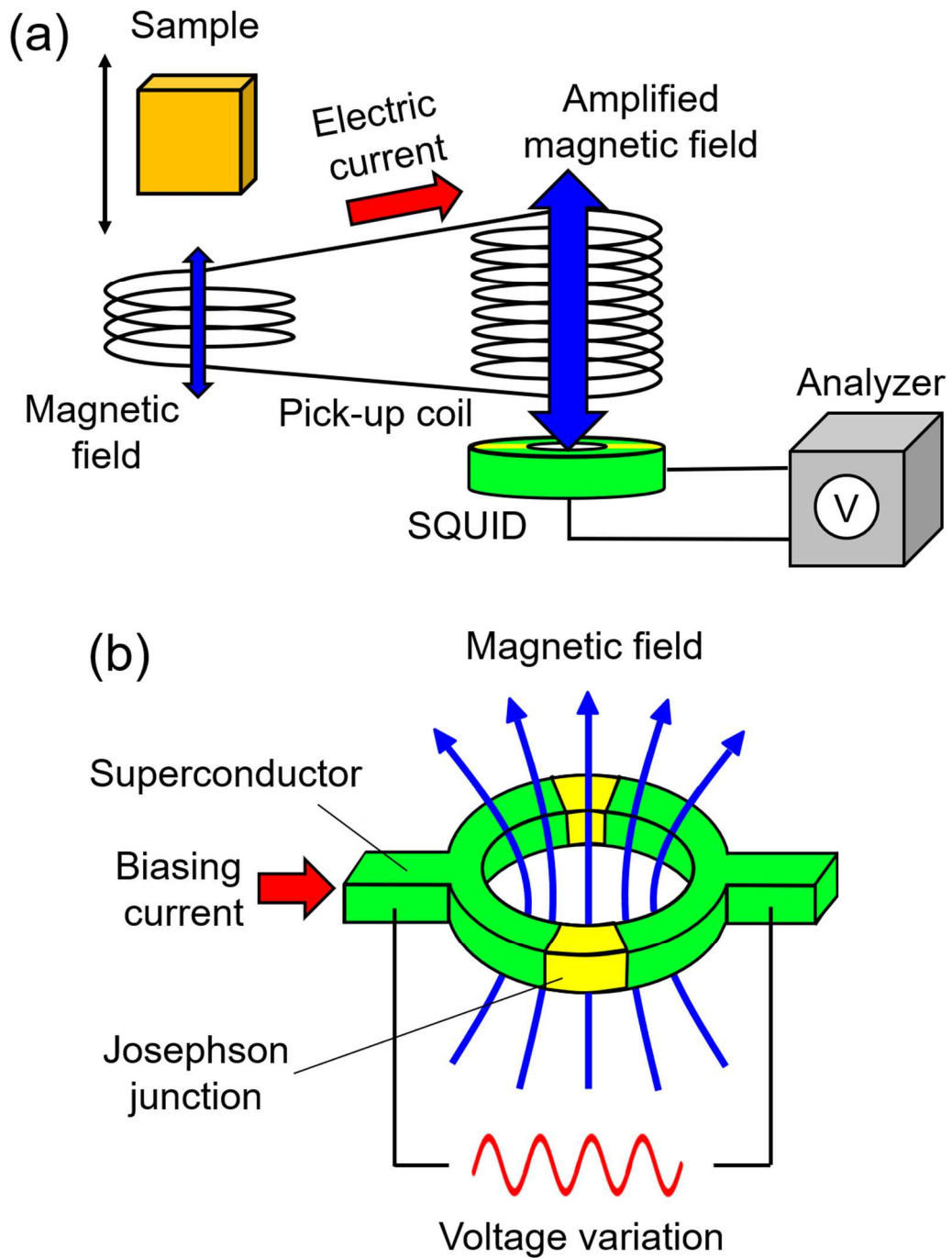
Figure 2.3.3 (a) A schematic image of the whole measurement system.
(b) An illustration of SQUID magnetometer.

2.3.3 Electric transport property measurement

2.3.3.1 Electric resistivity measurement [95]

When an electrical current I flows between two electrodes, voltage V is generated in the current flow direction. Electrical resistivity ρ is obtained by the following formula:

$$\rho = \frac{V}{I} \frac{wt}{L} \, [\Omega \, \text{cm}]$$

where w, t, and L are the current path width, the thickness of the sample, and the length between electrodes for voltage detection, respectively.
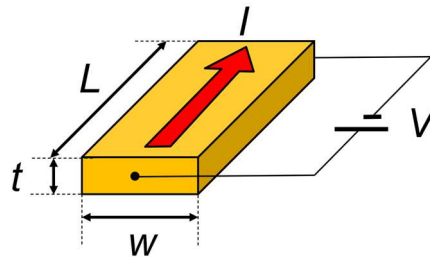
Figure 2.3.4 Definition of resistivity.

Several kinds of measurement geometry are adopted in order to measure I and V. Two-probe and four-probe methods are standard techniques to evaluate the electrical resistivity of samples. The two-probe method, as shown in Figure 2.3.5(a), is used to characterize highly resistive samples, while the four-probe method is used to characterize low-resistance samples. Contrary to the two-probe method with simple setup, the four-probe method is relatively complex because it requires to use Hall-bar-shaped thin films, as shown in Figure 2.3.5(b). Voltage is measured at two different places, V_1 and V_2, to check the uniformity of the sample. V is adopted as the average of V_1 and V_2.

Another technique is the Van der Pawn method [95] [95] [95] [95] [95] [95] [95] [95] [95] [95] [95] [95] [95] [95], which can measure resistivity of thin film samples with arbitrary shapes. In this method, four

58

electrodes are placed at the corners of the sample, and a four-probe measurement is performed with two geometry, as shown in Figure 2.3.5(c). The following equation gives the resistivity ρ:

$$\rho = \frac{\pi t}{\ln(2)} \left(\frac{R_{AB,CD} + R_{BC,DA}}{2} \right) f \left(\frac{R_{AB,CD}}{R_{BC,DA}} \right) \ [\Omega \ \mathrm{cm}]$$

where $R_{AB,CD} = V_{CD} / I_{AB}$, $R_{AD,BC} = V_{BC} / I_{AD}$, t is the thickness of the thin film sample. f is the correction factor that accounts for the effects of non-ideal features of experiments, such as sample shape and positions of electrode, as defined in the following formula.
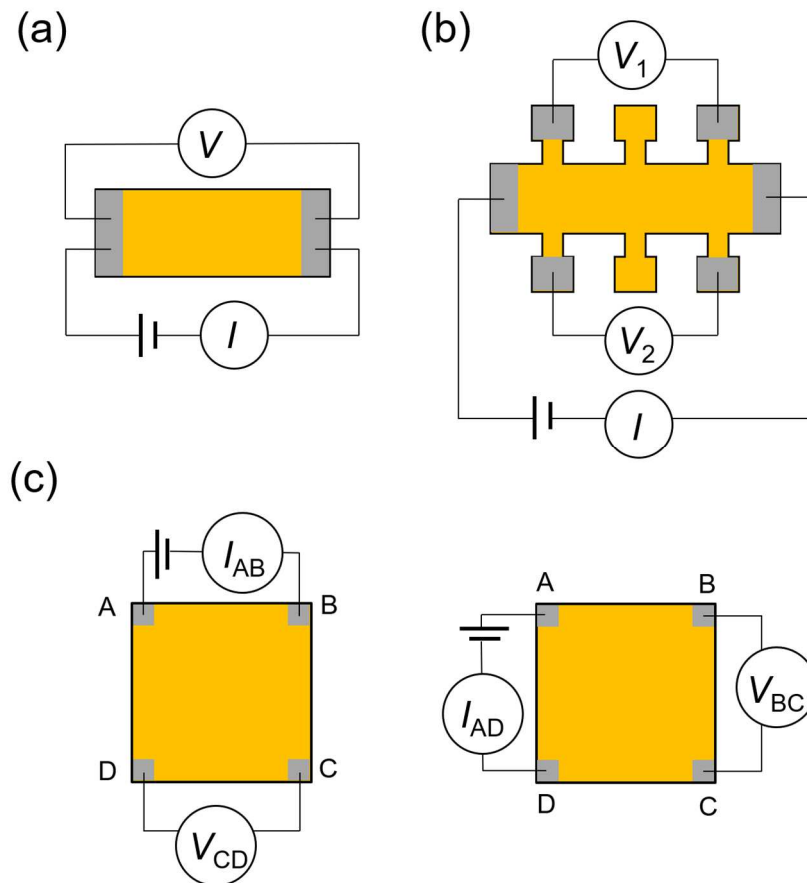
Figure 2.3.5 Schematic illustrations of (a) typical two-probe method. (b) four-probe method in Hall bar geometry. (c) Van der Pawn method.

$$\frac{R_{AB,CD} - R_{BC,DA}}{R_{AB,CD} + R_{BC,DA}} = \frac{f}{\ln(2)} \arccos\left[\frac{\exp(\ln(2/f))}{2}\right]$$

2.3.3.2 Hall effect measurements

Hall effect measurement can five information of carriers such as carrier type, carrier density, and carrier mobility. Figure 2.3.6 shows the situation that electrons carry charges, and the electrical current runs in the positive direction of the *x*-axis. When a magnetic
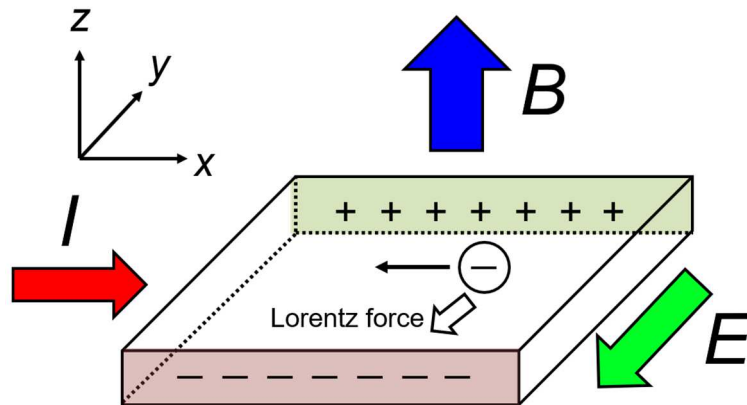
Figure 2.3.6 A schematic image of Hall effect when charge carrier is electron.

field is applied in the positive direction of the *z*-axis, an electric field is generated along the *y*-axis due to the Lorentz force.

The voltage generated along the *y*-axis is called Hall voltage, which is written as the following equation:

$$V_{\mathrm{H}} = \frac{IB}{nqt} = R_{\mathrm{H}} \frac{IB}{t} \ [\mathrm{V}]$$

where *n* and *q* are the carrier density and the charge of carriers, respectively, *t* is the thickness of the sample, and R_{H} is the Hall coefficient. Note that a positive sign of V_{H} means that the electric field is directed along the positive *y*-axis. The carrier type, *n*-type

(negative), or p-type (positive) can be judged from the sign of R_H. Carrier density (n) and carrier mobility (μ) are calculated from the following equations:

$$n = \left| \frac{1}{R_H e} \right| \ [\text{cm}^{-3}]$$

$$\mu = \left| \frac{R_H}{\rho} \right| \ [\text{cm}^2 \text{ V}^{-1} \text{ s}^{-1}]$$

The actual experimental setup of Hall effect measurements in Hall bar geometry is shown in Figure 2.3.7(a). The measurement configuration of the Van der pawn method, is shown in Figure 2.3.7(b), where Hall coefficient R_H can be obtained as follows:

$$R_H = \frac{t R_{\text{BD AC}}}{B} \ \left[\frac{m^3}{C} \right]$$

Where $R_{\text{BD, AC}} = V_{\text{BC}} / I_{\text{AD}}$, and t is the thickness of the thin film.
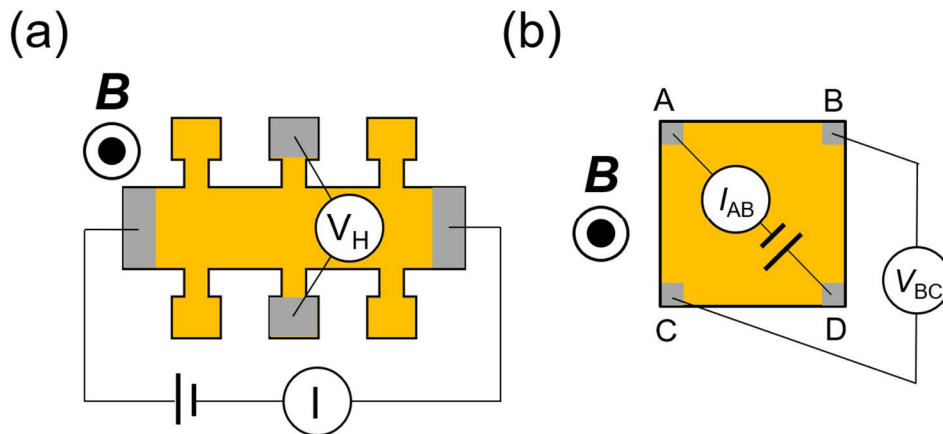
Figure 2.3.7 Figure 2.3.5 Schematic illustrations of Hall effect measurements. Magnetic field is applied in vertical direction for both cases. (a) four-probe method in Hall bar geometry. (c) Van der Pawn method.

3. Magnetotransport properties of perovskite EuNbO₃ thin films[*]

3.1 Introduction

Oxides containing Eu^{2+} ($4f^7$) have attracted considerable attention because of their intriguing physical properties resulting from the large magnetic moment of Eu^{2+} (7 μ_B). For example, rocksalt EuO shows ferromagnetic (FM) semiconducting behavior with a Curie temperature (T_C) of 70 K [96]. T_C increases to 200 K upon the chemical substitution of a trivalent cation such as Gd^{3+} or La^{3+} for Eu^{2+}. This increase in T_C is likely caused by hybridization between the Eu^{2+} 4f and donor states and/or Ruderman–Kittel–Kasuya–Yoshida interaction between the localized Eu^{2+} spin and conduction electrons [97,98]. Another example is perovskite oxides $EuMO_3$, whose crystal structure is shown in Figure 3.1.
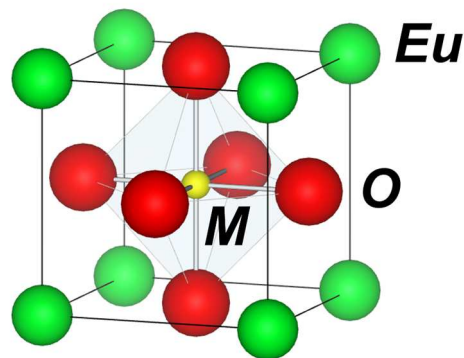
Figure 3.1. Crystal structure of perovskite oxides $EuMO_3$

M in Eu*M*O$_3$ is a tetravalent 3*d*, 4*d* transition metal. They have also been extensively studied in terms of the coupling between Eu^{2+} spin and phonon modes of *M*O$_6$ octahedra or conduction electrons released from *M*. The antiferromagnetic insulators EuTiO$_3$ and EuZrO$_3$ exhibit large magnetodielectric effects at temperatures below the antiferromagnetic (AFM) transition temperature (~5 K) [99,100]. The substitution Nb at 5% of Ti sites in EuTiO$_3$ causes a transition to an FM metallic state [101], and 15% Nb substitution generates a giant low-field magnetocaloric effect [102]. Meanwhile, EuNbO$_3$ shows metallic behavior and FM ordering at temperatures below 4 K [103,104]. Perovskite oxynitride (EuNbO$_2$N), in which the oxygen sites of EuNbO$_3$ are partially substituted by nitrogen, exhibits colossal magnetoresistance (MR) and large magnetocapacitance at low temperature; these properties are attributed to the interplay between the localized Eu^{2+} spin and the off-centered instability of $4d^0$ Nb^{5+}, which is enhanced by covalent bonding to N [85].

The physical properties of Eu^{2+}-based oxide thin films cannot be obtained in bulk samples. Furthermore, the growth of crystals on single-crystalline substrates allows the formation of high-quality crystals suitable for precise measurements with minimal influence from extrinsic factors (e.g., grain boundaries). For example, EuTiO$_3$ thin films undergo a phase transition from a paraelectric AFM phase to a ferroelectric FM phase driven by tensile strain through modification of the spin-phonon coupling [105,106]. In metastable Eu^{2+}Mo^{4+}O$_3$ stabilized by epitaxial strain, a FM metal phase with low resistivity (~31.1 μΩ cm at 2 K) and large magnetic moment (6.8 μ$_B$/Eu at 2 K) appears at temperatures below ~5 K; the metallic conduction and ferromagnetism originate from the Mo $4d^2$ and Eu $4f^7$ electrons, respectively [107].

SrNbO$_3$ thin films, in which the *A*-site ion (Sr^{2+}) has the same ionic radius as Eu^{2+} [108], were recently reported to show interesting phenomena [25,109]. A stoichiometric SrNbO$_3$ thin film showed Fermi-liquid behavior with low resistivity ($\sim 2.8 \times 10^{-5}$ Ω cm) and non-Drude behavior in the near-infrared region [25], and plasmon resonance attributed to the large carrier density was observed in an SrNbO$_{3+\delta}$ thin film [109]. EuNbO$_3$ is also expected to exhibit interesting transport properties under external fields as a result of interactions between the localized spin and itinerant electrons. However, perovskite EuNbO$_3$ has only been obtained in sintered bulk form [103,104,110], and its detailed transport properties have not yet been reported. In this letter, we describe the fabrication of perovskite-structured, single-crystalline EuNbO$_3$ thin films using pulsed laser deposition (PLD) method and the investigation of their magnetic and transport properties. The obtained EuNbO$_3$ thin films exhibited FM behavior with a T_C of ~ 6 K and both positive and negative MR across T_C.

3.2 Experimental methods

EuNbO$_3$ thin films were fabricated on SrTiO$_3$ (001) (STO; cubic structure with $a = 0.3905$ nm; Shinkosha Co.) and GdScO$_3$ (110) (GSO; pseudocubic structure with $a = 0.3967$ nm; CrysTec GmbH) substrates using PLD. Magnetic measurements were conducted using the EuNbO$_3$ thin films deposited on non-magnetic STO substrates. To prevent contributions from conductive SrTiO$_{3-\delta}$ layers at the film/substrate interface in reductive environments, electrical transport measurements were conducted on the EuNbO$_3$ thin films deposited on GSO [111]. The PSD method used a KrF excimer laser (wavelength $\lambda = 248$ nm) with an energy of ~1.3 J/cm^2/shot and a repetition rate of 5 Hz. The PLD target was a polycrystalline EuNbO$_4$ ceramic pellet. To stabilize Eu^{2+}, Ar gas containing 3% H$_2$ was employed as the ambient atmosphere. The gas pressure in the PLD chamber was 1×10^{-4} Torr, and the substrate temperature (T_S) was varied from 300–700°C. The thicknesses of the EuNbO$_3$ thin films were determined to be 40–50 nm using a style profiler (Vecco, Dektak 6M).

The crystalline structures of the films were examined by X-ray diffraction (XRD) with Cu $K\alpha$ radiation (Bruker AXS D8 DISCOVER). The HAXPES spectra of valence band was measured by an electron energy analyzer (VG SCIENTA Scienta R-4000) with an energy resolution of 0.27 eV, at a photon energy of 7.94 keV at beamline BL47XU at the SPring-8 facility Magnetic properties were evaluated using a superconducting quantum interference device magnetometer (Quantum Design MPMS). In-plane electrical transport properties were measured in the temperature range of 2–300 K using the four-probe method with indium electrodes (Physical Property Measurement System, Quantum Design Co.). Hall measurements were carried out using a six-terminal Hall bar

pattern with a width of 1 mm and a length of 3 mm.

3.3 Results and discussion

Figure 3.2(a) shows 2θ–θ XRD patterns (measured at $\chi = 90°$) of the EuNbO$_3$ films fabricated on STO substrates at T_S = 300–700°C. All the films showed the 002 diffraction peaks of perovskite EuNbO$_3$ at 44.2°. No impurity phases were detected in the films fabricated at T_S = 300–600°C, whereas the film prepared at T_S = 700°C contained Eu$_2$O$_3$. As T_S increased from 300–600°C, the 002 diffraction peak became weaker and broader. Thus, we subsequently investigated the intrinsic properties of EuNbO$_3$ based on the films fabricated at T_S = 300 and 400°C. Figure 3.2(b) shows the XRD reciprocal space map of the film fabricated on STO at 400°C; the map was measured around the STO 103 diffraction peak. As shown in the map, the q_x value of the EuNbO$_3$ film (2.45 nm^{-1}) differed from that of the STO substrate (2.56 nm^{-1}). This indicates that the lattice of the EuNbO$_3$ thin film was not perfectly matched to that of the STO substrate. Based on the XRD results, the crystal system of the EuNbO$_3$ film was tetragonal, and the in-plane and out-of-plane lattice constants were calculated to be 0.405 and 0.410 nm, respectively. In a recent study on bulk-sintered EuNbO$_3$, the crystal structure of EuNbO$_3$ was found to be orthorhombic with pseudocubic lattice parameters a_p = 0.4018 nm, b_p = 0.4025 nm, and c_p = 0.4016 nm [110]. In the analogous SrNbO$_3$ structure, the excess oxygen results in the formation of a layered perovskite SrNbO$_{3.5}$ (Sr$_2$Nb$_2$O$_7$) structure with shortened lattice constants and causes a phase transformation from tetragonal to orthorhombic [109]. This might be explained by differences in the amount of oxygen in the samples; the EuNbO$_{3+\delta}$ thin film is thought to have less oxygen than the bulk sample (EuNbO$_{3+\delta'}$; where $\delta < \delta'$).

Figure 3.2(c) shows 2θ–θ XRD patterns (measured at $\chi = 90°$) of EuNbO$_3$ films

fabricated on STO and GSO substrates at 400°C. The 002 diffraction peaks of EuNbO₃ were observed at 44.25° in the samples deposited on both substrates. Based on the XRD reciprocal space map of the film on GSO (data not shown), the lattice constants were calculated to be $a = 0.406$ and $c = 0.409$ nm. These results indicate that the crystal structures of the EuNbO₃ films were equivalent on GSO and STO. Subsequent valuations of physical properties were conducted on films fabricated at $T_S = 400°C$.
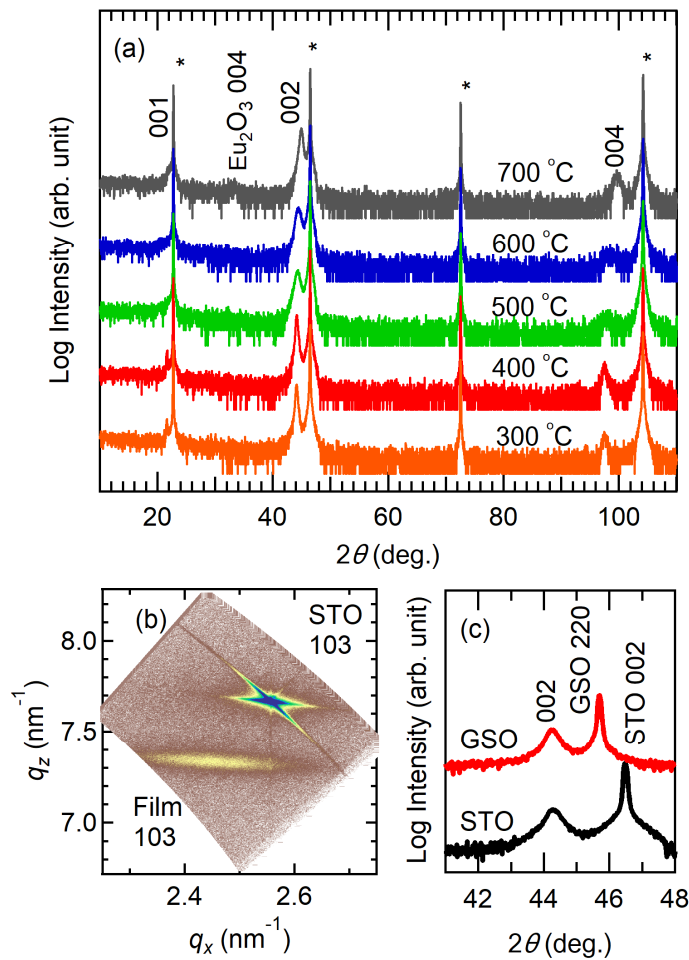
Figure 3.2. (a) 2θ–θ XRD patterns measured at $\chi = 90°$ for the EuNbO₃ thin films deposited on STO at $T_S = 300$–700°C. (b) XRD reciprocal space map of an EuNbO₃ thin film deposited on STO at 400°C (measured around the STO 103 diffraction peak). The white dotted lines are for visual guidance. (c) 2θ–θ XRD patterns measured around the EuNbO₃ 002 peaks at $\chi = 90°$ for the EuNbO₃ films deposited on STO and GSO substrates at 400°C.

Next, we evaluated the magnetic properties of the EuNbO$_3$ thin film. Figure 3.3(a) shows the magnetization–temperature (*M–T*) curve for a EuNbO$_3$ film deposited on STO under an external magnetic field of 0.1 T applied parallel to the in-plane direction. As indicated in Figure 3.3(a), the magnetization of the film decreased with increasing temperature until ~6 K, indicating FM order at $T_C \approx 6$ K. Similar FM behavior has been reported in perovskite oxides containing Eu^{2+} at the *A*-site, including Nb-doped EuTiO$_3$ [101] and EuMoO$_3$ [107].

Figure 3.3(b) shows the in-plane and magnetizations as functions of magnetic field (*H*) at 2 K for EuNbO$_3$ thin film deposited on STO. The saturated magnetization (6.56 μ_B) was close to the theoretical magnetic moment of Eu^{2+} (7 μ_B), demonstrating that most of the Eu ions in the EuNbO$_3$ thin film were in the divalent oxidation state. The slight deviation in saturated magnetization from the ideal value may be due to the presence of a small amount of trivalent Eu ions as a result of surface oxidation. The *M–H* curve indicated an extremely small coercive force at 2 K. Similar magnetic features were also observed in Nb-doped EuTiO$_3$ [101] and EuMoO$_3$ [107].
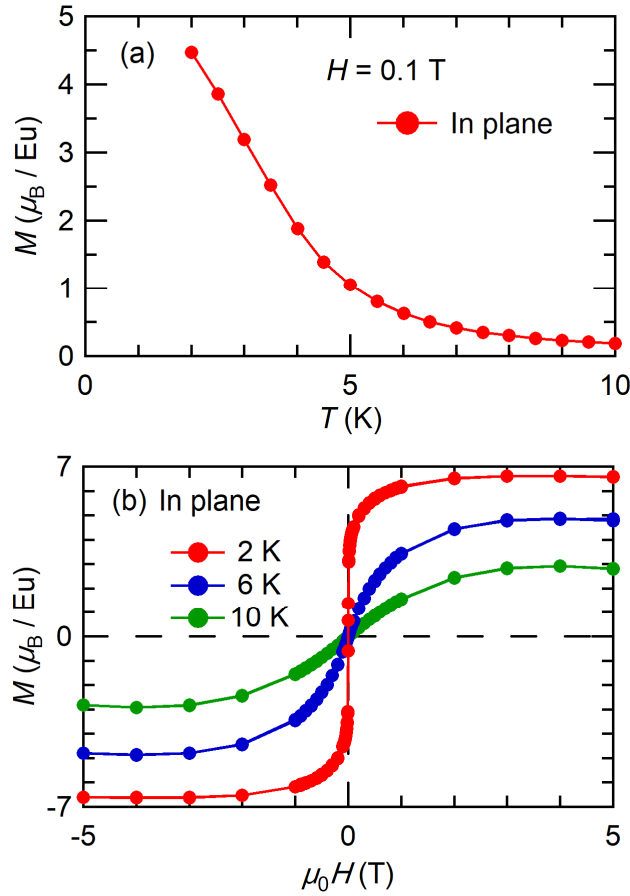
Figure 3.3(a) In-plane *M–T* curves and (b) in-plane *M–H* curves of EuNbO₃ thin film on STO

Figure 3.4 shows the temperature dependence of the transport properties for the EuNbO₃ film deposited on GSO measured under a magnetic field perpendicular to the film surface. As shown in Figure. 3.4(a), the resistivity ρ was almost independent of temperature below 300 K. The ρ value at 300 K (6.5×0^{-4} Ω cm) was one order of magnitude lower than the value previously reported for a bulk-sintered sample (5×10^{-3} Ω cm) [103]; this difference reflects the suppression of grain boundaries. Hall measurements confirmed that the carrier type was electron. The carrier concentration at 300 K [n_e(300 K)] was 9.47×10^{21} cm^{-3}, roughly 60% of the concentration calculated

assuming that each Nb ion supplies one electron (1.56×10^{22} cm^{-3}). The mobility (~1 cm^2 V^{-1} s^{-1}) was nearly independent of temperature, suggesting that impurity scattering governs the carrier conduction [112]. This mobility was approximately one order of magnitude smaller than that of the stoichiometric SrNbO$_3$ thin film on KTaO$_3$ (~15 cm^2 V^{-1} s^{-1}) [25], possibly as a result of the breakup of the NbO$_6$ octahedral conduction network by excess oxygen.
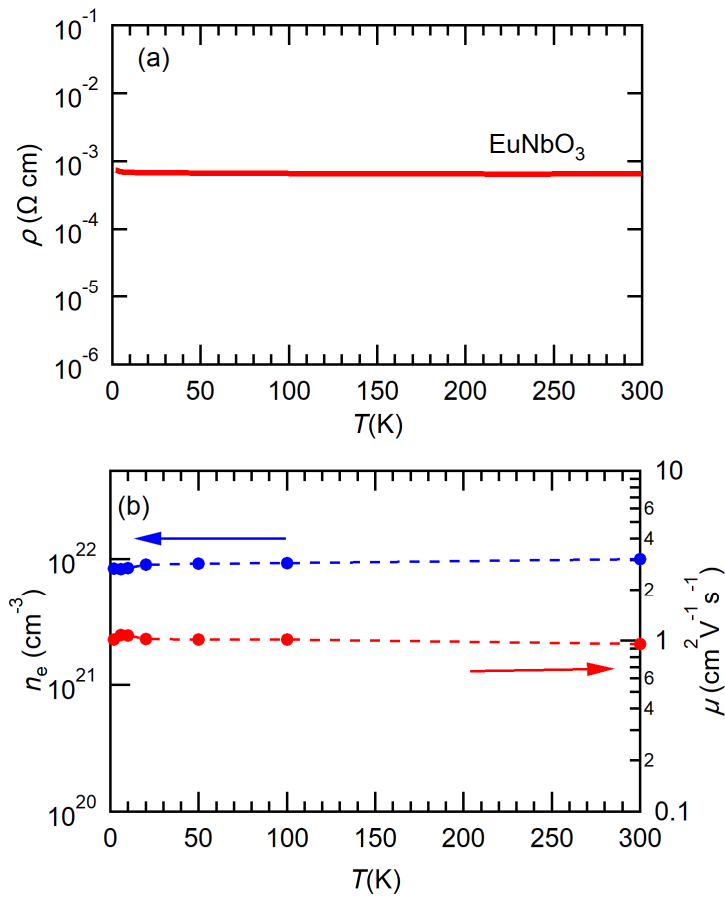
Figure 3.4 (a) ρ, (b) n_e, and μ of the EuNbO$_3$ thin film on GSO substrate as functions of temperatures.

3.3 Results and discussion

To reveal the origin of metallicity, I employed X-ray photoemission spectroscopy (XPS) to measure electronic structure around Fermi level (E_F). Figure 3.4 shows a valence band spectrum of $EuNbO_3$ on GSO. The spectrum mainly consisted of three structures, labeled as *A*, *B*, and *C*. The sharp peak of *A* observed around 2 eV corresponded to the localized Eu^{2+} 4*f* bands, which contribute to the magnetism [107]. The other two broad peaks *B* and *C* were observed at 6 eV and 8 eV, respectively. Based on a density functional calculation [113] and previous research [114], the peak *B* could originate from O 2*p* bonding bands. A strong peak is sometimes observed around 8 eV in the valence spectra of oxides containing Eu^{2+} [115], which is assigned from Eu^{3+} 4*f* bands. Since Eu^{2+} is easily oxidized, an oxidation layer often forms on the surface of a sample. The peak *C* was also attributed to the Eu^{3+} in the surface oxidation layer. The inset shows the magnified view around E_F. There was a finite intensity just above the E_F, consisting with the metallicity. Referring to the first-principle calculation [113], this density of state at E_F was assignable to that of Nb 4*d* bands. Therefore, it can be concluded that the metallicity of $EuNbO_3$ is due to electrons from Nb^{4+}.
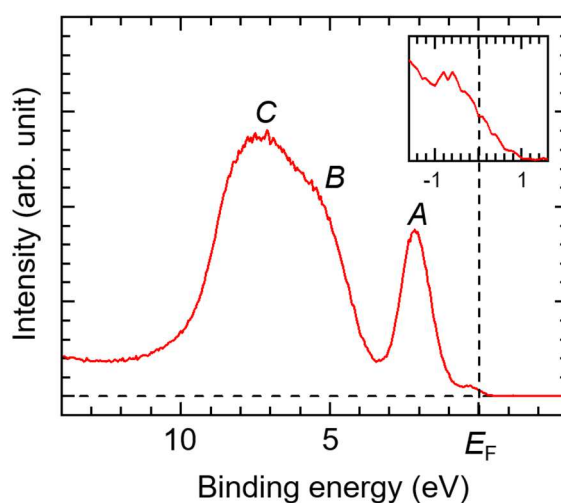
Figure 3.5 Valence band spectra of $EuNbO_3$ thin film on GSO. The inset shows the magnified view around E_F.

71

To investigate the MR of EuNbO$_3$ thin film on GSO, ρ was measured in the presence and absence of a 9-T perpendicular magnetic field, as shown in Figure 3.6(a). A slight increase in ρ was observed at low temperatures under zero field, possibly resulting from enhanced carrier scattering by magnetic domain walls. Positive and negative MR were observed in the temperature ranges of 6–50 K and <6 K, respectively, whereas no MR was observed at temperatures greater than 50 K. Figure 3.5(b) plots the MR ratio, defined as $[\rho(\mu_0 H) - \rho(0)/\rho(0)]$, as a function of H at various temperatures. At 20 K, MR increased with increasing H and became saturated at high magnetic field. At 10 and 6 K, although positive MR was still observed under small magnetic field, the MR ratio gradually decreased with increasing H. Furthermore, the MR vs. H curves at 10 and 6 K showed sharp dips near the low-magnetic-field region, suggesting a weak anti-localization (WAL) effect, a type of quantum interference effect [116]. Quantum interference effects appear when the elastic scattering time is shorter than the inelastic scattering time. The excess oxygen might act as a scattering center, resulting in a short elastic scattering time. Although quantum interference effects usually cause weak localization, the large spin-orbit coupling of the Nb $4d$ orbital may generate WAL in EuNbO$_3$, as reported in YO thin film [117]. In the low-magnetic-field region, the WAL effect is dominant over spin-carrier coupling because the localized spins are not aligned parallel to the magnetic field, as shown in Figure 3.5(b). In contrast, under large magnetic field, the fluctuation of localized Eu spins was suppressed, and the spin scattering between the localized spin and itinerant electrons was reduced, decreasing the MR. At two Kelvin, a negative MR of −5% was clearly observed. The shape of the MR vs. H curve was nearly identical to the shape of the out-of-plane M–H curve [Figure 3.6(c)], which supports the above-mentioned scenario. This result also suggests that spin-carrier coupling is more

important than the WAL effect in the FM region.
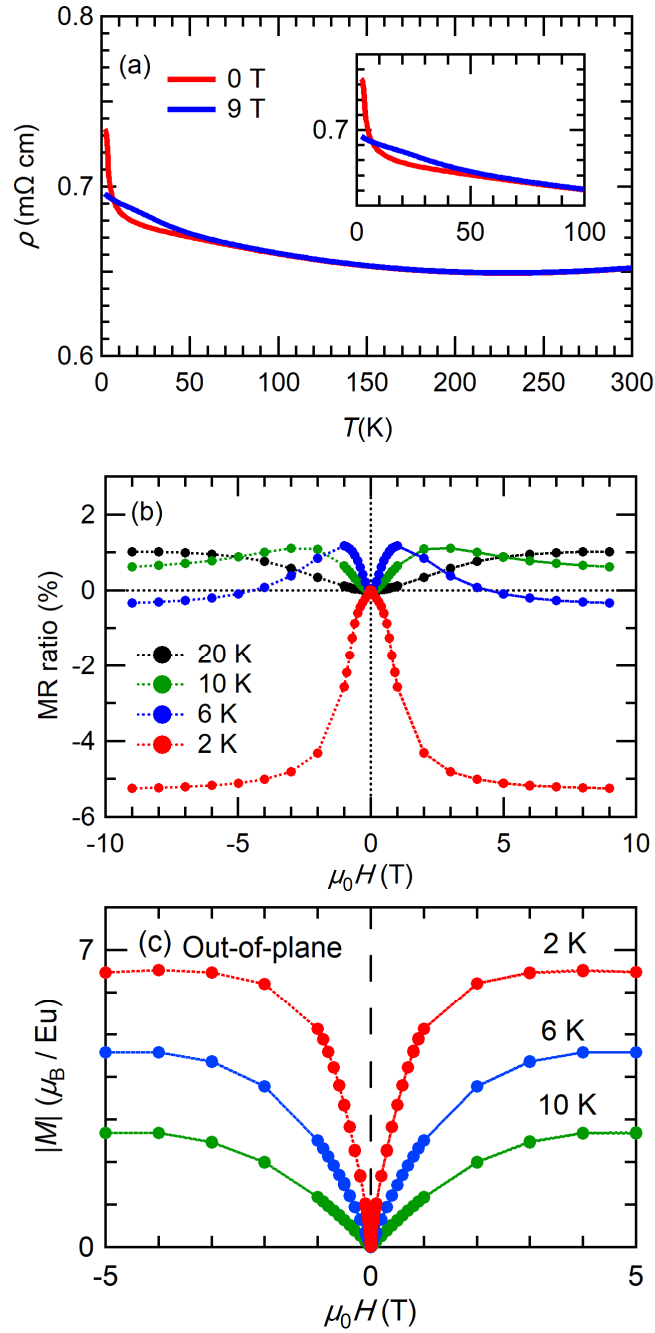
Figure 3.6(a) ρ–T curves measured without a magnetic field [identical to Figure 3.4(a)] and with a 9-T magnetic field of 9 T. (b) Dependence of the MR ratio on magnetic field at 20, 10, 6, and 2 K. (c) Magnetic field dependence of the EuNbO$_3$ thin film on STO.

3.4 Conclusion

I fabricated single-crystal $EuNbO_3$ thin films on STO and GSO substrates using PLD and investigated their magnetic and transport properties. The $EuNbO_3$ films were metallic and exhibited FM behavior with a T_C of ~6 K. Positive and negative MR was observed above and below the T_C, respectively. This suggests that the WAL effect was significant at temperatures above T_C, whereas exchange coupling between Eu^{2+} $4f^7$ localized spins and Nb^{4+} $4d^1$ itinerant electrons was dominant at temperatures below T_C. The results demonstrate that MR can be tuned by adjusting the effects of the above two opposing phenomena in Eu oxides.

4. Nitrogen content dependence of negative magnetoresistance in EuNbO$_{3-x}$N$_x$ thin films

4.1. Introduction

4.2 Experimental methods

4.2 Experimental methods

4.2 Experimental methods

4.3 Results and discussion

4.3 Results and discussion

4.3 Results and discussion

4.3 Results and discussion

4.3 Results and discussion

4.3 Results and discussion

4.3 Results and discussion

4.3 Results and discussion

4.3 Results and discussion

4.3 Results and discussion

4.3 Results and discussion

4.3 Results and discussion

4.3 Results and discussion

4.3 Results and discussion

4.3 Results and discussion

4.3 Results and discussion

4.3 Results and discussion

4.3 Results and discussion

4.3 Results and discussion

5. Influence of fluorination on electronic states and electron transport properties of Sr_2IrO_4 thin films[†]

5.1 Introduction

Layered Ruddlesden–Popper (RP)-type iridium oxides $Sr_{n+1}Ir_nO_{3n+1}$ ($n = 1$ and 2, where n defines the number of Ir–O layers in a unit cell) have insulating ground states, although iridium oxides are mostly metallic [53,54]. The origin of the insulating states in $Sr_{n+1}Ir_nO_{3n+1}$ has been explained by cooperative interplay among a strong crystal field, small on-site Coulomb repulsion (U), and large spin-orbit coupling (SOC) as follows. Owing to the strong SOC, the t_{2g} bands of Sr_2IrO_4 split into two: a lower-energy band with an effective total angular momentum (J_{eff}) of 3/2 and a higher-energy band with $J_{eff} = 1/2$ near the Fermi level [53]. Each Ir^{4+} ($5d^5$) ion provides five $5d$ electrons, four of which fill the $J_{eff} = 3/2$ band and the remaining electron partially fills the $J_{eff} = 1/2$ band. The half-filled $J_{eff} = 1/2$ band is so narrow that a Mott gap opens up even under a small U (-0.5 eV) [53,54]. In addition, spectroscopic and theoretical studies suggested that the insulating nature of $Sr_{n+1}Ir_nO_{3n+1}$ is triggered by antiferromagnetic correlation (Slater type) combined with electron correlation (Mott type) [142]. As the n of $Sr_{n+1}Ir_nO_{3n+1}$

increases, the bandwidth W increases, leading to a decrease in the bandgap. Perovskite $SrIrO_3$ ($n = \infty$) has a semi-metallic nature with a large mass enhancement factor of ~6 [54].

Sr$_2$IrO$_4$ ($n = 1$) is an insulator showing weak ferromagnetism with a Curie temperature of 240 K. The transport properties of bulk Sr$_2$IrO$_4$ are described by the three-dimensional variable-range hopping mechanism, while under epitaxial-strain Efros–Shklovskii-type variable-range hopping, conduction or thermally activated band conduction becomes dominant [143,144]. Coupling between magnetism and transport properties leads to anisotropic magnetoresistance with a magnetoresistance ratio of 80% [145]. In addition, a drastic change in these transport and magnetic properties by carrier doping has been reported. For instance, a robust metallic state can be achieved by electron doping via the substitution of Sr^{2+} by La^{3+} (4%) [146–148]. Moreover, Rh-substituted Sr$_2$IrO$_4$ (Sr$_2$Ir$_{1-x}$Rh$_x$O$_4$) shows a rich electronic phase diagram including antiferromagnetic insulator ($0 \leq x \leq 0.16$), paramagnetic metal/semiconductor ($0.16 \leq x \leq 0.24$), frustrated magnetic insulator ($0.24 \leq x \leq 0.85$), and paramagnetic correlated metal ($x \leq 0.85$) phases [149,150], where substitution with Rh^{3+} ions at the Ir^{4+} sites induces hole doping and magnetic dilution in the system [150].

The electronic properties of $Sr_{n+1}Ir_nO_{3n+1}$ can also be altered by fluorine doping. There are two aims fluorine doping, as illustrated in Figure 5.1. First aim is related to random substitution of oxygen by fluorine in IrO_6 octahedra, as shown in Figure 5.1(a). When oxygen is randomly substituted by fluorine, introduction of anion randomness is expected, which would affect the magnetic interaction and transport properties. Second aim is related to fluorine insertion into SrO rocksalt layers, as shown in Figure 5.1(b). It has been reported that fluorine insertion into vacant space causes the elongation of a unit cell. Therefore, strengthening of two dimensionality rather than three dimensionality is expected.
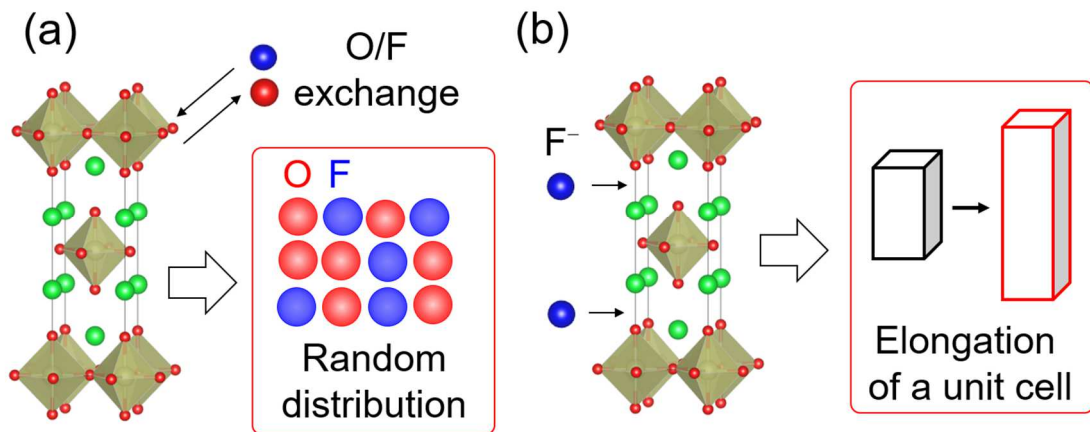
Figure 5.1. Schematic illustration of the aim of fluorine doping into $Sr_{n+1}Ir_nO_{3n+1}$. (a) Substitution of oxygen by fluorine in IrO_6 for introducing anion random distribution. (b) Insertion of fluorine into SrO layers for strengthening two dimensionality.

For instance, a single crystal of $Sr_3Ir_2O_7F_2$ was synthesized from $Sr_3Ir_2O_7$ (n = 2) through a topotactic fluorination reaction using CuF_2 [151]. In $Sr_3Ir_2O_7F_2$, F^- ions were inserted in SrO bilayers, and the oxidation state of Ir changed from Ir^{4+} to Ir^{5+} with fluorination. The fluorination concomitantly changed the electronic ground state from an antiferromagnetic Mott insulator phase with a half-filled J_{eff}

= 1/2 band to a nonmagnetic insulator phase with a $J = 0$ band [151]. Recently, bulk polycrystalline $Sr_2Ir(O,F)_{6-\delta}$ was prepared through topotactic fluorination using ZnF_2, CuF_2, and polyvinylidene fluoride (PVDF) [152], where F^- ions were also inserted into the SrO rock-salt layer. With fluorination, the antiferromagnetic order was suppressed, and paramagnetic behavior was observed, which can be interpreted as the weakening of the antiferromagnetic coupling between IrO_2 layers due to the elongation of the c-axis [152]. The resistivity showed a $T^{-1/2}$ temperature dependence, suggesting Efros–Shklovskii variable-range hopping conduction. However, the observed transport properties might be affected by grain boundaries and reaction products from fluorine sources such as ZnO.

Single-crystalline thin films epitaxially grown on single-crystal substrates are well suited for evaluating intrinsic electric properties. Particularly in the case of oxyfluorides, the topotactic fluorination of epitaxial oxide precursor thin films allows the preparation of such single-crystalline samples with wider ranges of anion compositions [153]. Indeed, topotactic fluorination reactions of thin films with PVDF have been applied to various types of transition-metal–oxide epitaxial thin films, such as $La_{1-x}Sr_xMnO_{3-\delta}$, $SrFeO_{3-\delta}$, $SrCoO_{2.5}$, $(La,Nd)NiO_3$, $BaBiO_3$, and layered Sr_2RuO_4 [74,75,82,153–157].

Herein, I synthesized new layered oxyfluoride $Sr_2IrO_{4-x}F_y$ thin films through the PVDF-mediated topotactic fluorination of Sr_2IrO_4 precursor thin films and investigated their electronic states and electron transport properties. Photoemission spectroscopy (PES) measurements revealed that fluorination did not change the valence state of iridium, Ir^{4+}. Analyses of the crystal structure and chemical composition suggested that the insertion of F^- into SrO rock-salt layers occurred

simultaneously with the partial removal of O^{2-} in the fluorination process. By combining the results of optical and PES measurements, we suggested that the J_{eff} = 3/2 state is stabilized upon fluorination owing to the high electronegativity of fluorine. The temperature dependence of resistivity changed from $T^{-1/4}$ to $T^{-1/2}$ with fluorination, which might reflect the increase of randomness associated with fluorination.

5.2 Experimental methods

Layered perovskite Sr_2IrO_4 precursor films were grown on $SrTiO_3$ (001) (STO, Shinkosha Co.) substrates through the pulsed-laser deposition (PLD) technique by using a KrF excimer laser (wavelength λ = 248 nm) with an energy of 1.5 J/cm^2/shot and a repetition rate of 1 Hz. As the PLD target, we used polycrystalline Sr_2IrO_4 ceramic pellets, which were prepared by mixing powders of Ir metal and $SrCO_3$ through a solid-state reaction (pre-sintering at 900 °C for 20 h and sintering at 1100 °C for 20 h). The substrate temperature and oxygen partial pressure were set to 850 °C and 1×10^{-3} Torr, respectively, during each deposition run. The thickness of the precursor films was set to ~40 nm and was measured using a style profiler (Vecco, Dektak 6M). The obtained Sr_2IrO_4 thin films were further subjected to fluorination using PVDF (Fluorochem Ltd.) under Ar gas flow at 250 °C for 3 h. Following the methodology developed by the group to which I belonged [75,82,153,156,157], the films were covered with an Al foil during fluorination to avoid the adhesion of the charcoal-like residue produced by the decomposition of the PVDF.

5.2 Experimental methods

The crystal structures of the films were evaluated through X-ray diffraction (XRD) with Cu-$K\alpha$ radiation (Bruker AXS D8 DISCOVER). The diffractometer was operated in parallel-beam geometry and was equipped with one-dimensional (1D) and two-dimensional (2D) detectors, which were used to calculate out-of-plane and in-plane lattice constants, respectively. Surface morphology was characterized by atomic force microscopy (AFM, SIISPI4000). Chemical compositions were investigated using an energy-dispersive X-ray spectrometer (EDS, JED-2300, JEOL) used in conjunction with a scanning electron microscope (JSM-7100F, JEOL), which was operated at an electron accelerating voltage of 2.5 keV to reduce any substrate contribution. Photoemission spectra were recorded at 300 K and a vacuum pressure of 10^{-6} Pa by using an R4000 electron energy analyzer (VG SCIENTA) installed at the BL-2A beamline of Photon Factory, KEK. The incident photon energy was 1200 eV. The total energy resolution was set to 300 meV. The Fermi edge of an in situ evaporated gold film was used as the energy reference. In-plane electrical resistivities (ρ) were measured via the two-terminal method with indium electrodes by using a Physical Property Measurement System (Quantum Design Co.). Optical properties were measured at 300 K by using an ultraviolet−visible−near-infrared (UV−Vis−NIR) spectrometer (Jasco V670DS) and a Fourier-transform infrared spectroscope (FT-IR, Jasco FT/IR-4600).

5.3 Results and discussion

Figure 5.2(a) shows a 2θ–θ XRD pattern of the Sr_2IrO_4 precursor thin film on an STO substrate. The figure clearly indicates 004, 006, 0012, and 0016 diffraction peaks originating from a K_2NiF_4-type structure. In the 2θ–χ XRD pattern (Figure 5.2(b)), the 116 diffraction peak of Sr_2IrO_4 was observed at $2\theta = 30.8°$. These results indicate that the precursor film has a tetragonal lattice with $a = 0.557$ nm and $c = 2.573$ nm, which are almost the same as those previously reported for a Sr_2IrO_4 single-crystalline film grown on an STO substrate ($a = 0.549$ nm, $c = 2.580$ nm) [158]. The a-axis parameter of the precursor film was very close to that of the STO substrate ($\sqrt{2}a$STO $= 0.552$ nm), validating the coherent growth of a c-axis-oriented Sr_2IrO_4 single crystalline film.

Figure 5.2(c) shows the 2θ–θ XRD pattern of the film obtained through the fluorination of the Sr_2IrO_4 precursor film with PVDF at 250 °C. All the peaks were indexed to the $004n$ diffraction of the K_2NiF_4-type structure, and no impurity phases, such as SrF_2 and Sr_2IrO_4, were detected. Notably, the $004n$ diffraction peaks were observed at lower angles compared with those of the precursor, indicating the increase of the c-axis length to 3.578 nm. However, the a-axis length of the fluorinated film, as calculated from the 2θ–χ XRD pattern (Figure 5.2(d)), was 0.554 nm, which is almost identical to that of the precursor film (0.552 nm). Thus, it can be concluded that the epitaxial relation between the film and substrate was maintained during the fluorination reaction. Note that the a-axis length of the fluorinated thin film was longer than those of bulk samples [152], which may be due to the tensile strain from the substrate. Furthermore, an expansion of the out-

106

of-plane axis was reported in polycrystalline bulk $Sr_2Ir(O,F)_{6-\delta}$ [152] and has been commonly observed in the topotactic fluorination of layered perovskite oxides. For example, the *c*-axis length of Sr_2RuO_4 thin films increased from 1.270 nm to 1.675 nm upon the insertion of fluoride ions into the SrO rock-salt layers [82]. Therefore, it is suggested that the insertion of fluorine ions also occurred in the Sr_2IrO_4 precursor film. The *c*-axis length of the thin film was also longer than those of bulk samples [152], which implies that the fluorine content of the films is larger than that of the bulk samples.
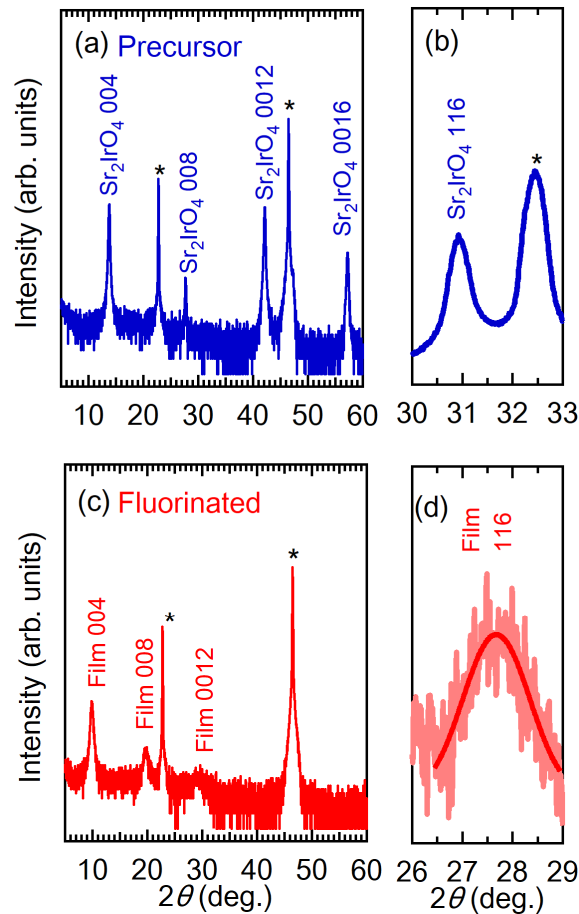
Figure 5.2. X-ray diffraction patterns of the Sr_2IrO_4 precursor film measured at (a) 2θ–θ and (b) 2θ–χ and of the film fluorinated with PVDF at 250 °C measured at (c) 2θ–θ and (d) 2θ–χ on $SrTiO_3$ (001) substrates. (* denotes peaks attributed to the substrate). The solid red line in (d) is the result of Gaussian fitting.

107

Figure 5.3 shows atomic force microscopy (AFM) images of (a) the precursor film and (b) the film fluorinated at 250 °C, which exhibited root-mean-square surface roughness values of 0.35 and 0.81 nm, respectively. This result indicates that the fluorination process did not cause severe surface roughening.
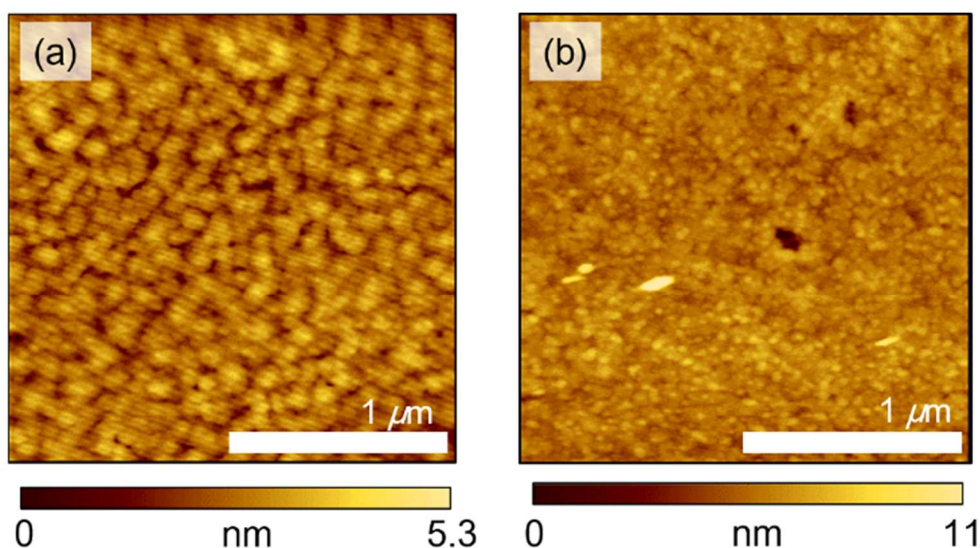
. Figure 5.3. Atomic force microscopy images of (a) the precursor film and (b) the film fluorinated at 250 °C.

In order to examine the chemical composition of the fluorinated film, EDS measurements were performed for O $K\alpha$, F $K\alpha$, and Ir $M\alpha$. Figure 5.4 shows EDS spectra normalized by the peak intensity of Ir $M\alpha$ for the Sr_2IrO_4 precursor film and the film fluorinated at 250 °C. After the fluorination reaction, a clear F $K\alpha$ peak evolved at 0.65 keV, while the intensity of the O $K\alpha$ peak decreased, indicating the incorporation of fluorine into the film and the release of oxygen from the film. Change of anion composition has also been observed during the fluorination of other $n = 1$ RP-type oxides such as $Sr_2RuO_3F_2$, $Sr_2TiO_3F_2$, $La_2NiO_3F_2$, and $Sr_2CuO_2F_2$. [76,82,159,160]. In these fluorination reactions, F$^-$ substitutes for the

O^{2-} sites in BO_6 (B: Ru, Ti, Ni, and Cu) octahedra. Therefore, it is natural that F$^-$ substitution of oxygen in IrO$_6$ octahedra takes place together with insertion into the rock-salt block in the fluorination of Sr$_2$IrO$_4$ By subtracting the substrate contribution from the O $K\alpha$ peak through a Monte Carlo simulation of the electron trajectory in solids [161], the O amount of the Sr$_2$IrO$_x$ precursor film was roughly estimated to be $x \approx 4$. Similarly, the ratio of O to F of the Sr$_2$IrO$_x$F$_y$ film was estimated to be $x : y = 5 : 6$.
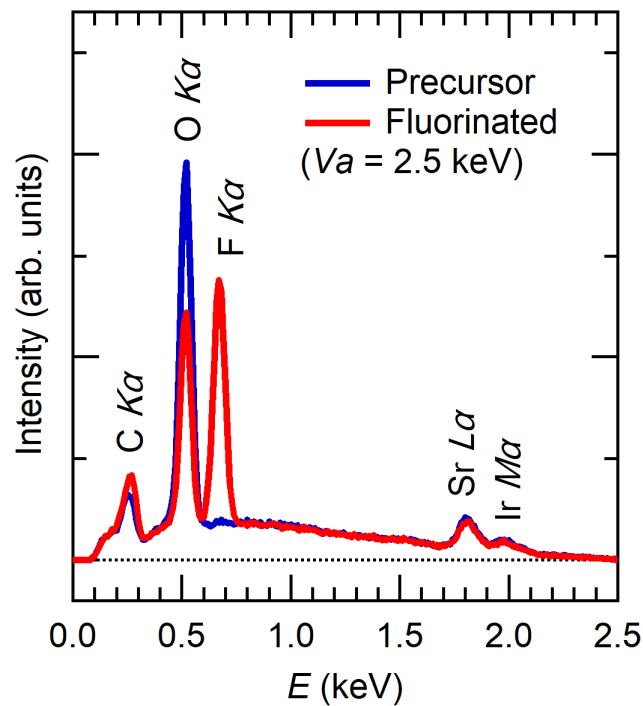
Figure 5.4. Energy-dispersive X-ray spectra of the Sr$_2$IrO$_4$ precursor film and the film fluorinated at 250 °C.

Figure 5.5 shows core-level photoemission spectra of Sr *3d* and Ir *4f* for the precursor and fluorinated films. As shown in Figure 5.4(a), the Sr *3d* peaks of the Sr_2IrO_4 thin film shifted by 1.2 eV towards higher binding energy upon fluorination. Because the Sr *3d* peak position is known to be strongly influenced by the surrounding anions [83], the shift in the Sr *3d* peak is attributable to a change in the chemical environment around Sr upon F insertion. On the other hand, as shown in Figure 5.4(b), the positions of the main Ir $4f_{7/2}$ (~62.0 eV) and Ir $4f_{5/2}$ (~65.0 eV) peaks were not affected by the fluorination. It is well known that in oxide compounds, the Ir $4f_{7/2}$ peak position depends on the valence state of Ir [162–165], and oxides containing Ir^{4+} show the Ir $4f_{7/2}$ peak around 62.0 eV (IrO_2 [162,163]; Sr_2IrO_4 [165]). Therefore, the Ir *4f* XPS spectra in Figure 5.5(b) indicate that the valence state of Ir did not change from 4+ even after fluorination. Note that the Ir *4f* spectra contained two additional peaks at higher binding energies (~63.0 eV and ~65.9 eV), which were also observed in the Sr_2IrO_4 thin-film samples [165]. These additional features are attributed to plasmon satellites, which should be located at higher binding energies, rather than to Ir^{5+} [166–168]. Because the valence state of Ir was found to be 4+, the chemical formula of the fluorinated film can be written as $Sr_2IrO_{4-x}F_{2x}$. Considering the EDS result of $4 - x : 2x = 5 : 6$, the x value can be estimated to be ~1.5 ($Sr_2IrO_{2.5}F_3$). Therefore, during the fluorination of the Sr_2IrO_4 film with PVDF, the insertion of F^- into the SrO block, the introduction of oxygen vacancies in the O^{2-} sites of the IrO_6 octahedra, and F^- substitution at the O^{2-} sites occur simultaneously. The estimated fluorine content per unit cell of the film, ~3, is much larger than that of polycrystalline bulk $Sr_2Ir(O, F)_{6-\delta}$, 1.5 [152], which corresponds to the difference in *c*-axis lengths that was observed. This may be due

to the higher reactivity of thin films, which have larger surface areas and smaller volumes than bulk samples. The modulation of the crystal structure can be summarized as shown in Figure 5.6.
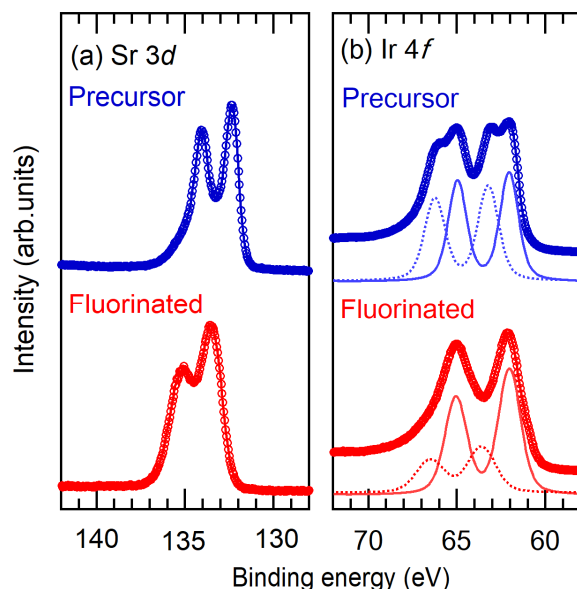
Figure 5.5. Core-level photoemission spectra of (a) Sr *3d* and (b) Ir *4f* for the Sr₂IrO₄ precursor and fluorinated films. These spectra have been normalized to the maximum peak heights. The solid and dashed lines in (b) represent main and satellite peaks, respectively.
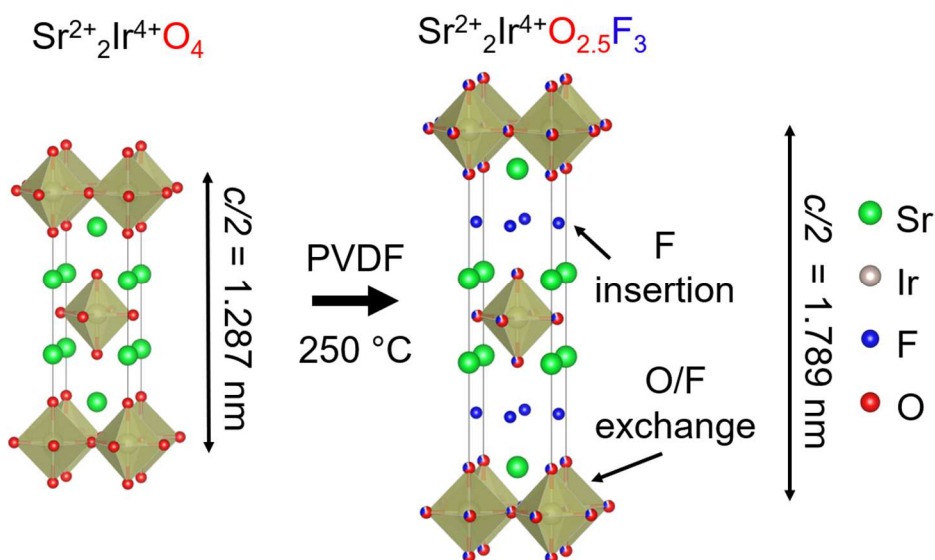
Figure 5.6. Graphical summary of the crystal structure modulation upon fluorine doping into Sr₂IrO₄.

To investigate the electronic structure of the thin films, we conducted optical transmission measurements. From the transmission spectra measured for the film on the SrTiO$_3$ substrate and the SrTiO$_3$ substrate alone, $T(\omega)_{\text{film+substrate}}$ and $T(\omega)_{\text{substrate}}$, respectively, the optical absorption spectrum was calculated as;

$$\alpha\,(\omega) = -\ln[T(\omega)_{\text{film+substrate}}/T(\omega)_{\text{substrate}}]/t$$

,where t is the film thickness. Figure 5.7. compares the $\alpha\,(\omega)$ of the precursor and fluorinated films. Fluorination made the intensity of $\alpha\,(\omega)$ weak, which is consistent with the elongation of the c-axis length. The elongation of the lattice cell result in increase of the film thickness. Since the $\alpha\,(\omega)$ is normalized by length of the optical path in its definition, although the amount of the absorbed light was maintained, the $\alpha\,(\omega)$ was calculated to be a lower value after the fluorination. The spectrum of the precursor film is consistent with that of bulk Sr$_2$IrO$_4$, where peaks *A* and *B* correspond to the transition from the occupied $J_{\text{eff}} = 1/2$ state to the unoccupied $J_{\text{eff}} = 1/2$ state and from the occupied $J_{\text{eff}} = 3/2$ state to the unoccupied $J_{\text{eff}} = 1/2$ state, respectively [53]. After the fluorination, peak *A* shifted to a lower photon energy (peak *A'*) from 0.51 eV to 0.45 eV, while peak *B* shifted to a higher photon energy (peak *B'*) from 1.03 eV to 1.50 eV. The red shift of peak *A* was also observed in the temperature dependence of the optical properties of bulk Sr$_2$IrO$_4$ [169,170], and this phenomenon was well explained by adopting the Fröhlich polaron model on the basis of a large electron–phonon interaction [170]. The in-plane bending modes of the local IrO$_6$ octahedra mainly couple with $J_{\text{eff}} = 1/2$ electrons and holes, whereas $J_{\text{eff}} = 3/2$ holes do not couple with any phonons. Therefore, it is suggested that fluorine insertion/substitution and the concomitant release of oxygen modulate certain phonon modes coupled with $J_{\text{eff}} = 1/2$ electrons.
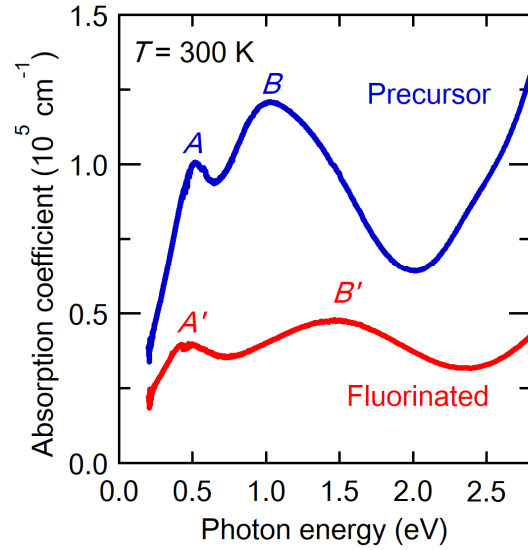
Figure 5.7. Absorption coefficients of the Sr$_2$IrO$_4$ precursor and fluorinated films.

However, the large blue shift of peak *B* (Figure 5.7) cannot be described by the Fröhlich polaron model, because of the absence of interplay between $J_{\text{eff}} = 3/2$ holes and phonons. When oxygen vacancy and fluorine are introduced into the IrO$_6$ octahedra, the ligand field likely departs from cubic symmetry and substantial mixing between the $J_{\text{eff}} = 1/2$ and $J_{\text{eff}} = 3/2$ states occurs, resulting in the large modulation of electronic states. In order to understand the origin of the blue shift of peak B, I measured the valence-band photoemission spectra of the Sr$_2$IrO$_4$ precursor and Sr$_2$IrO$_{4-x}$F$_{2x}$ films (Figure 5.8(a)). The spectrum of the precursor film showed two main peaks at ~1 eV and ~6 eV (peaks *C* and *D*, respectively). To help the understanding of the peaks, I prepared the density of state obtained by the theoretical calculation in the previous report [171], as shown in Figure 5.8(b). The Density of state are separated by four regions labelled A, B, C and D. The A region

corresponds to the Ir $5d$ t_{2g} that hybridize with O $2p$, B to nonbonding O $2p$ orbitals, C and D to both bonding O $2p$ that hybridize with the $5d$ t_{2g} Ir orbitals. According to this analysis, the peak C and D in Figure 5.8(a) are assigned to the Ir $5d$ t_{2g} that hybridize with O $2p$ and bonding O $2p$ that hybridizes with the $5d$ t_{2g} Ir orbitals, respectively. In another reports, the two peaks are denoted as Ir $5d$ -O $2p$ antibonding states and antibonding states, respectively [142]. Notably, the main peaks were shifted towards higher binding energies in the fluorinated film. Because fluorine has a larger electronegativity than oxygen, F $2p$ generally has a larger binding energy than O $2p$. Thus, it is likely that peaks C' and D' are due to the hybridization of F $2p$ and Ir $5d$. Figure 5.9 summarizes the discussion mentioned above. The hybridization of Ir $5d$ with F $2p$ may stabilize the $J_{eff} = 3/2$ states, which increases the energy interval between the $J_{eff} = 3/2$ and $J_{eff} = 1/2$ states and thereby
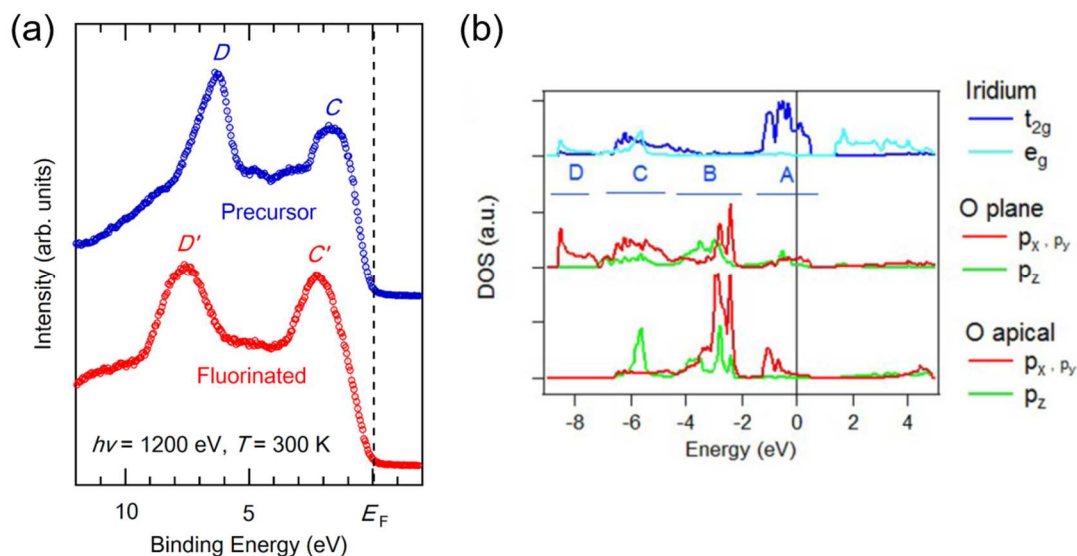
Figure 5.8(a) Valence-band spectra of the precursor and fluorinated films. The dashed line indicates the Fermi level (E_F). (b) Density of states calculated for Sr_2IrO_4, including oxygen octahedra rotations. (b) is reprinted with permission from [171]. Copyright 2019 by the American Physical Society.

results in the blue shift of peak *B*. Although the hybridization of Ir $5d$ with F $2p$ could also stabilize the $J_{\text{eff}} = 1/2$ states, there is no clear evidence in this research.
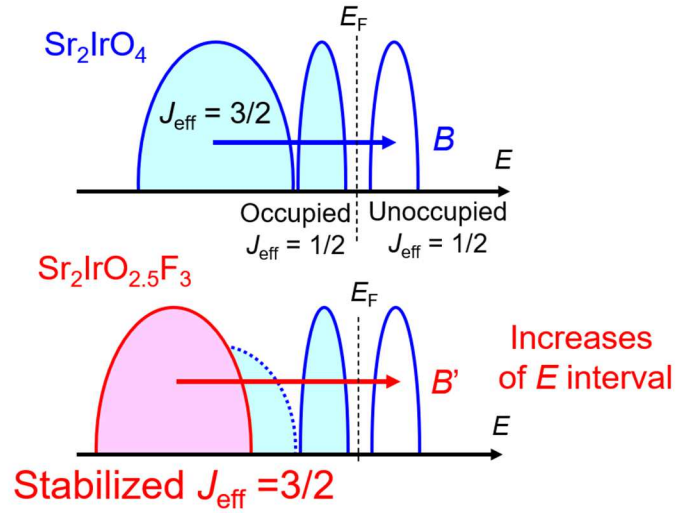
Figure 5.9. Possible modulation of the electronic structure related to the optical transitions.

115

Finally, I investigated how electric conduction was affected by fluorination. Figure 5.10(a) shows resistivity–temperature (ρ–T) curves of the Sr_2IrO_4 precursor and $Sr_2IrO_{4-x}F_{2x}$ films. Both films showed insulating (dρ/dT < 0) behavior with almost the same ρ value at 300 K: ~4.3 × 10^{-1} Ω cm for Sr_2IrO_4 and ~3.2 × 10^{-1} Ω cm for $Sr_2IrO_{4-x}F_{2x}$. This behavior is consistent with the valence-band photoemission spectra, where the density of states was zero at the Fermi level (Figure 5.8). Even though valence state of transition metal was maintained upon fluorination in both $Sr_2IrO_{4-x}F_{2x}$ and $Sr_2RuO_3F_2$ cases, the maintenance of resistivity value in $Sr_2IrO_{4-x}F_{2x}$ films is clearly different from the MIT in $Sr_2RuO_3F_2$ films. The theoretical calculation suggests that the MIT is triggered by change of electric configuration through modification of coordination environment around Ru ions [83]. The analysis of partial density of state of $Sr_2RuO_3F_2$ implies that while the four $4d$ electrons of Ru^{4+} occupy the three t_{2g} bands in Sr_2RuO_4, they occupy the four bands of $(d_{xy})^1(d_{yz}, d_{zx})^2(d_{z2})^1$ in $Sr_2RuO_3F_2$ due to long Ru-F bond. The electric configuration of Sr_2IrO_4 is determined by large SOI, and five electrons
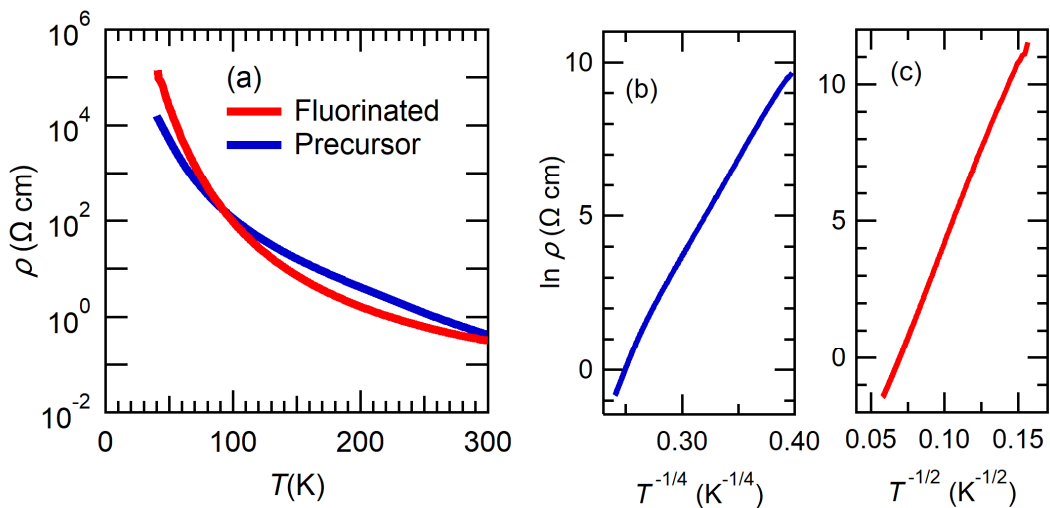
Figure 5.10 (a)Temperature dependence of resistivity of the Sr_2IrO_4 precursor (blue line) and $Sr_2IrO_{4-x}F_{2x}$ films (red line). (b) ln ρ vs. $T^{-1/4}$ and (c) ln ρ vs. $T^{-1/2}$ at T = 40–300 K.

of Ir^{4+} occupy two bands of $(J_{eff}=1/2)^1(J_{eff}=3/2)^4$. The unchanged resistivity value in $Sr_2IrO_{4-x}F_{2x}$ film implies that the electric configuration is not affected by modulation of coordination environment around Ir ions upon fluorination.

Figure 5.10(b) shows a plot of ln ρ vs. $T^{-1/4}$ for the Sr_2IrO_4 precursor film in the temperature range of $T = 40$–300 K. The plot exhibits a good linear relationship with $\rho = \rho_0 \exp (T_0/T)^{-1/4}$, indicating that three-dimensional variable-range hopping is the dominant mechanism of electric conduction. This result is consistent with a previous report [143]. On the other hand, the ln ρ of the $Sr_2IrO_{4-x}F_{2x}$ film was proportional to $T^{-1/2}$ at $T = 40$–300 K, as shown in Figure 5.10(c). This behavior was also observed in the polycrystalline bulk sample [152].

Figure 5.11 shows the possible modulation of the conduction mechanism in Sr_2IrO_4 by fluorine doping. In the Mott variable-range hopping model, the temperature dependence of resistivity varies according to the dimensionality of the conducting pathway [172], and the $T^{-1/2}$ dependence of ln ρ is characteristic of a one-dimensional pathway. However, such one-dimensional variable-range hopping is not plausible for $Sr_2IrO_{4-x}F_{2x}$ with the K_2NiF_4-type structure. Another possibility is Efros–Shklovskii variable-range hopping, which is usually observed when Coulomb interaction plays a key role in carrier hopping [173]. I speculate that Efros–Shklovskii variable-range hopping, rather than Mott variable-range hopping, was dominant because of the following two reasons. The first reason is related to fluorine insertion, which is schematically illustrated in Figure 5.12(a). As fluorine is inserted, electrons are confined in IrO_6 layers, which causes increase of Coulomb interaction. The other reason is related to anion randomness, which is

117

schematically illustrated in Figure 5.12(b). Since conduction mechanism of precursor Sr_2IrO_4 was describe by the Mott variable-range hopping model, hopping electrons in Sr_2IrO_4 may be in a random potential in the crystal. The random distribution of oxygen and electron could additionally create disorder in the conducting pathway of carriers and further enhance carrier localization, which may result in the suppression of the electron screening effect, and thereby the increase of Coulomb interaction between carrier electrons. Therefore, this research demonstrated that the fluorine doping could increase Coulomb interaction.
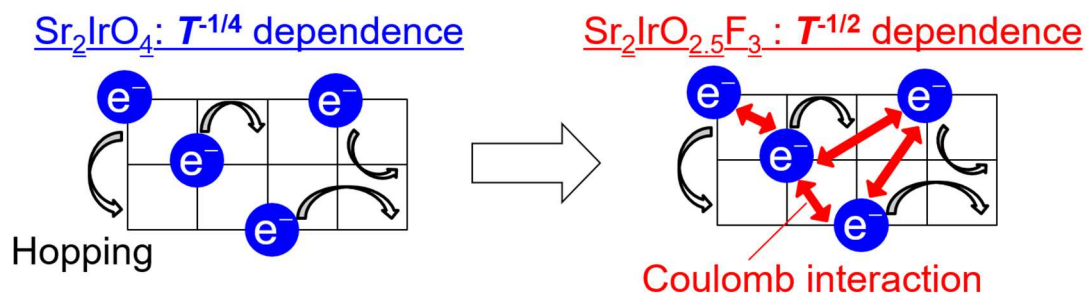
Figure 5.11. Schematic illustration of the modulation of conduction mechanism in Sr₂IrO₄ upon fluorine doping.
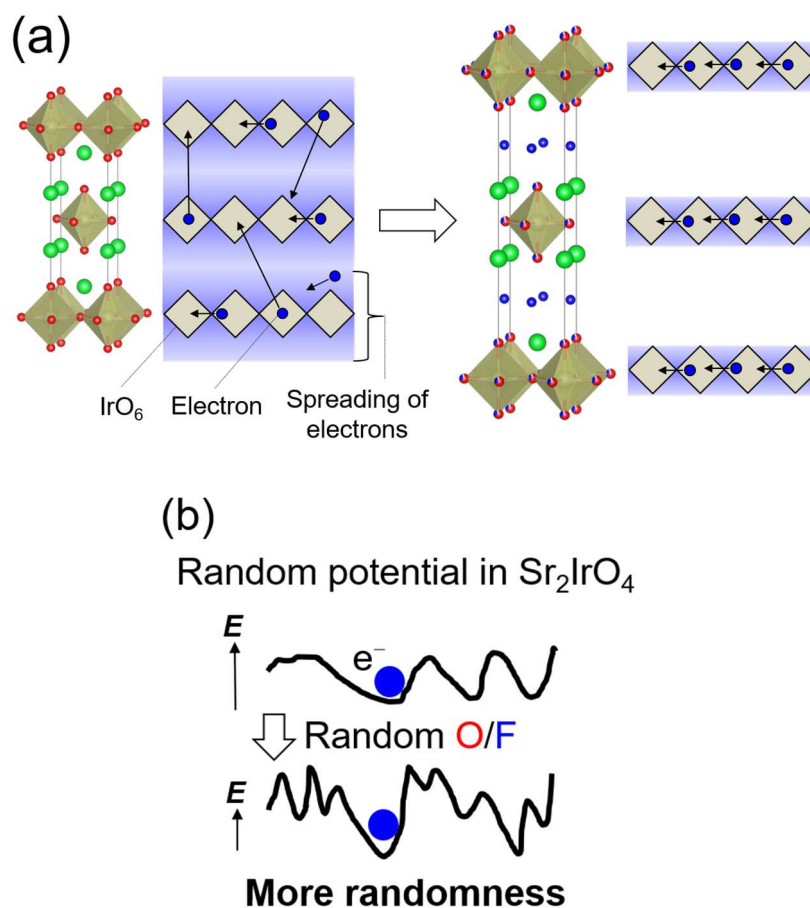
Figure 5.12. Two possible origin of the modulation of conduction mechanism in Sr₂IrO₄ upon fluorine doping. (a) Electron confinement in IrO₆ layers. (b) Enhancement of randomness of the potential in the crystal.

5.4 Conclusion

I synthesized layered oxyfluoride $Sr_2IrO_{4-x}F_{2x}$ thin films using a topotactic fluorination method and observed the modulation of the electric conduction mechanism. In the fluorination process, fluoride ions were inserted into the SrO rock-salt blocks in perovskite Sr_2IrO_4, and oxide ions were partially removed while maintaining the Ir^{4+} valence state. Optical and PES measurements revealed that the $J_{eff} = 3/2$ state was stabilized upon fluorination owing to the large electronegativity of fluorine. The semiconducting behavior was observed in both Sr_2IrO_4 and $Sr_2IrO_{4-x}F_{2x}$ thin films, where $\rho(T)$s of Sr_2IrO_4 and $Sr_2IrO_{4-x}F_{2x}$ were proportional to $T^{-1/4}$ and $T^{-1/2}$, respectively. While the temperature dependence of Sr_2IrO_4 is based on Mott variable range hopping mechanism, that of $Sr_2IrO_{4-x}F_{2x}$ can be explained by the Efros–Shklovskii variable-range hopping mechanism. The change of conduction mechanism could result from the increase of Coulomb interaction among electrons, which may be induced by confinement of electrons in the $Ir(O, F)_6$ layer and by suppression of electron screening effect due to the random potential in $Ir(O, F)_6$. Our research provides valuable insight into how electronic states can be modified by anion doping to explore unprecedented physical properties in RP-type iridates.

In this research, the discussion is largely constructed by speculation. One of the reasons is that there is still limited knowledge about the competition between spin-orbit interaction and crystal field splitting in physical properties. It will be greatly beneficial to theoretically calculate electronic structure of $Sr_2IrO_{4-x}F_{2x}$ and compare with that of $Sr_2RuO_3F_2$. Besides, fluorine doping into Sr_2RhO_4 ($4d^5$) may also be an effective approach.

6. General conclusion

In this research, I attempted to modulate the physical properties of *4d-5d* TMOs thin films by anion doping.

In chapter 3, I examined the magnetic and transport properties of perovskite $EuNbO_3$ by preparing single-crystalline thin films. The $EuNbO_3$ thin films showed metallic transport properties and ferromagnetism with a Curie temperature (T_C) of ~6 K. The sign of magnetoresistance changed around T_C, possibly due to competition between the weak anti-localization effect and magnetic coupling between Eu^{2+} $4f$ localized spins and Nb^{4+} $4d$ itinerant electrons.

In chapter 4, I investigated magneto-transport properties of $EuNbO_{3-x}N_x$ single-crystalline thin films with different nitrogen contents (N/Eu = 0.6, 0.7, 1.0). It was found that nitrogen doping induced the change of transport properties from metallic to semiconducting behavior with gradual increase of electric resistivity. The semiconducting behavior could be described by three-dimensional variable-range hopping conduction, suggesting that carrier localization occurred due to the random distribution of nitrogen in the anion sites. The negative MR ratio at 2 K increased from 20 % to 98 % with an increase of N^{3-} amount. It was proposed that the exchange interaction between Eu^{2+} and Nb $4d^1$ localized spins in the random potential played a key role in the colossal negative MR of ENON.

In chapter 5, I fabricated layered-perovskite $Sr_2IrO_{4-x}F_{2x}$ thin films by combining pulsed-laser deposition with topotactic fluorination and investigated their structures, electronic states, and electron transport properties. Semiconducting behavior was

observed in both Sr_2IrO_4 and $Sr_2IrO_{4-x}F_{2x}$ thin films, where $\rho(T)$s of Sr_2IrO_4 and $Sr_2IrO_{4-x}F_{2x}$ were proportional to $T^{-1/4}$ and $T^{-1/2}$, respectively. While the temperature dependence of Sr_2IrO_4 was based on Mott variable range hopping mechanism, that of $Sr_2IrO_{4-x}F_{2x}$ can be explained by the Efros–Shklovskii variable-range hopping mechanism. The change of conduction mechanism could result from the increase of Coulomb interaction between electrons, which may be induced by confinement of electrons in the $Ir(O, F)_6$ layer and by suppression of electron screening effect due to the random potential in $Ir(O, F)_6$.

In conclusion, I successfully modulated the physical properties of $4d$-$5d$ TMO thin films by anion doping and provided valuable insights into the intrinsic role of the anions. In the study of $EuNbO_{3-x}N_x$, I proposed a model that randomly distributed nitrogen localizes Nb $4d^1$ electrons, and that the exchange interaction between Eu^{2+} and Nb $4d^1$ localized spin is responsible for the colossal negative MR effect. In the study of $Sr_2IrO_{4-x}F_{2x}$, it was found that F doping could increase the Coulomb interaction among electrons by strengthening two-dimensionality and by introducing random distribution of oxygen and nitrogen. Introduction of randomness associated with anion doping in $4d$-$5d$ TMOs would lead to a finding of unprecedented physical properties in $4d$-$5d$ TMOs. Based on this idea, I also examined the transport properties of $SrWO_{3-x}N_x$ single-crystalline thin films and found positive magnetoresistance which cannot be explained by the conventional classical theory (Appendix.A). A further deep and systematic understanding of the roles of the anions in the electronic properties of $4d$-$5d$ TMOs will enrich the field of mixed anion compounds based on $4d$-$5d$ transition metal elements.

Appendix Chapter A: Transport properties of SrWO$_{3-x}$N$_x$ thin films

A.2 Experimental methods

A.2 Experimental methods

125

A.3 Results and discussion

A.3 Results and discussion

A.3 Results and discussion

A.3 Results and discussion

,

A.3 Results and discussion

A.3 Results and discussion

A.3 Results and discussion

A.3 Results and discussion

A.3 Results and discussion

A.3 Results and discussion

A.3 Results and discussion

A.3 Results and discussion

A.3 Results and discussion

A.4 Conclusion

Appendix Chapter B: Calculation of the magnetization of Eu oxide/oxynitride thin films

B.1 Introduction

Oxides containing divalent europium are famous for its large magnetization. The electric configuration of Eu^{2+} is $4f^7$. The magnetic moment μ of an ion is proportional to the total angular momentum J ($J = L+S$) of several electrons, which is expressed as the following formula:

$$\mu = - g\mu_B J$$

,where g is called the g factor. The magnetization M created by N magnetic moments per unit volume is represented by using the famous Brillouin function as follows:

$$M = Ng\mu_B J B_J(x) \ (x = \frac{gJ\mu_B B}{k_B T})$$

Here, I theoretically calculate the saturated magnetization M_s of a compound with one Eu^{2+} in a unit cell. Seven electrons of Eu^{2+} occupy seven orbitals one by one, resulting in the $L = 0$, $S = 7/2$ and $J = 7/2$. In that situation, the g facture is 2. In a large magnetic field near 0 K, x divers to infinity and $B_J(x)$ converges to 1. Therefore, M_s of the compound becomes as follows:

$$M_s = 1 \times 2 \times \mu_B \times \frac{7}{2} = 7 \mu_B$$

The M_s of perovskite oxide $EuMO_3$ (M = transition metal ions) has been experimentally measured in past research. The saturated magnetization of $EuTiO_3$ always lies in between

140

6-7 μ_B /f.u., which is close to the theoretical value of 7 μ_B [101,105,177]. The deviation

between experimental values and the theoretical values is thought to originate from some

oxidized region in prepared sample containing Eu^{3+} without spin moments. I also refer to

the contribution of itinerant electrons to the magnetization. According to previous reports,

$SrNbO_3$ is paramagnetic and its magnetization is negligibly small (below 0.001 μ_B/f.u.)

compared to the contribution of Eu^{2+} [178]. The negligible contribution of iterant

electrons to the saturated magnetization is also confirmed in $EuMoO_3$ [107]. The

saturated magnetization at 2 K of $EuMoO_3$ was 6.8 μ_B /f.u., which is almost same as the

theoretical value. Therefore, the effect of itinerant electrons can be neglected and M_s of

Eu*M*O$_3$ is mainly due to only magnetic moments of Eu^{2+}. In the following section, I

simply explain the procedure of calculation of magnetization of $EuNbO_3$ and EuNbO$_{3-}$

$_x$N$_x$ thin films.

B.2 Calculation procedures

Oxides containing divalent europium are famous for its large magnetization. In

this chapter, I briefly explain procedures of calculation of the magnetization of $EuNbO_3$

and EuNbO$_{3-x}$N$_x$ thin films. Figure B.1(a) is an original data of the magnetization of

$EuNbO_3$ thin film on STO by MPMS. The data was in emu units together with

contribution from the diamagnetism of the substrate.

After subtracting the diamagnetic contribution, a clear *M-H* cure appeared as shown

in Figure B.1(b). To transform the unit from emu to Bhor magnetization (μ_B), I used a

following correspondence:

$$1\ emu \approx 1.078\ \times 10^{20}\ \mu_B$$

Besides, to calculate the magnetization per one Eu atom, I estimated the number of a unit cell

B.2 Calculation procedures

in the thin film sample, by diving the sample volume by the cell volume. Table B.1 summarizes the magnetization value of EuNbO$_3$ film at 2 K under a magnetic field of 5 T. First of all, the M value was 4.02×10^{-4} emu, which was seen Figure B.2. The value was calculated in Bhor magnetization unit, resulting in 4.33×10^{16} μ_B. Estimation of the number of a unit cell in the sample was based on division of the sample volume by the cell volume, where the sample volume was calculated from multiplication of film surface area and film thickness. In this case, there were 6.60×10^{15} cells in the sample. Finally, the magnetization per one Eu atom was obtained in Bhor magnetization unit by dividing 4.33×10^{16} μ_B by 6.60×10^{15}. When this procedure was applied to all data, Figure B.1(c) is finally obtained.
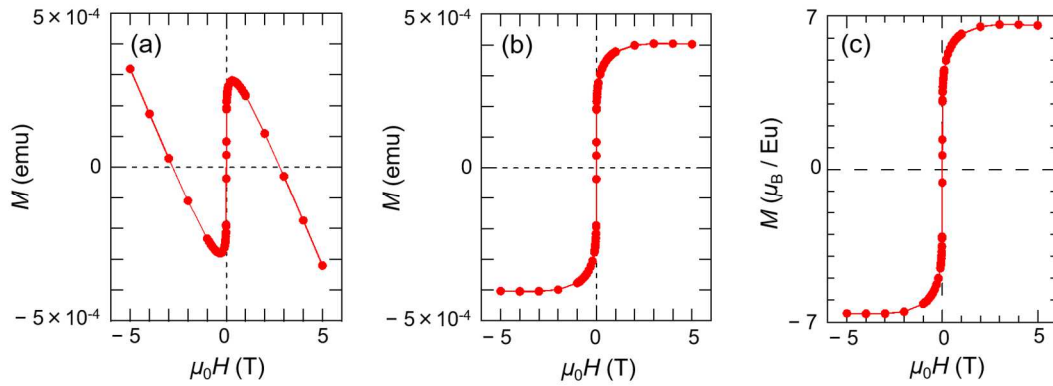
Figure B.1 Three kinds of *M-H* curves of EuNbO$_3$ /STO (a) the original date (b) the data after subtracting the contribution of the substrate. (c) the data after transforming the units.

2 K, 5 T	Value
M [emu]	4.02×10^{-4}
M [μ_B]	4.33×10^{16}
Cell number in the sample	6.60×10^{15}
M [μ_B / Eu]	6.56

Table B.1 Summary of magnetization value and the EuNbO$_3$ cell number in the thin film sample.

I analyzed the magnetization of $EuNbO_{3-x}N_x$ thin film in the same manner. Figure B.2. and Table B.2 are counterparts of Figure B.1 and Table B.1.
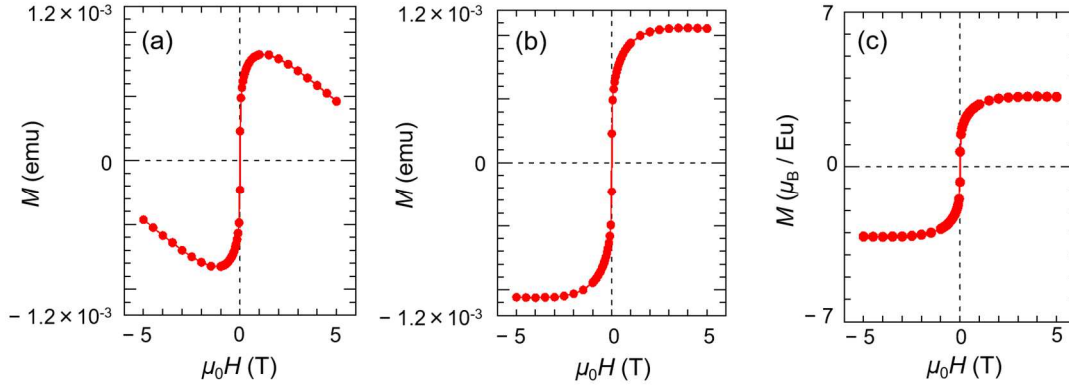
Figure B.2 Three kinds of *M-H* curves of $EuNbO_{2.3}N_{0.7}$/STO (a) the original date (b) the data after subtracting the contribution of the substrate. (c) the data after transforming the units.

2 K, 5 T	Value
M [emu]	1.06×10^{-3}
M [μ_B]	1.14×10^{17}
Cell number in the sample	3.59×10^{16}
M [μ_B / Eu]	3.18

Table B.2 Summary of magnetization value and the $EuNbO_{2.3}N_{0.7}$ cell number in the

Bibliography

[1]   M. Imada, A. Fujimori, and Y. Tokura, Rev. Mod. Phys. **70**, 1039 (1998).

[2]   J. A. Alonso, M. J. Martínez-Lope, M. T. Casais, M. A. G. Aranda, and M. T. Fernández-Díaz, J. Am. Chem. Soc. **121**, 4754 (1999).

[3]   A. Muñoz, J. A. Alonso, M. J. Martínez-Lope, and M. T. Fernández-Díaz, J. Solid State Chem. **182**, 1982 (2009).

[4]   M. L. Medarde, J. Phys. Condens. Matter **9**, 1679 (1997).

[5]   S. Miyasaka, T. Okuda, and Y. Tokura, Phys. Rev. Lett. **85**, 5388 (2000).

[6]   H. C. Nguyen and J. B. Goodenough, Phys. Rev. B **52**, 8776 (1995).

[7]   A. S. Panfilov, G. E. Grechnev, A. A. Lyogenkaya, V. A. Pashchenko, I. P. Zhuravleva, L. O. Vasylechko, V. M. Hreb, V. A. Turchenko, and D. Novoselov, Phys. B Condens. Matter **553**, 80 (2019).

[8]   B. Raveau and M. M. Seikh, *Magnetic and Physical Properties of Cobalt Perovskites*, in *Handbook of Magnetic Materials*, Vol. 23 (Elsevier, 2015), pp. 161–289.

[9]   K. Asai, A. Yoneda, O. Yokokura, J. M. Tranquada, G. Shirane, and K. Kohn, J. Phys. Soc. Japan **67**, 290 (1998).

[10]   V. G. Bhide, D. S. Rajoria, G. R. Rao, and C. N. R. Rao, Phys. Rev. B **6**, 1021 (1972).

[11]   S. R. English, J. Wu, and C. Leighton, Phys. Rev. B **65**, 220407 (2002).

[12]   Y. Tokura, A. Urushibara, Y. Moritomo, T. Arima, A. Asamitsu, G. Kido, and N. Furukawa, J. Phys. Soc. Japan **63**, 3931 (1994).

[13]   P. Schiffer, A. P. Ramirez, W. Bao, and S.-W. Cheong, Phys. Rev. Lett. **75**, 3336 (1995).

[14]   Y. Tokura, Y. Tomioka, H. Kuwahara, A. Asamitsu, Y. Moritomo, and M. Kasai, J. Appl. Phys. **79**, 5288 (1996).

[15]   M. R. Ibarra and J. M. De Teresa, J. Magn. Magn. Mater. **177–181**, 846 (1998).

[16]   A. Urushibara, Y. Moritomo, T. Arima, A. Asamitsu, G. Kido, and Y. Tokura, Phys. Rev. B **51**, 14103 (1995).

[17]   K. Momma and F. Izumi, J. Appl. Crystallogr. **44**, 1272 (2011).

[18]   J. G. Bednorz and K. A. Müller, Zeitschrift Für Phys. B Condens. Matter **64**, 189 (1986).

[19]   J. D. Jorgensen, H.-B. Schüttler, D. G. Hinks, D. W. Capone II, K. Zhang, M. B.

Brodsky, and D. J. Scalapino, Phys. Rev. Lett. **58**, 1024 (1987).

[20] K. Yamada, C. Lee, K. Kurahashi, J. Wada, S. Wakimoto, S. Ueki, H. Kimura, Y. Endoh, and S. Hosoya, Phys. Rev. B - Condens. Matter Mater. Phys. **57**, 6165 (1998).

[21] Y. Hidaka and M. Suzuki, Nature **338**, 635 (1989).

[22] M. K. Wu, J. R. Ashburn, C. J. Torng, P. H. Hor, R. L. Meng, L. Gao, Z. J. Huang, Y. Q. Wang, and C. W. Chu, Phys. Rev. Lett. **58**, 908 (1987).

[23] C. W. Chu, J. Supercond. **7**, 1 (1994).

[24] C. Martins, M. Aichhorn, and S. Biermann, J. Phys. Condens. Matter **29**, (2017).

[25] D. Oka, Y. Hirose, S. Nakao, T. Fukumura, and T. Hasegawa, Phys. Rev. B **92**, 205102 (2015).

[26] I. Nagai, N. Shirakawa, S. Ikeda, R. Iwasaki, H. Nishimura, and M. Kosaka, Appl. Phys. Lett. **87**, 024105 (2005).

[27] S. Huang, H. L. Park, and F. H. Pollak, Mater. Res. Bull. **17**, 1305 (1982).

[28] Q. X. Jia, S. G. Song, X. D. Wu, J. H. Cho, S. R. Foltyn, A. T. Findikoglu, and J. L. Smith, Appl. Phys. Lett. **68**, 1069 (1996).

[29] N. Kikugawa, R. Baumbach, J. S. Brooks, T. Terashima, S. Uji, and Y. Maeno, Cryst. Growth Des. **15**, 5573 (2015).

[30] Y. Maeno, K. Yoshida, H. Hashimoto, S. Nishizaki, S. Ikeda, M. Nohara, T. Fujita, A. P. Mackenzie, N. E. Hussey, J. G. Bednorz, and F. Lichtenberg, J. Phys. Soc. Japan **66**, 1405 (1997).

[31] T. P. Pearsall and C. A. Lee, Phys. Rev. B **10**, 2190 (1974).

[32] J. J. Lin, S. M. Huang, Y. H. Lin, T. C. Lee, H. Liu, X. X. Zhang, R. S. Chen, and Y. S. Huang, J. Phys. Condens. Matter **16**, 8035 (2004).

[33] R. A. Matula, J. Phys. Chem. Ref. Data **8**, 1147 (1979).

[34] G. Koster, L. Klein, W. Siemons, G. Rijnders, J. S. Dodge, C.-B. Eom, D. H. A. Blank, and M. R. Beasley, Rev. Mod. Phys. **84**, 253 (2012).

[35] G. Cao, S. McCall, M. Shepard, J. E. Crow, and R. P. Guertin, Phys. Rev. B **56**, 321 (1997).

[36] A. Kanbayasi, J. Phys. Soc. Japan **41**, 1876 (1976).

[37] K. Terai, T. Ohnishi, M. Lippmaa, H. Koinuma, and M. Kawasaki, Jpn. J. Appl. Phys. **43**, L227 (2004).

[38] S. Kunkemöller, F. Sauer, A. A. Nugroho, and M. Braden, Cryst. Res. Technol. **51**, 299 (2016).

[39] L. Klein, L. Antognazza, T. H. Geballe, M. R. Beasley, and A. Kapitulnik, Phys. Rev. B **60**, 1448 (1999).

[40]   G. Cao, O. Korneta, S. Chikara, L. E. DeLong, and P. Schlottmann, Solid State Commun. **148**, 305 (2008).

[41]   I. Felner, I. Nowik, I. Bradaric, and M. Gospodinov, Phys. Rev. B - Condens. Matter Mater. Phys. **62**, 11332 (2000).

[42]   N. Hiraoka, M. Itou, A. Deb, Y. Sakurai, Y. Kakutani, A. Koizumi, N. Sakai, S. Uzuhara, S. Miyaki, H. Koizumi, K. Makoshi, N. Kikugawa, and Y. Maeno, Phys. Rev. B - Condens. Matter Mater. Phys. **70**, 8 (2004).

[43]   D. J. Singh, J. Appl. Phys. **79**, 4818 (1996).

[44]   I. I. Mazin and D. J. Singh, Phys. Rev. B **56**, 2556 (1997).

[45]   D. Fobes, E. Vehstedt, J. Peng, G. C. Wang, T. J. Liu, and Z. Q. Mao, J. Appl. Phys. **111**, 2 (2012).

[46]   C. S. Alexander, G. Cao, V. Dobrosavljevic, S. Mc Call, J. E. Crow, E. Lochner, and R. P. Guertin, Phys. Rev. B - Condens. Matter Mater. Phys. **60**, R8422 (1999).

[47]   S. Nakatsuji and Y. Maeno, Phys. Rev. Lett. **84**, 2666 (2000).

[48]   S. Nakatsuji and Y. Maeno, J. Solid State Chem. **156**, 26 (2001).

[49]   V. I. Anisimov, I. A. Nekrasov, D. E. Kondakov, T. M. Rice, and M. Sigrist, Eur. Phys. J. B **25**, 191 (2002).

[50]   Y. Maeno, H. Hashimoto, K. Yoshida, S. Nishizaki, T. Fujita, J. G. Bednorz, and F. Lichtenberg, Nature **372**, 532 (1994).

[51]   Y. L. K. D. Nelson, Z. Q. Mao, Y. Maeno, Science (80-.). **306**, 1151 (2004).

[52]   Y. Maeno, S. Kittaka, T. Nomura, S. Yonezawa, and K. Ishida, J. Phys. Soc. Japan **81**, 011009 (2012).

[53]   B. J. Kim, H. Jin, S. J. Moon, J. Y. Kim, B. G. Park, C. S. Leem, J. Yu, T. W. Noh, C. Kim, S. J. Oh, J. H. Park, V. Durairaj, G. Cao, and E. Rotenberg, Phys. Rev. Lett. **101**, 1 (2008).

[54]   S. J. Moon, H. Jin, K. W. Kim, W. S. Choi, Y. S. Lee, J. Yu, G. Cao, A. Sumi, H. Funakubo, C. Bernhard, and T. W. Noh, Phys. Rev. Lett. **101**, 2 (2008).

[55]   H. Watanabe, T. Shirakawa, and S. Yunoki, Phys. Rev. Lett. **110**, 1 (2013).

[56]   Z. Y. Meng, Y. B. Kim, and H.-Y. Kee, Phys. Rev. Lett. **113**, 177003 (2014).

[57]   T. Kondo, M. Nakayama, R. Chen, J. J. Ishikawa, E.-G. Moon, T. Yamamoto, Y. Ota, W. Malaeb, H. Kanai, Y. Nakashima, Y. Ishida, R. Yoshida, H. Yamamoto, M. Matsunami, S. Kimura, N. Inami, K. Ono, H. Kumigashira, S. Nakatsuji, L. Balents, and S. Shin, Nat. Commun. **6**, 10042 (2015).

[58]   T. Ohtsuki, Z. Tian, A. Endo, M. Halim, S. Katsumoto, Y. Kohama, K. Kindo, M. Lippmaa, and S. Nakatsuji, Proc. Natl. Acad. Sci. **116**, 8803 (2019).

[59]   H. Kageyama, K. Hayashi, K. Maeda, J. P. Attfield, Z. Hiroi, J. M. Rondinelli, and K. R. Poeppelmeier, Nat. Commun. **9**, (2018).

[60]   A. Fuertes, J. Mater. Chem. **22**, 3293 (2012).

[61]   Y. Tsujimoto, K. Yamaura, and E. Takayama-Muromachi, Appl. Sci. **2**, 206 (2012).

[62]   Y. Kobayashi, O. Hernandez, C. Tassel, and H. Kageyama, Sci. Technol. Adv. Mater. **18**, 905 (2017).

[63]   P. K. Pandey, R. J. Choudhary, and D. M. Phase, Appl. Phys. Lett. **103**, 132413 (2013).

[64]   Q. Li, X. Yuan, L. Xing, and M. Xu, Sci. Rep. **6**, 27712 (2016).

[65]   Y. Tsujimoto, J. J. Li, K. Yamaura, Y. Matsushita, Y. Katsuya, M. Tanaka, Y. Shirako, M. Akaogi, and E. Takayama-Muromachi, Chem. Commun. **47**, 3263 (2011).

[66]   Y. Tsujimoto, C. I. Sathish, K. P. Hong, K. Oka, M. Azuma, Y. Guo, Y. Matsushita, K. Yamaura, and E. Takayama-Muromachi, Inorg. Chem. **51**, 4802 (2012).

[67]   Y. Tsujimoto, S. Nakano, N. Ishimatsu, M. Mizumaki, N. Kawamura, T. Kawakami, Y. Matsushita, and K. Yamaura, Sci. Rep. **6**, 1 (2016).

[68]   J. F. Afonso, A. Sotnikov, A. Hariki, and J. Kuneš, Phys. Rev. B **99**, 1 (2019).

[69]   M. Sturza, H. Kabbour, S. Daviero-Minaud, D. Filimonov, K. Pokholok, N. Tiercelin, F. Porcher, L. Aldon, and O. Mentré, J. Am. Chem. Soc. **133**, 10901 (2011).

[70]   K. Mori, T. Kamiyama, H. Kobayashi, T. Otomo, K. Nishiyama, M. Sugiyama, K. Itoh, T. Fukunaga, and S. Ikeda, J. Appl. Crystallogr. **40**, s501 (2007).

[71]   Y. Takeda, M. Shimada, F. Kanamaru, M. Koizumi, and N. Yamamoto, Mater. Res. Bull. **9**, 537 (1974).

[72]   I. Gil de Muro, M. Insausti, L. Lezama, and T. Rojo, J. Solid State Chem. **178**, 1712 (2005).

[73]   A. Chikamatsu, T. Maruyama, T. Katayama, Y. Su, Y. Tsujimoto, K. Yamaura, M. Kitamura, K. Horiba, H. Kumigashira, and T. Hasegawa, Phys. Rev. Mater. **4**, 025004 (2020).

[74]   E. J. Moon, Y. Xie, E. D. Laird, D. J. Keavney, C. Y. Li, and S. J. May, J. Am. Chem. Soc. **136**, 2224 (2014).

[75]   T. Onozuka, A. Chikamatsu, T. Katayama, Y. Hirose, I. Harayama, D. Sekiba, E. Ikenaga, M. Minohara, H. Kumigashira, and T. Hasegawa, ACS Appl. Mater. Interfaces **9**, 10882 (2017).

[76] M. AI-Mamouri, P. P. Edwards, C. Greaves, and M. Slaski, Nature **369**, 382 (1994).

[77] M. Sano, Y. Hirose, S. Nakao, and T. Hasegawa, J. Mater. Chem. C **5**, 1798 (2017).

[78] C. Tassel, Y. Kuno, Y. Goto, T. Yamamoto, C. M. Brown, J. Hester, K. Fujita, M. Higashi, R. Abe, K. Tanaka, Y. Kobayashi, and H. Kageyama, Angew. Chemie Int. Ed. **54**, n/a (2014).

[79] S. Mo, Y. Kurauchi, T. Katayama, Y. Hirose, and T. Hasegawa, J. Phys. Chem. C **123**, 25379 (2019).

[80] Y. Kobayashi, M. Tian, M. Eguchi, and T. E. Mallouk, J. Am. Chem. Soc. **131**, 9849 (2009).

[81] R. K. Li and C. Greaves, Phys. Rev. B **62**, 3811 (2000).

[82] K. Kawahara, A. Chikamatsu, T. Katayama, T. Onozuka, D. Ogawa, K. Morikawa, E. Ikenaga, Y. Hirose, I. Harayama, D. Sekiba, T. Fukumura, and T. Hasegawa, CrystEngComm **19**, 313 (2017).

[83] A. Chikamatsu, Y. Kurauchi, K. Kawahara, T. Onozuka, M. Minohara, H. Kumigashira, E. Ikenaga, and T. Hasegawa, Phys. Rev. B **97**, 2 (2018).

[84] D. Oka, Ph. D. Thesis Univ. Tokyo. (2012).

[85] A. B. Jorge, J. Oró-Solé, A. M. Bea, N. Mufti, T. T. M. Palstra, J. A. Rodgers, J. P. Attfield, and A. Fuertes, J. Am. Chem. Soc. **130**, 12572 (2008).

[86] A. Kusmartseva, M. Yang, J. Oró-Solé, A. M. Bea, A. Fuertes, and J. P. Attfield, Appl. Phys. Lett. **95**, 022110 (2009).

[87] M. Yang, J. Oró-Solé, A. Kusmartseva, A. Fuertes, and J. P. Attfield, J. Am. Chem. Soc. **132**, 4822 (2010).

[88] M. Lippmaa, T. Furumochi, S. Ohashi, M. Kawasaki, H. Koinuma, T. Satoh, T. Ishida, and H. Nagasawa, Rev. Sci. Instrum. **72**, 1755 (2001).

[89] M. N. R. Ashfold, F. Claeyssens, G. M. Fuge, and S. J. Henley, Chem. Soc. Rev. **33**, 23 (2004).

[90] D. H. Lowndes, D. B. Geohegan, A. A. Puretzky, D. P. Norton, and C. M. Rouleau, Science (80-.). **273**, 898 (1996).

[91] A. Basillais, R. Benzerga, H. Sanchez, E. Le Menn, C. Boulmer-Leborgne, and J. Perrière, Appl. Phys. A **80**, 851 (2005).

[92] I. Marozau, A. Shkabko, G. Dinescu, M. Döbeli, T. Lippert, D. Logvinovich, M. Mallepell, A. Weidenkaff, and A. Wokaun, Appl. Phys. A **93**, 721 (2008).

[93] F. J. Giessibl, Rev. Mod. Phys. **75**, 949 (2003).

[94] F. Reinert and S. Hüfner, New J. Phys. **7**, 97 (2005).

[95] L. J. van der PAUW, *A METHOD OF MEASURING SPECIFIC RESISTIVITY AND HALL EFFECT OF DISCS OF ARBITRARY SHAPE*, in *Philips Research Reports*, Vol. 13 (WORLD SCIENTIFIC, 1958), pp. 1–9.

[96] A. Mauger and C. Godart, Phys. Rep. **141**, 51 (1986).

[97] R. Sutarto, S. G. Altendorf, B. Coloru, M. Moretti Sala, T. Haupricht, C. F. Chang, Z. Hu, C. Schüßler-Langeheine, N. Hollmann, H. Kierspel, J. A. Mydosh, H. H. Hsieh, H.-J. Lin, C. T. Chen, and L. H. Tjeng, Phys. Rev. B **80**, 085308 (2009).

[98] H. Miyazaki, H. J. Im, K. Terashima, S. Yagi, M. Kato, K. Soda, T. Ito, and S. Kimura, Appl. Phys. Lett. **96**, 232503 (2010).

[99] T. Katsufuji and H. Takagi, Phys. Rev. B **64**, 054415 (2001).

[100] T. Kolodiazhnyi, K. Fujita, L. Wang, Y. Zong, K. Tanaka, Y. Sakka, and E. Takayama-Muromachi, Appl. Phys. Lett. **96**, 252901 (2010).

[101] Y. Kususe, H. Murakami, K. Fujita, I. Kakeya, M. Suzuki, S. Murai, and K. Tanaka, Jpn. J. Appl. Phys. **53**, 05FJ07 (2014).

[102] S. Roy, N. Khan, and P. Mandal, APL Mater. **4**, 026102 (2016).

[103] K. Ishikawa, G. Adachi, and J. Shiokawa, Mater. Res. Bull. **16**, 419 (1981).

[104] V. G. Zubkov, A. P. Tyutyunnik, V. A. Pereliaev, G. P. Shveikin, J. Köhler, R. K. Kremer, A. Simon, and G. Svensson, J. Alloys Compd. **226**, 24 (1995).

[105] J. H. Lee, L. Fang, E. Vlahos, X. Ke, Y. W. Jung, L. F. Kourkoutis, J.-W. Kim, P. J. Ryan, T. Heeg, M. Roeckerath, V. Goian, M. Bernhagen, R. Uecker, P. C. Hammel, K. M. Rabe, S. Kamba, J. Schubert, J. W. Freeland, D. A. Muller, C. J. Fennie, P. Schiffer, V. Gopalan, E. Johnston-Halperin, and D. G. Schlom, Nature **466**, 954 (2010).

[106] C. J. Fennie and K. M. Rabe, Phys. Rev. Lett. **97**, 267602 (2006).

[107] Y. Kozuka, H. Seki, T. C. Fujita, S. Chakraverty, K. Yoshimatsu, H. Kumigashira, M. Oshima, M. S. Bahramy, R. Arita, and M. Kawasaki, Chem. Mater. **24**, 3746 (2012).

[108] R. D. Shannon, Acta Crystallogr. Sect. A **32**, 751 (1976).

[109] D. Y. Wan, Y. L. Zhao, Y. Cai, T. C. Asmara, Z. Huang, J. Q. Chen, J. Hong, S. M. Yin, C. T. Nelson, M. R. Motapothula, B. X. Yan, D. Xiang, X. Chi, H. Zheng, W. Chen, R. Xu, Ariando, A. Rusydi, A. M. Minor, M. B. H. Breese, M. Sherburne, M. Asta, Q.-H. Xu, and T. Venkatesan, Nat. Commun. **8**, 15070 (2017).

[110] Y. Kususe, S. Yoshida, K. Fujita, H. Akamatsu, M. Fukuzumi, S. Murai, and K. Tanaka, J. Solid State Chem. **239**, 192 (2016).

[111] W. Gong, H. Yun, Y. B. Ning, J. E. Greedan, W. R. Datars, and C. V. Stager, J. Solid State Chem. **90**, 320 (1991).

[112] *A. A. Abriksov Fundamentals of the Theory of Metals (North-Holland) (1988).Pdf.*

[113] S. Xu, Y. Gu, X. Zhang, and X. Wu, Eur. Phys. J. Appl. Phys. **85**, 10601 (2019).

[114] T. Kolodiazhnyi, M. Valant, J. R. Williams, M. Bugnet, G. A. Botton, N. Ohashi, and Y. Sakka, J. Appl. Phys. **112**, 083719 (2012).

[115] C. Caspers, M. Müller, A. X. Gray, A. M. Kaiser, A. Gloskovskii, C. S. Fadley, W. Drube, and C. M. Schneider, Phys. Rev. B - Condens. Matter Mater. Phys. **84**, 1 (2011).

[116] P. A. Lee and T. V. Ramakrishnan, Rev. Mod. Phys. **57**, 287 (1985).

[117] K. Kaminaga, R. Sei, K. Hayashi, N. Happo, H. Tajiri, D. Oka, T. Fukumura, and T. Hasegawa, Appl. Phys. Lett. **108**, 1 (2016).

[118] C. Nico, T. Monteiro, and M. P. F. Graça, Prog. Mater. Sci. **80**, 1 (2016).

[119] J. W. Schultze and M. M. Lohrengel, Electrochim. Acta **45**, 2499 (2000).

[120] R. Brayner and F. Bozon-Verduraz, Phys. Chem. Chem. Phys. **5**, 1457 (2003).

[121] A. Esteves, L. C. A. Oliveira, T. C. Ramalho, M. Goncalves, A. S. Anastacio, and H. W. P. Carvalho, Catal. Commun. **10**, 330 (2008).

[122] S. Furukawa, Y. Ohno, T. Shishido, K. Teramura, and T. Tanaka, ACS Catal. **1**, 1150 (2011).

[123] P. Ruello, G. Petot-Ervas, C. Petot, and L. Desgranges, J. Am. Ceram. Soc. **88**, 604 (2005).

[124] R. Pynn and J. D. Axe, J. Phys. C Solid State Phys. **9**, L199 (1976).

[125] J. K. Hulm, C. K. Jones, R. A. Hein, and J. W. Gibson, J. Low Temp. Phys. **7**, 291 (1972).

[126] A. M. Okaz and P. H. Keesom, Phys. Rev. B **12**, 4917 (1975).

[127] K. Wang and J. F. Li, J. Adv. Ceram. **1**, 24 (2012).

[128] A. A. BALLMAN, J. Am. Ceram. Soc. **48**, 112 (1965).

[129] B. T. Matthias and J. P. Remeika, Phys. Rev. **76**, 1886 (1949).

[130] S. H. Wemple, M. DiDomenico, and I. Camlibel, Appl. Phys. Lett. **12**, 209 (1968).

[131] N. Mkhitaryan, J. Zaraket, N. Kokanyan, E. Kokanyan, and M. Aillerie, Eur. Phys. J. Appl. Phys. **85**, 30502 (2019).

[132] D. Oka, Y. Hirose, S. Nakao, T. Fukumura, and T. Hasegawa, Phys. Rev. B **92**, 205102 (2015).

[133] T. Maruyama, A. Chikamatsu, T. Onozuka, and T. Hasegawa, Appl. Phys. Lett.

113, 032401 (2018).

[134] V. Motaneeyachart, Y. Hirose, A. Suzuki, S. Nakao, I. Harayama, D. Sekiba, and T. Hasegawa, Chem. Lett. **47**, 65 (2018).

[135] R. KIKUCHI, T. KOUZAKI, T. KURABUCHi, and K. HATO, Electrochemistry **83**, 711 (2015).

[136] H. Urabe, T. Hisatomi, T. Minegishi, J. Kubota, and K. Domen, Faraday Discuss. **176**, 213 (2014).

[137] T. Motohashi, M. Ito, Y. Masubuchi, M. Wakeshima, and S. Kikkawa, Inorg. Chem. **51**, 11184 (2012).

[138] D. Oka, Y. Hirose, M. Kaneko, S. Nakao, T. Fukumura, K. Yamashita, and T. Hasegawa, ACS Appl. Mater. Interfaces **10**, 35008 (2018).

[139] I. Harayama, K. Nagashima, Y. Hirose, H. Matsuzaki, and D. Sekiba, Nucl. Instruments Methods Phys. Res. Sect. B Beam Interact. with Mater. Atoms **384**, 61 (2016).

[140] K. S. Takahashi, M. Onoda, M. Kawasaki, N. Nagaosa, and Y. Tokura, Phys. Rev. Lett. **103**, 057204 (2009).

[141] T. Yamamoto, R. Yoshii, G. Bouilly, Y. Kobayashi, K. Fujita, Y. Kususe, Y. Matsushita, K. Tanaka, and H. Kageyama, Inorg. Chem. **54**, 1501 (2015).

[142] A. Yamasaki, S. Tachibana, H. Fujiwara, A. Higashiya, A. Irizawa, O. Kirilmaz, F. Pfaff, P. Scheiderer, J. Gabel, M. Sing, T. Muro, M. Yabashi, K. Tamasaku, H. Sato, H. Namatame, M. Taniguchi, A. Hloskovskyy, H. Yoshida, H. Okabe, M. Isobe, J. Akimitsu, W. Drube, R. Claessen, T. Ishikawa, S. Imada, A. Sekiyama, and S. Suga, Phys. Rev. B - Condens. Matter Mater. Phys. **89**, 1 (2014).

[143] C. Lu, A. Quindeau, H. Deniz, D. Preziosi, D. Hesse, and M. Alexe, Appl. Phys. Lett. **105**, (2014).

[144] M. Souri, J. G. Connell, J. Nichols, J. Terzic, G. Cao, and A. Seo, J. Appl. Phys. **126**, 185101 (2019).

[145] H. Wang, C. Lu, J. Chen, Y. Liu, S. L. Yuan, S.-W. Cheong, S. Dong, and J.-M. Liu, Nat. Commun. **10**, 2280 (2019).

[146] M. Ge, T. F. Qi, O. B. Korneta, D. E. De Long, P. Schlottmann, W. P. Crummett, and G. Cao, Phys. Rev. B - Condens. Matter Mater. Phys. **84**, 1 (2011).

[147] X. Chen, T. Hogan, D. Walkup, W. Zhou, M. Pokharel, M. Yao, W. Tian, T. Z. Ward, Y. Zhao, D. Parshall, C. Opeil, J. W. Lynn, V. Madhavan, and S. D. Wilson, Phys. Rev. B - Condens. Matter Mater. Phys. **92**, 1 (2015).

[148] K. Horigane, M. Fujii, H. Okabe, K. Kobayashi, R. Horie, H. Ishii, Y. F. Liao, Y. Kubozono, A. Koda, R. Kadono, and J. Akimitsu, Phys. Rev. B **97**, 1 (2018).

[149] T. F. Qi, O. B. Korneta, L. Li, K. Butrouna, V. S. Cao, X. Wan, P. Schlottmann, R. K. Kaul, and G. Cao, Phys. Rev. B **86**, 125105 (2012).

[150] J. P. Clancy, A. Lupascu, H. Gretarsson, Z. Islam, Y. F. Hu, D. Casa, C. S. Nelson, S. C. Lamarra, G. Cao, and Y. J. Kim, Phys. Rev. B - Condens. Matter Mater. Phys. **89**, 1 (2014).

[151] C. Peterson, M. W. Swift, Z. Porter, R. J. Clément, G. Wu, G. H. Ahn, S. J. Moon, B. C. Chakoumakos, J. P. C. Ruff, H. Cao, C. Van De Walle, and S. D. Wilson, Phys. Rev. B **98**, 1 (2018).

[152] K. Kuramochi, T. Shimano, T. Nishio, H. Okabe, A. Koda, K. Horigane, J. Akimitsu, and H. Ogino, Phys. Rev. Mater. **4**, 013403 (2020).

[153] T. Katayama, A. Chikamatsu, Y. Hirose, R. Takagi, H. Kamisaka, T. Fukumura, and T. Hasegawa, J. Mater. Chem. C **2**, 5350 (2014).

[154] P. Anitha Sukkurji, A. Molinari, C. Reitz, R. Witte, C. Kübel, V. Chakravadhanula, R. Kruk, and O. Clemens, Materials (Basel). **11**, 1204 (2018).

[155] J. Wang, Y. Shin, E. Arenholz, B. M. Lefler, J. M. Rondinelli, and S. J. May, Phys. Rev. Mater. **2**, 073407 (2018).

[156] T. Katayama, A. Chikamatsu, Y. Hirose, T. Fukumura, and T. Hasegawa, J. Sol-Gel Sci. Technol. **73**, 527 (2015).

[157] A. Chikamatsu, K. Kawahara, T. Shiina, T. Onozuka, T. Katayama, and T. Hasegawa, ACS Omega **3**, 13141 (2018).

[158] J. Nichols, J. Terzic, E. G. Bittle, O. B. Korneta, L. E. De Long, J. W. Brill, G. Cao, and S. S. A. Seo, Appl. Phys. Lett. **102**, 10 (2013).

[159] P. R. Slater, J. Fluor. Chem. **117**, 43 (2002).

[160] K. Wissel, J. Heldt, P. B. Groszewicz, S. Dasgupta, H. Breitzke, M. Donzelli, A. I. Waidha, A. D. Fortes, J. Rohrer, P. R. Slater, G. Buntkowsky, and O. Clemens, Inorg. Chem. **57**, 6549 (2018).

[161] D. Drouin, A. R. Couture, D. Joly, X. Tastet, V. Aimez, and R. Gauvin, Scanning **29**, 92 (2007).

[162] G. K. Wertheim and H. J. Guggenheim, Phys. Rev. B **22**, 4680 (1980).

[163] R. Kötz, J. Electrochem. Soc. **131**, 72 (1984).

[164] V. Pfeifer, T. E. Jones, J. J. Velasco Vélez, C. Massué, R. Arrigo, D. Teschner, F. Girgsdies, M. Scherzer, M. T. Greiner, J. Allan, M. Hashagen, G. Weinberg, S. Piccinin, M. Hävecker, A. Knop-Gericke, and R. Schlögl, Surf. Interface Anal. **48**, 261 (2016).

[165] X. Liu, Y. Cao, B. Pal, S. Middey, M. Kareev, Y. Choi, P. Shafer, D. Haskel, E. Arenholz, and J. Chakhalian, Phys. Rev. Mater. **1**, 1 (2017).

[166] A. Bourlange, D. J. Payne, R. G. Palgrave, H. Zhang, J. S. Foord, R. G. Egdell, R. M. J. Jacobs, T. D. Veal, P. D. C. King, and C. F. McConville, J. Appl. Phys. **106**, (2009).

[167] D. J. Payne, R. G. Egdell, W. Hao, J. S. Foord, A. Walsh, and G. W. Watson, Chem. Phys. Lett. **411**, 181 (2005).

[168] A. Nag, S. Bhowal, A. Chakraborty, M. M. Sala, A. Efimenko, F. Bert, P. K. Biswas, A. D. Hillier, M. Itoh, S. D. Kaushik, V. Siruguri, C. Meneghini, I. Dasgupta, and S. Ray, Phys. Rev. B **98**, 1 (2018).

[169] S. J. Moon, H. Jin, W. S. Choi, J. S. Lee, S. S. A. Seo, J. Yu, G. Cao, T. W. Noh, and Y. S. Lee, Phys. Rev. B **80**, 195110 (2009).

[170] C. H. Sohn, M. C. Lee, H. J. Park, K. J. Noh, H. K. Yoo, S. J. Moon, K. W. Kim, T. F. Qi, G. Cao, D. Y. Cho, and T. W. Noh, Phys. Rev. B - Condens. Matter Mater. Phys. **90**, 1 (2014).

[171] V. Ilakovac, A. Louat, A. Nicolaou, J.-P. Rueff, Y. Joly, and V. Brouet, Phys. Rev. B **99**, 035149 (2019).

[172] N. F. Mott, J. Non. Cryst. Solids **1**, 1 (1968).

[173] A. L. Efros and B. I. Shklovskii, J. Phys. C Solid State Phys. **8**, (1975).

[174] N. Srmoo, I. D. Fawcett ', K. V Ramanujachary " ', and M. Greenblatt, Pergamon Mater. Res. Bull. **32**, 1565 (1997).

[175] M. Yashima, U. Fumi, H. Nakano, K. Omoto, and J. R. Hester, J. Phys. Chem. C **117**, 18529 (2013).

[176] J. Lynch, C. Giannini, J. K. Cooper, A. Loiudice, I. D. Sharp, and R. Buonsanti, J. Phys. Chem. C **119**, 7443 (2015).

[177] K. Fujita, N. Wakasugi, S. Murai, Y. Zong, and K. Tanaka, Appl. Phys. Lett. **94**, 1 (2009).

[178] K. Isawa, J. Sugiyama, and H. Yamauchi, Phys. Rev. B **47**, 11426 (1993).